Ph. D. Thesis

Physics

Selim Reza

Acoustooptically Tunable Waveguide Lasers in Erbium Doped Lithium Niobate

UNIVERSITÄT PADERBORN
Die Universität der Informationsgesellschaft

2006

Acoustooptically Tunable Waveguide Lasers in Erbium Doped Lithium Niobate

Thesis

Submitted to the
Department of Physics, Faculty of Science
University of Paderborn, Germany
for the degree
Doctor of Philosophy (Ph. D./Dr. rer. nat.)

by

Selim Reza

Reviewers:

1. Professor Dr. Wolfgang Sohler
2. Professor Dr. Artur Zrenner

Submission: May 09, 2006
Examination: July 10, 2006

To

Ichcha
&
Sneha

Abstract

Integrated acoustooptically tunable lasers are developed and investigated. They are fabricated in an Erbium-diffusion-doped Lithium Niobate substrate and have Titanium-diffused optical channel waveguides. The key element of these lasers is an acoustooptical (AO) filter which is monolithically integrated inside the laser cavity and used as wavelength selective element. The laser resonator is formed by dielectric mirrors deposited directly on the polished waveguide end faces. The filter consists of two waveguide polarization splitters and an AO polarization converter with a tapered acoustical directional coupler in between. It consists of acoustical waveguides with undoped Lithium Niobate core; their claddings are defined by thick Titanium indiffusion. Interdigital transducers are used to excite the surface acoustic wave (SAW). Through the AO interaction SAW induces a polarization conversion of a selected optical wavelength which is then separated by the polarization splitter. Also this conversion process is accompanied by a frequency shift of the converted wave by the frequency of the driving SAW. So a second AO polarization converter is used inside the cavity to compensate this frequency shift. Thus the feedback condition of conventional laser operation is satisfied where resonances build up at fixed frequencies (cavity modes). Without this compensator the oscillating optical wave is frequency shifted in each round trip which results in a much broader spectral emission. These two types of lasers are investigated: one is a more conventional Frequency Shift Compensated (FSC) laser and the other is a Frequency Shifted Feedback (FSF) laser. The design, operation and output characteristics of these lasers are presented.

The lasers are optically pumped by a fiber-coupled, Bragg-grating stabilized laser-diode of 1480 nm wavelength. The emission wavelength and the tuning range are identical for both integrated lasers: from 1530 nm to 1577 nm. The tuning slope is –8.2 nm/MHz. To get lasing at 1560 nm wavelength, a SAW frequency of 170.70 MHz is to be adjusted. In the FSC mode of operation, single mode laser emission is achieved with a measured linewidth of smaller than 12 pm. More than 0.5 mW of laser output power (TE polarized) is obtained in the wavelength range around 1560 nm at a pump power level of 130 mW (TM polarized). The spectral properties of the integrated FSF laser are completely different in comparison with those of the integrated FSC laser. At 1560 nm wavelength a linewidth of 180 pm is observed at a pump power level of 95 mW (both pump and laser emission are TM polarized). This linewidth depends mainly on the net round trip gain inside the cavity. Unique features of this emission are demonstrated when investigated in an interferometric setup. In steady state operation, the FSF laser output consists of a comb of chirped (at the rate of 2.43×10^{17} Hz/s) frequency components with a regular spacing equal to the cavity free spectral range (of 711 MHz corresponding to a waveguide cavity of length 94.2 mm); they are strongly correlated in phase. These properties allow to apply the FSF laser for optical frequency domain ranging (OFDR). Details of this measurement technique are described with experimental results.

Contents

Chapter 1

Introduction

1.1 Background

Integrated Optical Circuits/devices (IOC) are supposed to do for optics what integrated circuits (IC) are doing for electronics [1]. Therefore, as optical sources, integrated optical lasers are essential. Different types of integrated optical devices and lasers with advanced properties have already been demonstrated in different material systems such as III–V compounds, glass and Lithium Niobate ($LiNbO_3$) with a good potential for a variety of attractive applications. $LiNbO_3$ has a unique combination of excellent electrooptic, acoustooptic, nonlinear, and photorefractive properties for which it is well known as important substrate material for integrated optical circuits [2–7]. The development of very low loss Titanium (Ti) in-diffused optical waveguides and selective diffusion doping with various active dopants such as Erbium (Er) allows to integrate both passive and active optical components monolithically. Rare-earth doped optically pumped integrated laser devices in $LiNbO_3$ have already been reported [8–16].

Particularly, Erbium diffusion doped Lithium Niobate (Er:$LiNbO_3$) lasers attract considerable interests for its emission wavelengths. If it is optically pumped at 1480 nm wavelength, laser emission is possible within the wavelength range from 1530 nm to 1620 nm (the low attenuation range of an optical fiber). The active medium of this laser can easily be fabricated in the surface layer of a $LiNbO_3$ substrate by in-diffusion of a thin vacuum deposited Er layer [17]. Afterwards, a single mode channel waveguide is defined by the standard indiffusion technique of Ti-stripes.

Recently, the development of a whole class of new lasers of higher functionality have been demonstrated in Er:$LiNbO_3$ [18–21]. The simple Fabry-Perot laser with continuous wave (cw) emission of high efficiency is fabricated by depositing multilayer dielectric mirrors on the end faces of a Ti-doped Er-doped (Ti:Er:$LiNbO_3$) waveguide to form the laser cavity [22–24]. An intracavity phase or amplitude modulator is used to obtain mode-locked operation to generate ultrashort pulses [25, 26]. An amplitude modulator inside the cavity is used to get Q-switching (short pulses of high power) [27]. One or both mirrors can be replaced by a Bragg grating to form a DBR (Distributed

Bragg Reflector) or DFB (Distributed Feedback) cavity to obtain a very narrowband (single frequency) laser emission at a fixed wavelength [28–30]. Such gratings are etched into the surface of the waveguide amplifier or, alternatively, photorefractive gratings are developed by holographic exposure of the substrate surface doped with Iron or Copper [31–34].

By utilizing the wavelength selective property of acoustooptical (AO) interactions, wavelength tunable integrated AO filters have been developed in $LiNbO_3$ for the wavelength range around 1550 nm. They can be fabricated by integrating an AO polarization converter between two polarization splitters. [35–37]. The use of such filters have already been demonstrated in optical communication systems consists with Wavelength Division Multiplexing (WDM) [38, 39]. Such a filter incorporated in a Fabry-Perot cavity allows to develop an electronically tunable integrated laser with a wide tuning range [40–42].

In the process of AO polarization conversion, the converted optical wave always experiences a frequency shift by the amount of the driving frequency of the surface acoustic wave (SAW) [43–45]. In the standard method for sustaining laser oscillation, the oscillating optical wave inside the cavity is reproduced in amplitude and phase after each round trip. Therefore, a second AO polarization converter is required inside the cavity to compensate the frequency shift. Since almost all cw lasers are operated in this manner, this can be termed as conventional, Frequency Shift Compensated (FSC) laser operation. Without this frequency shift compensator inside the cavity, the oscillating optical wave remains frequency shifted after each round trip and it leads to another type of laser emission known as frequency shifted feedback laser [46].

Frequency Shifted Feedback (FSF) lasers have been investigated in bulk optics for several years [47–71]; they proved to be unique sources for various applications which are difficult to realize with conventional lasers [72–83]. In the bulk optics approach, an acoustooptical modulator is placed inside the laser cavity and the fist-order deflected light is allowed to feed back; it experiences a frequency shift by the amount of the driving acoustic frequency. The spectrum of this FSF laser is drastically different from that of a conventional FSC laser.

1.2 Motivation

Different types of lasers are in use for different applications in industry, environment, medicine, communications, and in various fields of scientific research, etc.. Different properties of the laser beam are important for those purposes. To meet all requirements, research is also growing rapidly with new materials and technologies to develop laser sources with advanced features. The technology for integrated optical devices is improving with similar pace to develop reliable, miniature and robust lasers with relatively low cost. There is a high potential application of tunable integrated laser also. As a single wavelength tunable laser can deliver many wavelengths in a range, in most cases, it is preferable to use a tunable laser instead of a cascaded system of number of fixed wavelength lasers. The economics of new optical networks requires a

shift from current fixed dense wavelength division multiplexing (DWDM) to flexible DWDM networks. These, in turn, require high-performance tunable optical devices and modules that can be rapidly replaced and adapted. Tunable lasers expand the flexibility in its broadest sense: inventory management, networking flexibility, and feature flexibility. The wider the tuning range the more useful the laser is for the applications. The tuning range is limited by the gain bandwidth product of the lasing material if an appropriate tuning mechanism is applied. For efficient wide range tuning, the best suitable two mechanisms are: tuning with a grating and tuning with an acoustooptical (AO) tunable filter [84–87]. Tuning with an external grating is already popular in many solid-state laser systems due to its very narrow linewidth selection; however, it has the drawback to use slowly adjustable mechanics. AO tunable filters can give wide wavelength tuning without any moving parts in the system. The tuning mechanism is fast and even allows to address multiple wavelengths simultaneously. Therefore, the best choice to achieve a wide tuning range in an integrated optical laser is to use AO filter.

For many applications mode hop free continuous tuning over the wide wavelength range is required. For this tuning, the longitudinal mode must be shifted at exactly the same rate as the filter peak so that the same mode maintains its status as the lowest loss mode and continues to oscillate. For conventional laser operation there are two AO polarization mode converters inside the laser cavity driven by the same acoustic frequency. By changing the relative phase between the two RF (Radio Frequency)-signals together with the frequency in an appropriate manner, continuous mode-hop free tuning should be possible.

Already bulk optical frequency shifted feedback (FSF) lasers have attracted much interest to realize optical frequency domain ranging because of its frequency chirped laser emission of high and linear chirp rate without any expensive high frequency electronics. An integrated FSF laser should be even more useful in comparison with the bulk optical device due to its expected stable operation and compact configuration.

This work is a part of the continuous effort to demonstrate different types of integrated lasers on a Lithium Niobate substrate with added advanced features for a variety of applications. It is based on the experiences acquired in the previous activities to develop acoustooptically tunable wavelength filters with internal amplification [41] and tunable integrated lasers [40].

A detailed description of design, development, operation and emission properties of an acoustooptically tunable conventional FSC laser is presented in this thesis. Nearly continuous tuning over the range from 1530 nm to 1577 nm with single mode emission is observed. In addition, operation and output characteristics of the first integrated tunable FSF laser are described [20, 88–90]. As an attractive application of this laser optical frequency domain ranging is demonstrated.

1.3 Thesis Organisation

This thesis describes the design, fabrication and properties of two types of tunable integrated laser: a conventional, frequency shift compensated (FSC) laser and a frequency shifted feedback (FSF) laser. These two lasers are similar in structure but have differences in operation and thereby, in the resultant spectral properties. The most important characteristics (power characteristics, tunability and spectral characteristics) have been experimentally investigated. Since the basic components of these two lasers are the same, they are discussed in the beginning together with their properties. Fabrication steps of the lasers are mentioned only once.

In Chapter 2, the basic components for the integrated tunable lasers and their functionality are discussed individually. Experimental results of their performances are given in each section. Those results represent the characteristics of the components monolithically integrated on a substrate to form the laser.

The design, fabrication and operation of the tunable integrated FSC laser are discussed in Chapter 3. The conditions for conventional laser operation are maintained to yield a single mode laser output. The spectral characteristics are discussed.

In Chapter 4, the operation and output characterization of the tunable integrated FSF laser are described.

As an interesting application, optical frequency domain ranging (OFDR) is demonstrated in Chapter 5. It is shown that the spatial resolution is determined by the FSF laser properties and that it is independent of the measurement range. A summary and an outlook are presented in Chapter 6.

Chapter 2

Basic Components

2.1 Introduction

A **waveguide laser** in $LiNbO_3$ consists of an Er doped Ti-indiffused optical **waveguide amplifier** with deposited **end face mirrors**. This is a Fabry-Perot cavity for basic laser operation. Without any wavelength selective element inside the cavity, the emission wavelength of this laser depends on the spectral properties of the cavity, e.g., wavelength dependent mirror reflectivity, amplifier gain spectrum, and waveguide scattering losses and therefore on the pump power level also [16, 22, 23].

The laser emission can be selected at the desired wavelength within the gain bandwidth of the amplifier by integrating an acoustooptical (AO) tunable filter inside the Fabry-Perot cavity. The architecture of such an integrated wavelength tunable laser is shown in figure 2.1. It comprises of two Erbium doped optical waveguides as am-

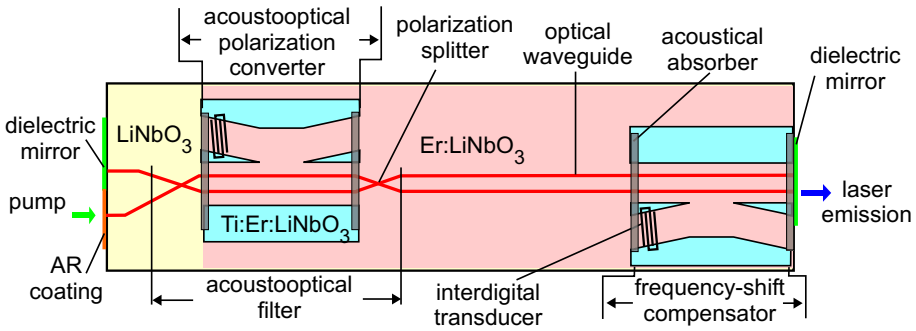

Figure 2.1: Schematic diagram of an acoustooptically tunable Ti:Er:$LiNbO_3$ waveguide laser. The basic components are Ti:Er:$LiNbO_3$ optical waveguide/amplifier, polarization splitters, acoustooptical polarization mode converter/filter/frequency-shifter, dielectric coatings for mirror and anti reflection (AR).

plifying medium. Multilayer dielectric mirrors are deposited at the end faces to form the cavity. One of the end face of the waveguides is antireflection (AR) coated to couple-in the pump light. There is an **acoustooptical filter** as a wavelength tunable element at the left hand side of the cavity. The acoustooptical filter consists of an **AO**

polarization mode converter between two **polarization splitters**. Since the AO polarization mode conversion is always accompanied by a frequency shift of the optical wave, a second polarization mode converter (at the right hand side in the cavity) is necessary to serve as frequency shift compensator for a conventional laser operation.

To understand the design and operation of an acoustooptically wavelength tunable laser, we need to know in detail the properties and functional characteristics of these basic elements of the laser. In this chapter we shall discuss sequentially optical waveguide, polarization splitter, waveguide amplifier, acoustooptical polarization mode converter, acoustooptical tunable filter and the dielectric layers for high-reflection and anti-reflection coatings. For each of the elements, first the required properties are described and then the functional characteristics are presented from experimental measurements of an actual laser structure.

2.2 Optical Waveguides

The basic component of any integrated waveguide device or circuit is the optical waveguide. For devices like integrated waveguide lasers with tunable single mode emission the following properties of the optical waveguides are required:

- Very low propagation losses;
- Single mode guiding of both polarizations within a wide wavelength range;
- Constant cross section and refractive index profile along the waveguide length.

The waveguide is fabricated in X-cut (Y-propagating) $LiNbO_3$. In this orientation, a large electromechanical coupling coefficient is utilized for efficient excitation of the surface acoustic waves (to be discussed later). Selective diffusion doping of $LiNbO_3$ by Erbium is necessary for integrating active and passive components monolithically as required for such laser development. To fabricate a single mode waveguide which fulfils the requirements given above a $7\,\mu$m wide and 100 nm thick photolithographically defined Ti-stripe is indiffused. The optical waveguide structure for the laser is shown in figure 2.2 together with a straight reference waveguide for characterization.

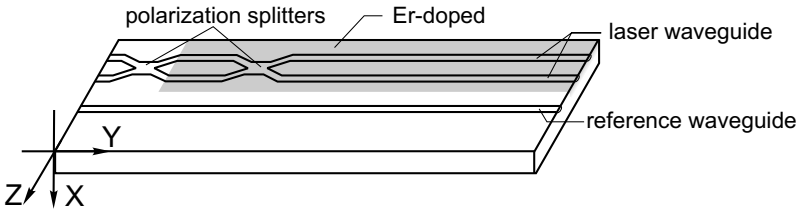

Figure 2.2: Schematic of the optical waveguide structure with polarization splitters for the laser and a reference waveguide for characterizations. X, Y and Z($\equiv$ optical c-axis) are the crystal axes.

Waveguide scattering loss is investigated in the straight optical waveguide in the undoped (without Erbium) section by analyzing the low-finesse Fabry-Perot resonance [91].

Polished end faces (reflectivity $\sim$ 14% with respect to air) perpendicular to the waveguide form a low-finesse Fabry-Perot cavity. The waveguide loss is evaluated by measuring the contrast of the transmitted optical intensity as function of the substrate temperature when a highly coherent external cavity laser (at $\lambda = 1550\,\text{nm}$) is launched into the waveguide. This resonator method yields results, which are independent on the input and output coupling efficiencies. For a 94.2 mm long waveguide the measured losses are given in Table 2.1 as an example. The measured scattering losses are 0.05 and 0.15 dB/cm for TM and TE polarizations, respectively, represent a good quality waveguide. For the laser operation, it is necessary to consider the propagation of optical modes in both polarizations since they experience a polarization conversion ($\text{TE} \leftrightarrow \text{TM}$) by the acoustooptical mode converter/filter.

Table 2.1: Results of waveguide (reference channel) scattering loss measurements

Polarization	Loss (dB/cm)
TM	0.05
TE	0.15

The mode sizes of the guided waves in both polarizations are determined by measuring the near-field intensity distribution at the waveguide output. An incoherent amplified spontaneous emission (ASE) from a Erbium Doped Fiber Amplifier (EDFA) is launched via a bandpass filter (of linewidth 1.1 nm) into the waveguide through free space lens coupling. The optical intensity distribution from the output of the waveguide is magnified (100X) and imaged to an infrared camera. The intensity profiles confirm that the waveguides are single mode in both polarizations. However, a polarization dependent intensity distribution is measured as given in Table 2.2.

Table 2.2: Results of near field mode size (at $1/e$ full width) measurements

Polarization	Horizontal direction (Approx. Gaussian profile) [μm]	Vertical direction (Approx. Hermite-Gaussian profile) [μm]
TM	8.5	4.4
TE	6.7	4.0

The magnified images of the intensity distribution of the modes in both polarizations are shown in figure 2.3. It is clearly visible that the mode size (at $1/e$ full width) of TM polarized light is slightly larger than that of TE polarized light. This is due to the difference in refractive index profiles in the respective polarizations. In X-cut, Y-propagating waveguide, the TM polarized light sees the ordinary refractive index (n_o) and TE polarized light sees the extra-ordinary refractive index (n_e). The refractive index increase, of course, depends upon the Ti concentration, but in a way

that is different for the n_o- and n_e- distributions [92]. According to the fabrication conditions of the waveguide used here, a larger increase of δn_e in comparison to δn_o is obtained in almost the whole cross-section of the guide. Therefore, one gets a tighter confinement for the TE polarized mode.

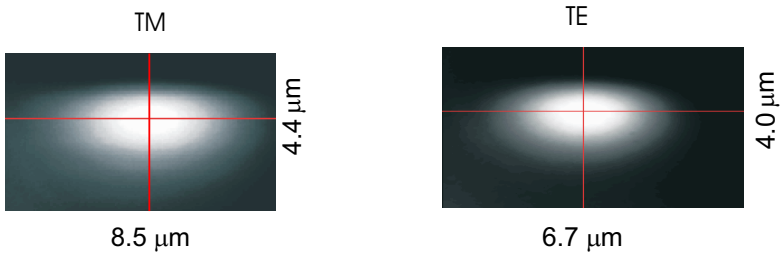

(a) (b)

Figure 2.3: Near field images of the intensity distribution of the guided optical modes; (a) TM and (b) TE polarized modes. The numbers [in μm] represent the $1/e$ full width of the mode intensity

2.3 Polarization Splitters

The second important component of this laser is the waveguide polarization splitter. It splits the optical waves of two orthogonal polarization modes in two optical waveguide branches. The performance of this component is given by the splitting ratio which is defined by the ratio of the optical power in unwanted output port to the total output power when light of particular polarization (TE or TM) is launched into the input port. So a very low splitting ratio indicates that the optical wave of particular polarization is guiding only in the desired branch. Moreover, very low wavelength sensitivity of the splitting ratio is required for a wavelength tunable laser.

The basic structure of such a component is shown in figure 2.4(a) [36, 39]. The principle of operation is based on the two-mode interference in an optical directional coupler. The two incoming single mode waveguides (7 μm wide) combine to a double mode waveguide of 14 μm width (zero gap coupler). Within the structure the accumulated phase difference $\Delta\Phi$ between the interfering symmetrical fundamental and the asymmetrical first-order modes results in a beating of the optical power density. The output power will be localized in either branch if this phase difference is a multiple of π. Therefore, the structure operates as a polarization splitter, if $\Delta\Phi$ is an even multiple for one polarization and an odd one for the other, simultaneously [93, 94].

This can be achieved by a careful design of the central section length L_c and the opening angle θ. One possibility is that the splitter can operate in the third order for TE and in the second order for TM as shown in figure 2.4(a). Therefore, the phase difference is 3π for TE polarized waves resulting in a coupling to the cross state. Here the cross state means, if the input light travels through the upper (or lower) branch, behind the central section the output light is coupled to the lower (or upper) branch. For the same length of L_c, the phase difference of 2π for TM polarized waves leads

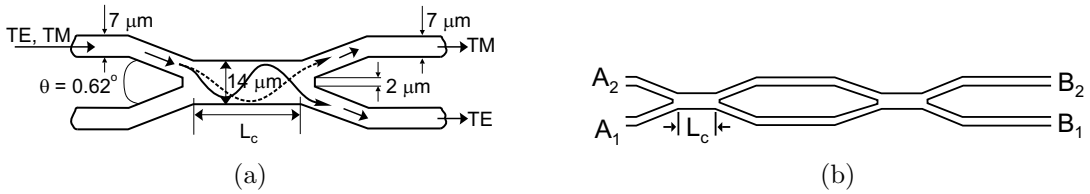

(a) (b)

Figure 2.4: Schematic view of the optical waveguide polarization splitters: (a) Design of the polarization splitter where TM and TE polarized wave travel in bar and cross states, respectively, L_c is the length of the central section of the common waveguide ($\approx 300\,\mu$m), [36, 39]. (b) Optical waveguide structure with two polarization splitters. A's and B's are the input and output ports.

to a coupling into the bar state. Here the bar state means, if the input light travels through the upper (or lower) branch, behind the central section the output light is coupled to the upper (or lower) branch (figure 2.4(a)). An advantage of such low order splitters is that the wavelength sensitivity is very low. This property is very useful for developing wavelength tunable lasers of wide tuning range.

The opening angle of the two branches is as small as 0.62° and width of the common waveguide is 14 μm as shown in figure 2.4(a). Due to limitations in modelling accuracy and fabrication errors, six laser structures have been fabricated monolithically with different lengths of the central sections, L_c ranging from 310 μm to 360 μm with an increment of 10 μm.

The optical waveguide structure with two polarization splitters as required by the integrated acoustooptical filter (to be discussed later) is shown in figure 2.4(b). To investigate the passive overall structure and in this way the performances of polarization splitters light from a single frequency External Cavity Laser (ECL) is launched either to the input A_1 or A_2 at the left hand side. Antireflection coatings are deposited on both end faces to avoid any reflections; otherwise, unwanted interference may occur during a measurement with coherent input light. The output power of the transmitted light from both ports on the right hand side (B_1, B_2) is measured for particular input port. Then the splitting ratio is calculated to estimate the performance of the splitter. The measurement is done for both TE and TM polarized input and at three different wavelengths, 1530 nm, 1550 nm and 1580 nm for all the polarization splitters having different L_c. For the sample pb164x_y, the splitters with $L_c = 330\,\mu$m show the best results compared to other values of L_c. For the input branch A_2 in TE polarization, the splitting ratio is about -18 dB and for the input branch A_1 in TM polarization the splitting ratio is about -30 dB.

The optimum length of L_c for both polarizations do not coincide exactly for a fabricated device. From the figure 2.4(b) it is clear that a slight asymmetry of the Mach-Zehnder-type structure combining two polarization splitters would lead to phase differences between the waves passing through the two arms. So this evaluation of splitting ratio might have some errors and does not represent the performance of the individual polarization splitter. A high splitting ratio leads to an additional loss in the structure.

2.4 Waveguide Amplifier

An optical amplifier is an essential component of any laser. The main requirement is to overcome the losses of the optical waves in a cavity by the means of optical amplification through the optically active medium. To get lasing it is essential to achieve an over all gain of more than unity inside the cavity. In case of a tunable laser, lasing is possible over the wavelength range where it is achieved. To get a waveguide amplifier for the integrated laser, a Ti-indiffused optical waveguide is fabricated in the surface of an Er- diffusion-doped $LiNbO_3$ substrate. At first a vacuum deposited thin layer (~ 20 nm) of metallic Erbium is indiffused in $LiNbO_3$ at 1130 ℃ during 150 hours. Then a Ti-indiffused optical waveguide is fabricated in this Er:$LiNbO_3$ surface. The electronic transitions of Er^{3+}:$LiNbO_3$ are exploited for amplification around 1550 nm wavelength. For lasing around this wavelength range they represent a quasi three level system with ground state absorption.

The process of Erbium in-diffusion has been characterized in detail using secondary ion mass spectroscopy (SIMS), secondary neutral mass spectroscopy (SNMS), Rutherford backscattering spectroscopy (RBS), and atomic force microscopy (AFM) [17]. Using X-ray standing wave spectroscopy (XSW) it has been found that Er is incorporated into $LiNbO_3$ on a vacant Li-site or replaces Lithium [95]. Er-diffusion doping of $LiNbO_3$ follows Fick's law resulting in a nearly Gaussian concentration profile [17]. Being $LiNbO_3$ an anisotropic crystal, the diffusion coefficient depends on the crystal cut which can be clearly seen in figure 2.5 where the temperature dependent diffusion coefficient derived from measured Er-concentration profiles has been plotted as Arrhenius-diagram [17].

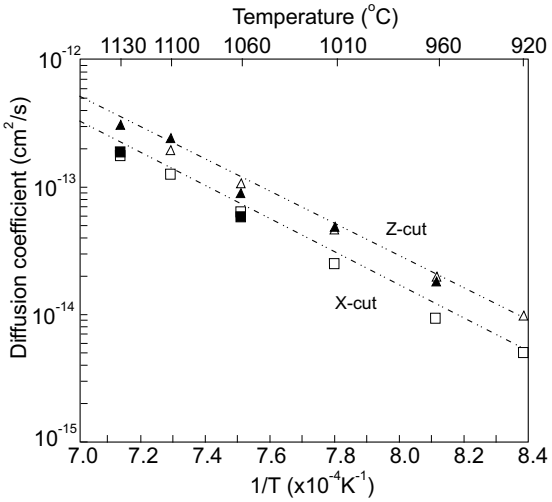

Figure 2.5: Arrhenius plot of diffusion coefficient of erbium into $LiNbO_3$ for diffusion parallel to the *c*-axis - Z-cut - (triangle) and perpendicular to the *c*-axis - X-cut - (squares) of the $LiNbO_3$ crystal obtained by SIMS (white) and SNMS (black) measurements. (From Ref. [17]).

The Er-diffusion parameters have been investigated and determined on X-cut substrate in our laboratory [41] to have a good overlap of the Er-doping profile with

the optical waveguide modes. Though the optimization is not yet perfect, routinely a 22 nm thick Erbium layer is indiffused at 1130 ℃ during 150 hours. The corresponding surface concentration is $\sim 2.0 \times 10^{20}\, cm^{-3}$.

The Erbium atom has the electronic configuration as $[Xe]4f^{11}5d^{1}6s^{2}$. It cedes the two $6s^2$ and one $4f$ electron and is incorporated as Er^{3+} ion in a $LiNbO_3$ host. The energy level diagram and optical transitions of Er^{3+} ions in Er:$LiNbO_3$ are shown in figure 2.6(a) [96]. The energy levels $^4I_{13/2}$ and $^4I_{15/2}$ are important as laser transitions in the $\lambda = 1.55\,\mu$m range can take place between these levels and they are shown in the inset in more detail (figure 2.6(b)). The $^{2S+1}L_J$ energy levels are split due to the Stark

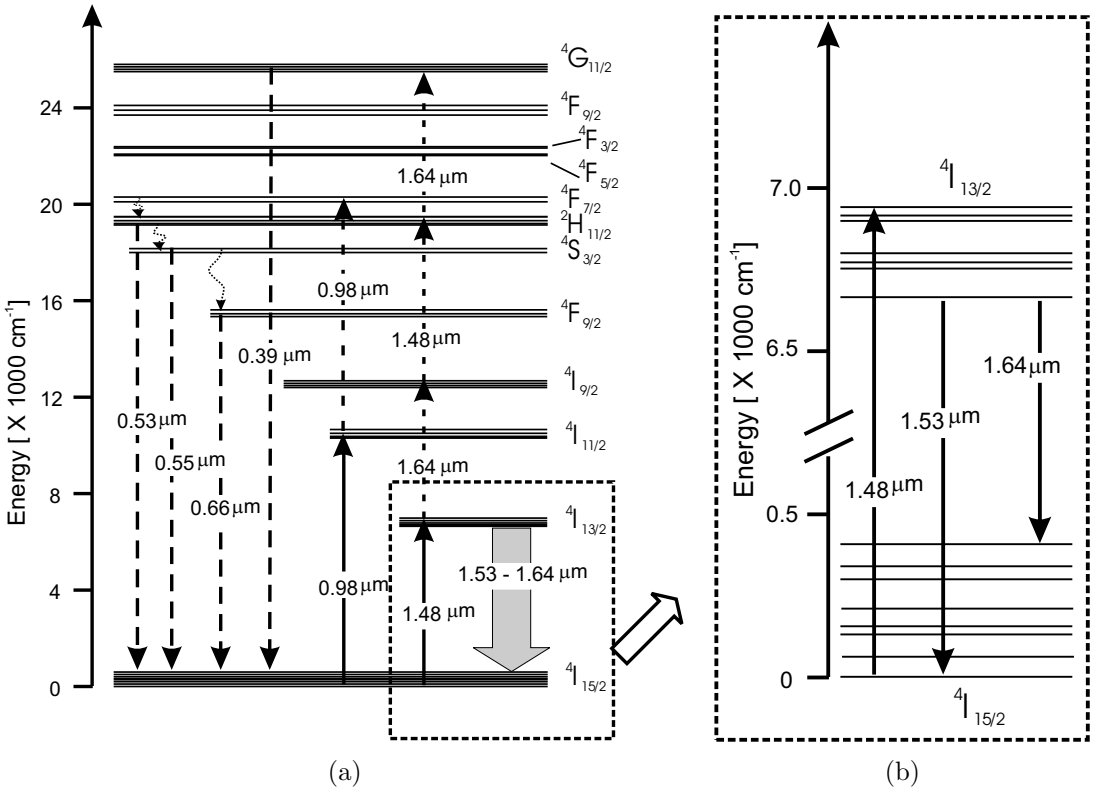

Figure 2.6: (a) Erbium energy level diagram after [96] with possible optical transitions. (b) Enlarged part of the diagram with the Stark splitting of the lower laser level $^4I_{15/2}$ and the upper laser level $^4I_{13/2}$. The energy scale is given in reciprocal wavelengths (cm^{-1}) as usual for spectroscopy.

effect in $J + \frac{1}{2}$ sublevels[1]. The local electric field in the $LiNbO_3$ crystal is responsible for this splitting. The $4f^{11}$ electron configuration leads to the ground state $^4I_{15/2}$; it is split into eight doubly degenerate levels by the Stark effect and the first excited state $^4I_{13/2}$ is split into seven Stark sub-levels. The most interesting transitions (to get amplification and lasing in the telecommunication window) occur between these manifolds leading to absorption at around $1.48\,\mu$m wavelength and optical amplification by stimulated emission in the wavelength range $1.53\,\mu\text{m} < \lambda < 1.64\,\mu$m.

[1] S:quantum number of the spin angular momentum, L:that of the orbital angular momentum and J: that of the total angular momentum

The fluorescence lifetime of the $^4I_{13/2}$-level is measured to be $\sim$ 2.6 ms [97], relatively well suited as a metastable upper laser level. If with proper pumping a population inversion is achieved between the levels $^4I_{15/2}$ and $^4I_{13/2}$, optical amplification of a signal takes place and lasing starts when the amplification overcomes total round trip loss of the cavity. It is clear from the figure 2.6(b) that the 1.53 μm transition belongs to a quasi three level system and the transition with the wavelength 1.64 μm is related to a quasi four level system (the expression quasi is used because the occupation is given by the Boltzmann Statistic). It is seen from the energy level diagrams that $^4I_{13/2}$ level can be excited by pump light at 1.48 μm wavelength. It is also ideal for single mode operation since it is possible to fabricate single mode waveguides for the wavelength range 1.48 μm$< \lambda <$ 1.64 μm. Also there are excited state absorptions or up-conversion processes for pumping at 1.48 nm (see upward pointing dashed arrows in figure 2.6(a)). From this figure, it is clear that this process is strong if the waveguide is pumped with 0.98 μm wavelength source. As a result, fluorescence can also be observed in the wavelength range $\sim$660 nm, $\sim$550 nm and $\sim$390 nm (see downward pointing dashed arrows in figure 2.6(a)).

Optical amplification in the wavelength range 1530 nm$< \lambda <$1620 nm has been intensively investigated for different Er doping levels in two different configurations: single pass and double pass [98]. In the latter case, a highly reflecting broadband mirror has been deposited on the rear end face of the waveguide to double the interaction length of pump and signal modes. Theoretical modelling and analysis of optical amplification in a Ti:Er:$LiNbO_3$ waveguide are described in references [99,100]. Some results of small signal gain measurements for different Er-doping levels in X-cut $LiNbO_3$ are also reported previously [41]. The measurement of gain is performed for an optical waveguide structure containing four polarization splitters to realize a double stage acoustooptical filter with internal amplification. Due to extra losses in the polarization splitters the net gain is very low and double pass pumping in TM polarization only shows a gain of about 4 dB at 1531 nm at a coupled pump power of 260 mW at 1480 nm wavelength. This result indicates that further improvement is required for design and fabrication of polarization splitters.

The optical absorption characteristics of Er:$LiNbO_3$ is measured in a straight waveguide for the laser sample pb164x_y. In this sample, the surface concentration of Er is about $2.0 \times 10^{20}\, cm^{-3}$. The optical gain characteristics for single pass pumping is measured in Er-doped laser structures with two polarization splitters as shown in figure 2.1. The same experimental setup (as shown in figure 2.7) is used to investigate the optical absorption and the gain of the amplifier. Wavelength division multiplexers (WDM) are not necessary for the absorption measurement because absorption is studied in the absence of pump light. But those are used during the gain measurement where pump (λ_P) and signal (λ_S) are combined and coupled into the input of the waveguide and decoupled at the output.

To study the absorption characteristics of a Ti:Er:$LiNbO_3$ waveguide, a low power broad band fiber coupled superluminescent light emitting diode (SLED) is used as a light source. It has 200 nm emission bandwidth centered at wavelength 1550 nm. The output from the SLED is launched into a straight Er-doped waveguide from the left

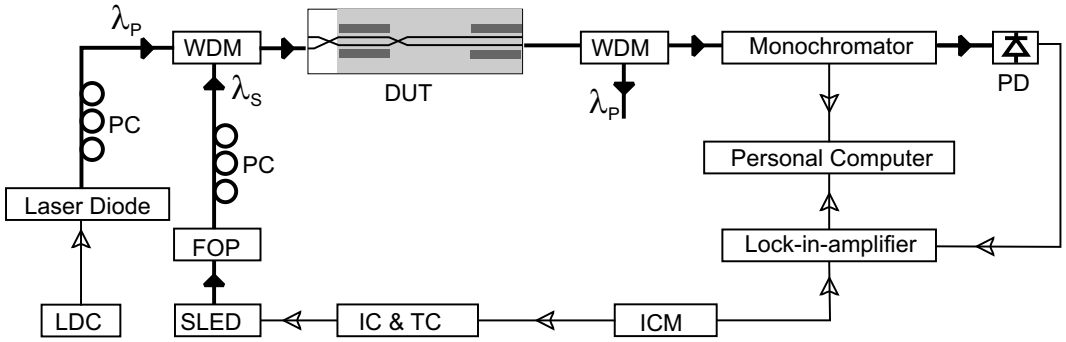

Figure 2.7: Schematic diagram of the experimental setup for absorption and gain measurement. DUT: device under test, here the waveguide amplifier, WDM: wavelength division multiplexer, PD: photodiode, PC: polarization controller, FOP: fiber optics polarizer, LDC: laser diode current controller, SLED: superluminescent light emitting diode, IC & TC: injection current and temperature controller for SLED, ICM: injection current modulator for SLED

hand side via one in-line fiber polarizer and one polarization controller. The incident power on the waveguide end face is about 0.5 mW. The output from the other end of the waveguide is fed to a monochromator (resolution bandwidth approximately 0.1 nm). The monochromator output is collected on a photodiode. The optical power received by the photodiode is very low due to the absorption by Er^{3+} and also due to the spectral filtering by the monochromator. Therefore, a lock-in-technique is used by modulating the injection current of the SLED and the lock-in signal is recorded as a function of the wavelength. With similar coupling conditions the transmitted optical power through an undoped (without Erbium) straight waveguide is also recorded as a function of the same wavelength range. The ratio of these two transmitted signals gives the wavelength dependent absorption characteristics (as shown in the figure 2.8 for TE and TM polarized input).

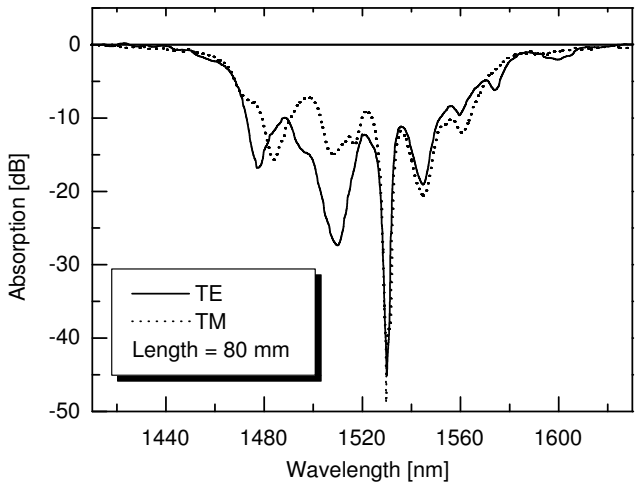

Figure 2.8: Absorption characteristics of a Er-doped straight waveguide for both polarizations of the signal. Length of the waveguide in the Er-doped section is 80 mm.

The absorption characteristics in the wavelength region from 1410 nm to 1630 nm are shown here for a 80 mm long (length of the Er doped section only) X-cut Y-propagation Ti:Er:$LiNbO_3$ waveguide. For TE-polarized light, the absorption dip is –17 dB at $\lambda = 1477.5$ nm whereas for TM-polarized light it is – 15.5 dB at $\lambda = 1483.5$ nm. Therefore, for efficient pumping of the amplifier in two different polarizations, pump sources of corresponding wavelengths are required. Since the absorption bands in these wavelength region are wide, one laser diode of 1480 nm emission wavelength is a compromise and can be used in both polarizations. Above 1530 nm wavelength, the absorption levels are nearly the same for both polarizations with slight differences at the dips at 1545 nm, 1561 nm, and 1575 nm.

The same setup is used to study the gain in laser structures, see figure 2.7. However, now a fiber Bragg grating stabilized laser diode at 1480 nm wavelength is used as pump source. Pump light (λ_P) from the laser diode and signal light (λ_S) from the SLED are coupled into the waveguide via a wavelength division multiplexer (WDM) with individual polarization controllers. A higher gain of the signal is observed when both signal and pump light have the same state of polarization in comparison with the opposite states of polarizations between them. The pump is decoupled from the signal at the output with another WDM before the monochromator. When the power level of the pump is sufficient to create a population inversion the signal will be amplified. To detect the amplified signal (without the amplified spontaneous emission), a lock-in-technique is used by modulating the injection current of the SLED. The signal output is recorded from the lock-in-amplifier as a function of wavelength from the monochromator reading. A comparative study of the gain of different laser structures shows that the laser structure with $L_c = 330$ μm has the highest gain. This result matched with the result obtained from the measurement of the polarization splitting ratio in the undoped laser structure where the splitting ratio was the lowest for this structure. Figure 2.9 shows the gain characteristics when both signal and pump are in TM polarization for three different input (incident) pump power levels. When the incident pump power is 135 mW, there is a nearly continuous gain in the wavelength range $1530\,\text{nm} < \lambda < 1580\,\text{nm}$ with a gain peak of nearly 5 dB at $\lambda = 1531$ nm. There is still absorption around 1537 nm wavelength, which is possible to overcome if we use double pass pumping in a laser cavity with the same level of incident pump power.

The wavelength dependent gain is also measured for TE polarized pump and signal. For the same (like TM polarized) incident pump power, it is seen that the gain for TE polarization is a bit smaller than for TM polarization. This can be understood from the waveguide loss and polarization splitter properties and different absorption and emission cross sections. Also, since the TE and TM mode sizes are different (mode size in TM is larger than that in TE, see figure 2.3), the gain is different due to a different overlap of mode profile and Erbium distribution profile inside the waveguide. The gain characteristics for TE polarization is not shown here because the result is not stable in time. Since a TE polarized wave is extra-ordinary in X-cut $LiNbO_3$ substrate, the photorefractive effect (or damage) is quite prominent at high pump power levels which causes an unstable result.

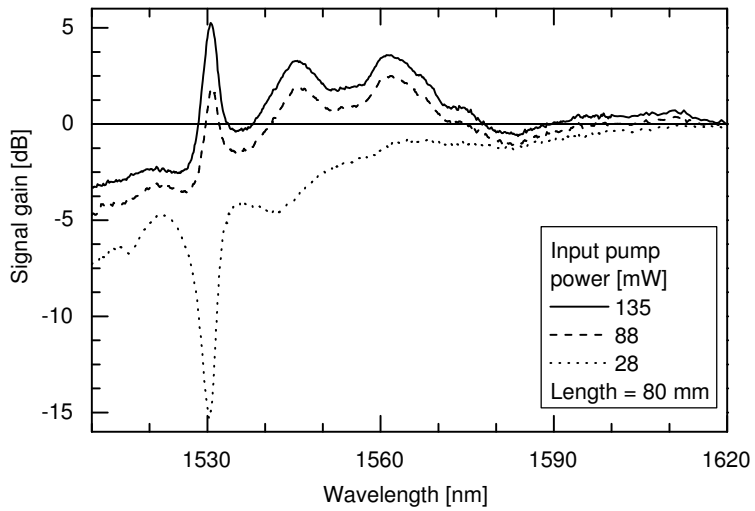

Figure 2.9: Gain characteristics of the laser structure (shown in figure 2.2) when both signal and pump waves are in TM polarization. Length of the waveguide in the Er-doped section is 80 mm.

2.5 Acoustooptical Polarization Converter and Frequency Shifter

In integrated optical devices TE↔TM polarization conversions are achieved through a periodic perturbation of the optical wave guiding medium via electrooptic and/or acoustooptic effects. Because of its wavelength selectivity and wide tunability, acoustooptical (AO) polarization converters have been used widely to realize optical wavelength filters, multiplexers/switches etc. for applications in optical communications [101,102]. It is used also as modulators, e.g., for integrated heterodyne interferometric sensors [103]. Such a converter is also used as an intracavity element in integrated lasers for emission wavelength selection, tuning and frequency shifting of the oscillating optical field [40, 88]. The integrated laser needs to achieve a complete transfer of optical power from one polarization to another at the selected optical wavelength. Otherwise, the unconverted optical power will contribute to the optical loss in the cavity. Through an efficient AO polarization converter it is possible to achieve a complete conversion between TE↔TM modes with a reasonable strength of the excited surface acoustic wave within a short interaction length. Homogeneity of the optical waveguide and good overlap between guided optical modes and excited surface acoustic wave are to be assured for this purpose.

Acoustooptical TE↔TM mode conversion is of particular interest here because of its wide optical wavelength coverage and easy implementation on a $LiNbO_3$ substrate. X-cut Y-propagation orientation of $LiNbO_3$ is chosen for this purpose. Compared to Y-cut X-propagation, the chosen orientation has the advantages of enhanced photoelastic effect and stronger piezoelectric coupling for surface acoustic wave excitation [104]. A schematic diagram of such an AO mode converter is shown in figure 2.10. In the figure x, y, z directions are shown for the wave propagation coordinate

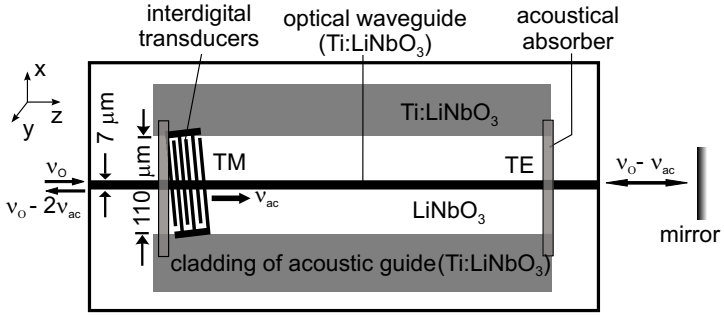

Figure 2.10: Schematic diagram of an acoustooptical (AO) polarization mode converter/frequency shifter configured for a homogeneous and collinear AO interaction. The 7 μm wide optical waveguide (Ti:$LiNbO_3$) is embedded within the 110 μm wide acoustic waveguide (with $LiNbO_3$ core) defined by the Ti-indiffused claddings. A TM wave of frequency ν_0 is converted to a TE wave of frequency $\nu_0 - \nu_{ac}$ due to the AO interaction with a phase matched SAW frequency of ν_{ac} and again converted back to a TM wave of frequency $\nu_0 - 2\nu_{ac}$ when it travels in opposite direction. x, y, z define the coordinate system for the wave propagation. Acoustical absorber limit the SAW propagation.

system. The axes of the substrate are shown in figure 2.2. On the $LiNbO_3$ substrate a 110 μm wide acoustic waveguide is formed by defining its claddings by a thick Ti indiffusion (typically 160 nm thick Ti stripes are indiffused at 1060 °C for 24 hours). Due to the high concentration and deep indiffusion of Titanium in this cladding region, mechanical stiffness is increased to enhance the phase velocity of the surface acoustic wave (SAW) [105]. So SAW guiding is achieved in the $LiNbO_3$ core region where the velocity of a SAW is lower. Later, a 7 μm wide Ti indiffused single mode optical waveguide is embedded into the core of the acoustic waveguide. Then 500 nm thick Aluminium interdigital transducers are fabricated by sputtering and lift-off photolithography technique. The transducer consists of 20 finger pairs with a period of 21.5 μm (of which 5.4 μm lines and space) between the pairs, inclined 5° away from the $+Z$-axis toward $+Y$ direction, yielding a center frequency of about 170 MHz for tuning the optical wavelength around 1550 nm. The SAW is excited by applying a sinusoidal RF-signal to the interdigital transducer. It interacts with the guided optical wave propagating through the optical waveguide. Acoustical absorbers are placed to absorb the SAW which effectively limits the AO interaction length. SAWs produce surface ripples as well as periodic changes of the index of refraction or more precisely a periodic variation of the dielectric permittivity of the surface layer of about one wavelength (of SAW) in depth. That is enough to provide a strong interaction with the guided optical wave.

The device is configured for a collinear interaction between the SAW and the guided optical wave. Collinear interaction has the advantage that the interaction length is large which requires less power of the SAW for polarization conversion. But it has a disadvantage that converted and unconverted part of the optical wave remain confined in same optical waveguide and a means must be used like the polarization splitter for their separation. This collinear interactions can be codirectional or contradirectional when a SAW propagates in the same or opposite direction, respectively, with respect

to the propagation of the optical wave. Many workers have studied this collinear interaction for AO polarization conversion to optimize the design of the converter [35,106–111]. We may have a brief discussion about the controlling parameter for this optimization [43,112–114].

The AO polarization conversion is achieved through the changes of the dielectric tensor created mainly by two effects: (a) the photoelastic and (b) the electrooptic effect. The dielectric permittivity change due to the photoelastic effect can be given by

$$\Delta\left(\frac{1}{n^2}\right)_{ij} = \Delta\epsilon_{ij} = \sum_{kl} p_{ijkl} S_{kl} \tag{2.1}$$

where p_{ijkl} are the photoelastic constants measured at constant electric field and the S_{kl} are the acoustic strain components. In case of piezoelectric crystals, like $LiNbO_3$, the acoustic strain is accompanied by electric fields which create a change of the dielectric permittivity through the electrooptic effect given by

$$\Delta\epsilon_{ij} = \sum_{k} r_{ijk} E_k \tag{2.2}$$

where the r_{ijk} are the electrooptic coefficients measured at constant strain and the E_k are the piezoelectrically produced electric fields.

This perturbation can be presented as a distributed polarization source, $P_{pert}(\mathbf{r},t)$ with $\mathbf{r}$ being a position vector, which is given by

$$[P_{pert}(\mathbf{r},t)] = \frac{\epsilon_i \epsilon_j}{\epsilon_0} \times \left[\sum_{kl} p_{ijkl} S_{kl}(\mathbf{r},t) + \sum_{k} r_{ijk} E_k^{ac}\right] E_j(\mathbf{r},t) \tag{2.3}$$

where ϵ_i, ϵ_j are the relative permittivity of the substrate, ϵ_0 is the permittivity of vacuum, E_j is the electric field of the unperturbed input optical waves, E_k^{ac} is the electric field generated by the SAW. Through this perturbation vector and the conservation of total power, we obtain the coupled mode equation for amplitudes A_{TE} and A_{TM} for TE and TM modes, respectively: (considering TM input travelling along z direction)

$$\begin{aligned}\frac{dA_{TE}}{dz}\exp\left[i(\omega_{TE}t + \beta_{TE}z)\right] &= -i\,\kappa\, A_{TM}\left[\exp\left\{i[(\omega_{TM}+\Omega)t - (\beta_{TM}+K_{ac})z]\right\}\right. \\ &\quad \left. + \exp\left\{i[(\omega_{TM}-\Omega)t - (\beta_{TM}-K_{ac})z]\right\}\right]\end{aligned} \tag{2.4}$$

where κ is the coupling coefficient between acoustic and optical modes, ω_{TE}, ω_{TM} and Ω are the frequencies of the optical TE, TM modes and acoustic waves, respectively; β_{TE}, β_{TM} are the propagation constants of TE and TM modes, and K_{ac} is the acoustic wave vector.

The coupling coefficient can be calculated by the overlap integral of optical field distributions $\mathbf{E}_{TE}(x,y)$ and $\mathbf{E}_{TM}(x,y)$ with the acoustooptically changed dielectric tensor $\Delta_{\underline{\underline{\varepsilon}}}$ by integrating over the area of the waveguide cross-section S and is given by

$$\kappa = \iint_S \mathbf{E}_{TM}^*(x,y).\Delta_{\underline{\underline{\varepsilon}}}.\mathbf{E}_{TE}(x,y)dxdy \tag{2.5}$$

Equations 2.4 and 2.5 describe the z dependence of TM–TE coupling for a collinear AO interaction. As a result of the electrooptic and photoelastic effects, the coupling between TM and TE modes takes place whenever the dielectric tensor has off-diagonal elements ϵ_{xy} and ϵ_{zy}.

In this optical waveguide $\beta_{TM} > \beta_{TE}$. To achieve an efficient polarization conversion the interaction must be phase-matched: the difference between the wave numbers of the optical modes must be compensated by the wave number of the SAW. So, in the TM–TE mode coupling, in particular, optical wavelength has to be adjusted by the wavelength of the SAW. For this codirectional interaction it is adjusted such that (from 2nd term in the right hand side of equation 2.4)

$$\begin{aligned} \beta_{TE} &= \beta_{TM} - K_{ac} \\ \text{and the resulting frequency is} \quad \omega_{TE} &= \omega_{TM} - \Omega \end{aligned} \tag{2.6}$$

So the frequency of the converted TE wave is downshifted. In case of contradirectional propagation we have

$$\begin{aligned} \beta_{TE} &= \beta_{TM} + K_{ac} \\ \text{and the resulting frequency is} \quad \omega_{TE} &= \omega_{TM} + \Omega \end{aligned} \tag{2.7}$$

So the frequency of the converted TE wave is upshifted. It is shown in the figure 2.10, that for TE mode optical input and for a contradirectional interaction, the frequency of the generated TM mode output is downshifted again. So in a round trip travel of a optical wave through the polarization converter leads to its two polarization conversions with two frequency shifts in the same direction. Thus, the direction of the frequency shift due to an AO polarization conversion can be summarized as shown in table 2.3.

Table 2.3: Direction of frequency shift in the acoustooptical polarization conversion process

Direction of SAW with respect to optical wave	Input polarization	
	TM	TE
Codirectional propagation	–	+
Contradirectional propagation	+	–

In this AO interaction, the phase match condition, or the condition where the complete power transfer between TE and TM takes place is given by:

$$K_{ac} = \beta_{TM} - \beta_{TE} \tag{2.8}$$

Then the exact phase matching frequency ν_{ac} of the SAW for the optical wavelength λ is given by

$$\nu_{ac} = \frac{v_s}{\lambda} \left| n_{eff}^{TM} - n_{eff}^{TE} \right| \tag{2.9}$$

where $n_{eff}^{TM,\,TE}$ are the effective refractive indices of the propagating modes TM and TE, respectively, and v_s is the SAW velocity. The phase matching condition makes the conversion process wavelength selective.

In this coupling another important parameter δ, which is the measure of phase mismatch is defined as

$$\delta = K_{ac} - (\beta_{TM} - \beta_{TE}) \tag{2.10}$$

The conversion efficiency is defined as the ratio of converted power P_{TE} at $z = L$ (L: interaction length), to the input power P_{TM} at $z = 0$ and is given by

$$\eta = \frac{P_{TE}|_{z=L}}{P_{TM}|_{z=0}} = \kappa^2 L^2 \frac{\sin^2\left(\sqrt{\kappa^2+\delta^2}.L\right)}{\left(\kappa^2+\delta^2\right).L^2} \tag{2.11}$$

In perfect phase-matching (i.e., $\delta = 0$), the conversion efficiency η is given by

$$\eta = \sin^2\left(\gamma\sqrt{P_a}\ L\right) \tag{2.12}$$

where γ is a constant determined by the overlap integral κ and P_a is the power of the SAW. The required interaction length L (say, $=l_c$) for complete conversion from one polarization to the other (between TM and TE of same order) can be expressed as

$$L = \frac{\pi}{2}\frac{1}{\gamma\sqrt{P_a}} \tag{2.13}$$

So, it is obvious that if γ is fixed by the fabrication parameters, the TM↔TE conversion can be achieved with low power level of SAW if the interaction length is long.

Following this discussion, it is evident that the coupling constant κ and the phase mismatch δ are the two most important factors to determine the performance or conversion efficiency of the AO polarization converter. κ includes the effects of dielectric perturbation due to the SAW and the optical field distributions of the guided modes (see equation 2.5). The modal birefringence $\left(\Delta n = \left|n_{eff}^{TM} - n_{eff}^{TE}\right|\right)$ determine the phase mismatch δ.

In the AO polarization converter as shown in figure 2.10, the TM↔TE conversions are achieved by a homogeneous coupling of a constant SAW intensity along the interaction length. The effective coupling strength as the function of propagation direction coordinate (z) is shown in figure 2.11(a). The resultant conversion characteristics, i.e., the power of the converted optical wave as function of the optical wavelength is a sinc^2-like function (shown in figure 2.11(b)). Disadvantages of such devices are the high sidelobes of about –10 dB. The spectral conversion characteristic is approximately given by the Fourier transform of the coupling strength. Therefore, to reduce the sidelobes, a weighted coupling technique (apodization) has been successfully applied by designing the AO polarization converter using acoustical directional couplers [39, 116–118]. Instead of this abrupt changes in the coupling strength at the beginning and at the end, within the interaction length a soft onset and cutoff are

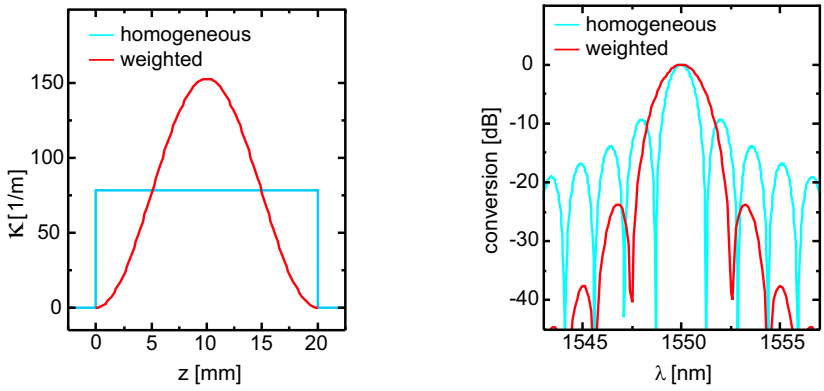

(a) (b)

Figure 2.11: Comparison between homogeneous coupling and weighted coupling in the AO interaction. (a) Profile of the coupling strength κ and (b) the corresponding calculated mode conversion versus wavelength λ [115].

achieved in this design. Such a weighted coupling strength and the corresponding conversion characteristics is shown in figure 2.11 in comparison with a homogeneous coupling strength in the same scale. For both types of coupling, the interaction length is limited to one complete conversion period ($l_c = 20$ mm as shown in figure) only.

The design of an AO polarization converter with a tapered acoustical directional coupler for the weighted coupling is shown in figure 2.12(a). One of the acoustical

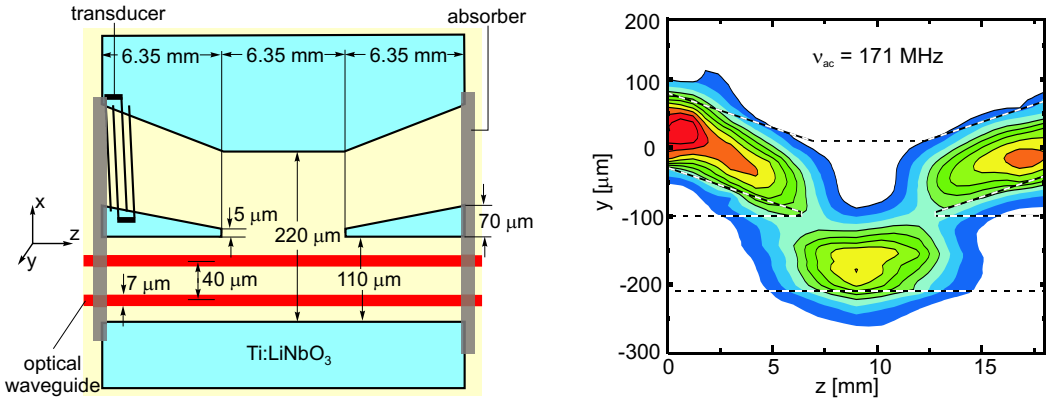

(a) (b)

Figure 2.12: (a) Design of the acoustooptical mode converter with tapered acoustical directional coupler configured for weighted coupling and (b) contour plots of the measured intensity distribution of SAW for the acoustical directional coupler shown in (a). (Ref. [117,118]

waveguides, in which the optical waveguides are embedded, is straight, whereas the other one is tilted outward at the end sections. The gap is linearly reduced from 70 μm from both ends to 5 μm (as shown in figure 2.12(a)) and in the middle section the gap is zero. The structure gives a weak coupling in the outer sections whereas in the zero-gap section strong coupling occurs. The coupler properties are characterized by

measuring the intensity profile of the SAW using a laser probing technique [119, 120]. An example is shown in figure 2.12(b) as contour plot with different steps of intensity up to 95%. The SAW is excited in the upper part of the left guide via the interdigital transducer, it couples to the adjacent guide almost completely and afterwards it is guided back.

2.6 Acoustooptically Tunable Wavelength Filter

The wavelength selective components in integrated optics, like filters, multiplexers, switches are realized using the 'phase match' property of the AO polarization converters as stated in equation 2.8. Since $\delta\beta = \beta_{TM} - \beta_{TE}$ varies with the optical wavelength λ, a wavelength selective TE↔TM conversion is achieved, if K_{ac} is given by a SAW of specific frequency. The phase matching wavelength λ is thus tunable by changing the length of the acoustic wave vector K_{ac}–that is, by changing the SAW frequency ν_{ac}. For a collinear interaction using guided optical waves, the wavelength filtering can be achieved using waveguide polarization splitters at the input/output ports of the device to separate the TE and TM modes. The most important property of AO polarization converters/filters is their large wavelength tuning range. Its narrowband ($\simeq 2\,\mathrm{nm}$) filter response and low power level of driving SAW ($< 100\,\mathrm{mW}$) are other interesting properties for integrated optical devices. A schematic diagram of a polarization independent AO filter is shown in figure 2.13 which consists of two waveguide polarization splitters and an AO polarization converter with a tapered acoustical directional coupler in between.

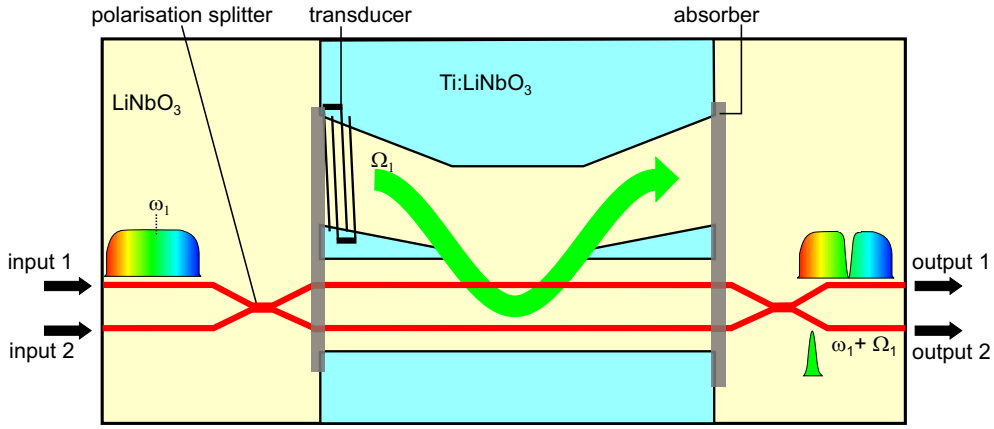

Figure 2.13: Polarization independent AO filter: an AO polarization converter between two waveguide polarization splitters. Filter action: if a broadband optical input (in any state of polarization) is launched at port input-1, the phase-matched (say, optical frequency ω_1 with SAW frequency Ω_1) frequency shifted (to $\omega_1 + \Omega_1$) orthogonally polarized narrowband 'filtered' optical output is emitted through port output-2.

Since the polarization splitters are designed to route TM polarized light into the bar state and TE polarized light into the cross state, when there is no AO interaction,

any broad-band optical signal in either polarization from the port input-1 will appear completely at port output-1. If the input is TE-polarized (TM-polarized), it will travel through the lower waveguide (upper waveguide) between the two splitters. If a SAW of angular frequency Ω_1 is excited and if it satisfies the phase-match condition with an optical signal of angular frequency ω_1, this signal of frequency ω_1 will experience a polarization conversion and it will be guided to the port output-2 with a frequency shift to $\omega_1 + (-)\,\Omega_1$. So a filter action takes place between port input-1 and port output-2. Same thing is true between port input-2 and port output-1.

Tuning of the filter is performed by changing the frequency of the RF generator driving the SAW. A typical experimental tuning curve is shown in figure 2.14 [35, 36]. These experimental data are given from a device prepared only to study the filter characteristics. For a given SAW frequency the peak wavelength of the filtered output is measured by an optical spectrum analyzer. The power of the RF signal (thereby the intensity of the SAW) is adjusted to achieve maximum conversion for different wavelength. A tuning range of 100 nm is observed with a tuning slope of –8.2 nm/MHz. The tuning range is mainly determined by the electrical bandwidth of the transducer.

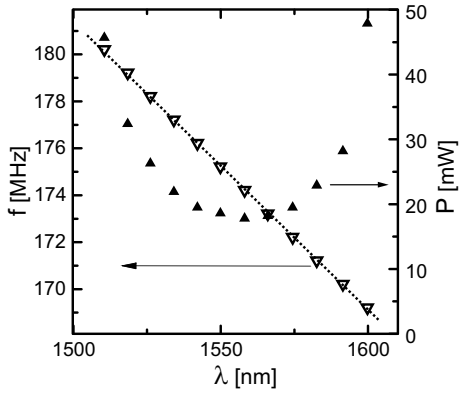

Figure 2.14: Tuning characteristics of AO filter: (Ref. [121]) (a) phase-matched acoustic frequency (left ordinate) and (b) electrical drive power of on the transducer for maximum conversion (right ordinate).

Another interesting feature of this acoustooptical wavelength filter is that simultaneous filtering for a set of optical wavelengths is possible by applying a set of corresponding SAW frequencies [36, 122]. In figure 2.15(a) this multiwavelength operation is demonstrated for two wavelength channels separated by 8 nm, when the filter has been driven by corresponding two RF signals simultaneously. The maximum conversion at both wavelengths can be adjusted separately by controlling the power levels of the corresponding RF signals. The SAW frequencies can be controlled in such a way that two filter pass bands can come close to each other to form a single pass band with wider spectral bandwidth as shown in figure 2.15(b).

When two SAWs of different frequencies are excited simultaneously in the same region of the acoustic waveguide, each SAW generates a travelling grating with a period

given by the acoustical wavelength. These two gratings of different periods can interfere with each other resulting in a time-dependent acoustooptical coupling strength and, therefore, in a time-dependent efficiency of the conversion process. A theoretical study of such interference is described in reference [122]. The spectral properties of a laser emission have yet to be studied theoretically when such an intracavity filter is operated by simultaneous two SAWs frequencies.

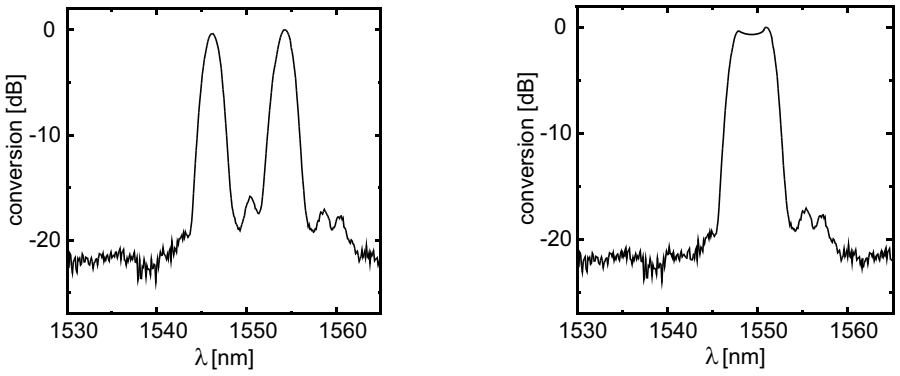

Figure 2.15: Simultaneous multi wavelength filtering: (Ref. [121]) (a) Two different optical wavelengths are filtered by applying simultaneously two RF-signals of different frequencies. (b) By adjusting the RF frequencies a single optical bandpass filter of large bandwidth is achieved.

The exact values of the parameters, like conversion efficiency and phase matching frequency of an AO polarization converter (as defined by the equations 2.11 and 2.9, respectively) depend on the fabrication process. So experimental studies are required to obtain those parameters after the fabrication. Also the polarization splitting ratio of the polarization splitters is needed to be evaluated experimentally. Therefore, an experimental study is performed to learn to know the filter characteristics of the developed sample pb164x_y. The schematic diagram of the experimental setup to study the characteristics of an AO filter and an AO polarization converter is shown in figure 2.16. There is a pair of optical waveguides common to both AO polarization converters. The positions of the polarization splitters indicate that the AO polarization converter at the left hand side is part of the AO filter. The AO filter with the polarization splitters having L_c= 330 μm is chosen for the experimental study for its good polarization splitting ratio, which is approximately –30 dB. The characteristics of two polarization converters are studied separately.

In the experiment the single frequency laser emission at 1557 nm wavelength from an External Cavity Laser (ECL) is launched into the input port A_1 in TM polarization and the corresponding output from port B_1 is focused to a photodiode after passing through a polarizer (TM-pass). To study the AO filter properties the SAW is excited in the acoustical waveguide of the first AO polarization converter only by connecting the corresponding transducer electrode to a RF generator via the impedance matching circuit and amplifiers, as shown in figure 2.16. The SAW frequency is varied in the range from 169 MHz to 173.5 MHz with steps of 1.0 kHz. The AO polarization conver-

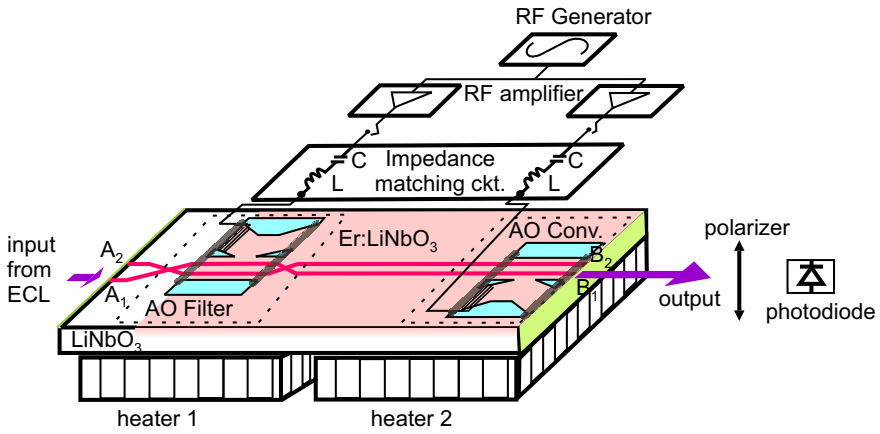

Figure 2.16: Schematic diagram of the experimental setup to study AO conversion characteristics. C: capacitor, L: inductor, ECL: external cavity laser.

sion (TM→TE coupling) can be studied by monitoring the corresponding photodiode output. Depending upon SAW frequency the polarization of the guided optical wave will be converted to TE polarization (as conversion efficiency depends on the phase mismatch δ defined by equation 2.11) and will be routed to the port B_2. So the photodiode output starts to decrease as it receives light only from port B_1. At some particular SAW frequency, the phase mismatch reduces to zero, the conversion reaches a maximum (indicated by the minimum transmission through output port B_1). For a further change of the SAW frequency, δ increases again which results in reduced polarization conversion. At the phase matched frequency of the SAW, the electrical drive power on the transducer, thereby the power of the SAW, is adjusted to achieve nearly zero transmission through the port B_1. Any increase or decrease in power from this value will reduce conversion efficiency (given by equation 2.12). At the optimized power level of 19.5 dBm, the conversion efficiency is measured as 97% and the corresponding AO conversion characteristics or therefore the AO filter characteristics is presented in figure 2.17(a). The phase matched SAW frequency corresponding to the optical wavelength 1557 nm is found to be 171.15 MHz and the filter bandwidth at FWHM is measured as 320 kHz.

Similarly, the polarization conversion properties of the 2nd converter on the right hand side are studied by exciting the SAW only with the corresponding transducer electrode. When the AO filter is not active, an input optical wave from port A_1 will remain in the lower optical waveguide after passing through the two polarization splitters. Since there is no polarization splitter at the output after this AO converter, the converted TE polarized light due to AO interaction will be blocked by the polarizer to reach the photodiode as shown in figure 2.16. The TM→TE conversion characteristics of this AO converter for the same range of SAW frequencies (169–173.5 MHz) is shown in figure 2.17(b). Here the phase matched frequency corresponding to the optical wavelength 1557 nm is observed as 171.68 MHz and the conversion bandwidth is measured as 370 kHz. The optimized electrical power for maximum conversion on this electrode is 17.8 dBm.

Comparing the two characteristics in figure 2.17(a) and figure 2.17(b) we see that TM→TE conversion up to 97% is achieved in both cases but with differences in phase matching frequency, required electrical drive power, conversion bandwidth, and sidelobes. Though the optical waveguides are common to both of the AO converters and also the acoustical directional couplers and transducers are fabricated simultaneously, these differences are due to inhomogeneities in the fabrication processes. For instance, a slight longitudinal variation of the waveguide width or the Ti layer thickness results in a shift of the effective indices of the waveguide modes and hence the phase match frequency [118]. This difference of the phase matching frequencies (approximately 530 kHz) is balanced by maintaining a temperature difference between these two converter regions. The arrangement for the heaters are shown in figure 2.16. To shift the phase match frequency of the 2nd AO polarization converter to that of the AO filter, temperatures of 20 ℃ and 25 ℃ are maintained through heater 1 and heater 2, respectively, with the aid of Peltier elements and proper thermal isolations.

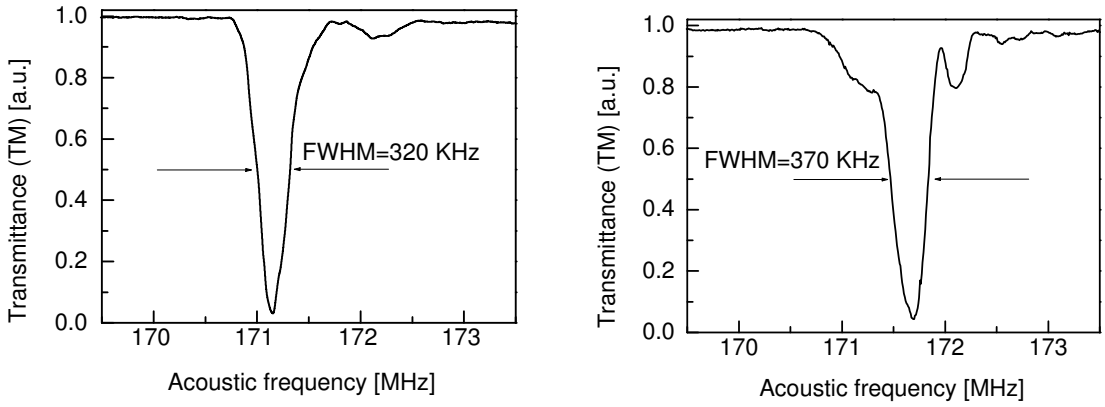

Figure 2.17: AO polarization conversion for TM polarized input through: (a) an AO filter, (b) an AO polarization converter. Though the fabrication parameters for AO filter and converter are same, the difference in phase-match frequencies arise due to inhomogeneities in the fabrication process.

To study the polarization conversion at different wavelengths, and thus, to see the tuning properties of the acoustooptical filter, broadband light from a SLED is launched into input port A_2 of the optical waveguide in TM polarization and the corresponding output from port B_1 is observed with an optical spectrum analyzer (OSA). The traces from the OSA are plotted in figure 2.18 for three different SAW frequencies. Due to the wavelength dependent emission of the SLED and absorption in the Er-doped waveguide, the power level of the transmitted waves at different wavelengths are not same. But to see the conversion characteristics clearly, the maximum power levels of the traces are normalized to one. The upper scale is showing the corresponding optical wavelength as recorded by the OSA. The tuning slope is observed as -8.2 nm/MHz. The filter linewidth (FWHM) is 2.5 nm. No significant sidelobe is observed.

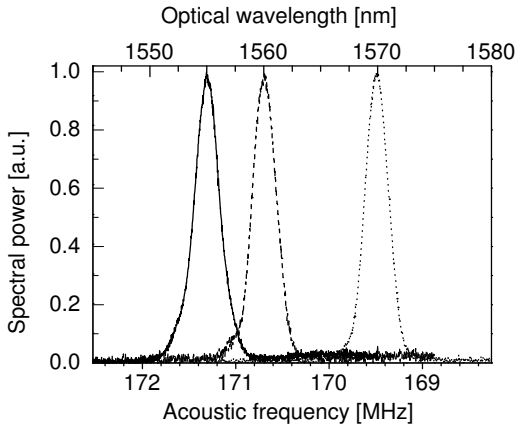

Figure 2.18: Filter characteristics at three different wavelengths. The peak spectral power is normalized to 1 for each spectrum.

2.7 Dielectric Coatings

For a tunable laser broad band high reflecting (HR) coatings are required at the waveguide end faces to form the laser cavity. Also for the efficient coupling of the input pump power an antireflection (AR) coating is required. The polarization independent AO filter has two inputs and two outputs to realize the filter action as shown in figure 2.13. From this figure, it is clear that a resonator with intracavity filter can be formed by depositing the mirrors on the end faces of the upper left input waveguide and the lower right output waveguide. Then the lower waveguide end face on the left hand side can be used as pump coupler; it is required to deposit an antireflection coating to improve the coupling efficiency.

The HR coating and AR coating are formed by alternating SiO_2 and TiO_2 quarterwave layers directly deposited onto the polished waveguide end faces. The characteristics of the dielectric coatings deposited on the end faces are studied on test glass surfaces which are coated simultaneously. The transmission of the coated test glass as a function of wavelength is recorded using a spectrophotometer (Perkin-Elmer Lamda 19). Then the data are corrected for a $LiNbO_3$ substrate considering the air-glass interface reflection of 4%. Figure 2.19 shows the resulting transmissions of the HR and AR coatings deposited on the end faces of the sample pb164x_y with laser structure. It is observed that at 1550 nm, the reflectivity (i.e., 1–transmission) of the HR coating is 97% and that of AR coating is 8% and at 1480 nm those are 96% and 8%. So for the laser cavity (formed by the end faces A_2 and B_1 of figure 2.16) both mirrors have the same reflectivity of 97%. The reflectivity of 96% at 1480 nm wavelength at the end face B_1 helps to reflect back the residual pump light into the waveguide (double pass configuration of pump) to enhance the gain compared to single pass gain as shown in figure 2.9.

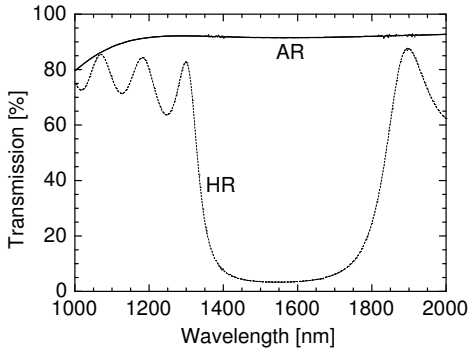

Figure 2.19: Measured transmission characteristics of broadband dielectric coatings for anti-reflection (AR) and high-reflection (HR). [These are fabricated and measured by our technicians].

2.8 Conclusions

The essential components for an integrated tunable laser are described individually in this chapter. Its required properties and functionalities are discussed briefly. The aim is to achieve an optimum performance of these components when they are monolithically combined to form an integrated tunable laser as shown in figure 2.1. This performance is investigated experimentally and presented in this chapter. A number of samples containing laser structures are investigated. The results are given from the best sample marked by pb164x_y in our laboratory.

Single mode waveguiding is observed in both polarizations over the wavelength range $1480 < \lambda < 1620$ nm. The scattering losses are found to be 0.05 and 0.15 dB/cm in TM and TE polarizations, respectively. Polarization dependent mode sizes are given in figure 2.3. For the polarization splitters, the best splitting ratio is observed to be –30 dB (TM polarized input) for $L_c = 330\,\mu$m. The Ti:Er:$LiNbO_3$ waveguide amplifier is characterized by measuring the wavelength dependent absorption and gain. The gain profile shows that for a 80 mm long amplifier section there are more than 3 dB gain in the wavelength range around 1560 nm and 5 dB gain at 1530 nm at the pump power level of 135 mW (incident) in TM polarization. AO polarization conversion and wavelength tuning properties of the AO filter are characterized by measuring the transmittance through the waveguide. A maximum conversion of 97% is observed for TM polarized input and the required power level of RF signal is about 19 dBm. The filter band width is observed to be 2.5 nm and the measured tuning slope is –8.2 nm/MHz. The transmission characteristics of the dielectric layers for broad-band anti-reflection and high-reflection coatings is also measured. All these results show that the performance of the individual components are good enough to develop an integrated tunable laser which will be discussed in the following chapters.

Chapter 3

Conventional Frequency Shift Compensated (FSC) Laser

3.1 Introduction

The design and characteristics of an integrated acoustooptical (AO) wavelength tunable filter have been introduced in the previous chapter. If this filter is used as an intracavity element of an integrated laser, the laser emission wavelength can be selected or tuned by selecting or tuning the frequency of the surface acoustic wave (SAW) by an electronic RF generator. Thus, the wavelength selective property of the AO interaction is utilized to develop electronically and widely tunable (few tens of nm) integrated lasers. The polarization converted optical wave experiences a frequency shift due to the AO interaction which leads to two different types of tunable laser operation. The first one is a conventional laser with the frequency shift compensated to fulfill the Fabry-Perot resonance condition in the cavity. The second one is a frequency shifted feedback (FSF) laser with the optical wave frequency shifted in each round trip in the cavity due to this AO interaction.

The design and operation of a conventional frequency shift compensated (FSC) laser and a detailed characteristics of its output will be described in this chapter. Issues of single mode emission and of mode-hop free tuning, will also be discussed. The operation and output characteristics of a FSF laser will be presented in the next chapter.

3.2 Laser Design

The most simple integrated waveguide laser is a free-running Fabry-Perot laser comprised of a waveguide amplifier with deposited end face mirrors. This laser is transformed into an advanced tunable laser if an AO wavelength filter is incorporated in the cavity.

Basic requirement for the operation of a conventional laser is that the oscillating optical field inside the cavity is reproduced in amplitude and phase after each round

trip. Depending on the optical path length inside the cavity this condition is satisfied only at a discrete set of frequencies known as cavity resonances. But it is explained in figure 2.10 that the frequency shift is doubled when an optical wave makes a round trip in the cavity with only one AO polarization converter. If for forward propagation the frequency of the optical wave is downshifted, the orthogonally polarized wave during the backward propagation experiences another downshift. So a frequency shift compensator is essential inside a conventional laser cavity. A second AO polarization converter inside the cavity can act as frequency shift compensator provided it satisfies the same phase-matching condition as the first one. In this situation, when the optical wave passes two polarization converters along one direction and the SAW propagates also in the same direction, the individual frequency shifts cancel each other due to the opposite state of polarization at the input of both polarization converters (see figure 3.1) [45,123]. So it is necessary that both AO polarization converters are driven simultaneously by one RF generator to excite the SAWs with the same frequency.

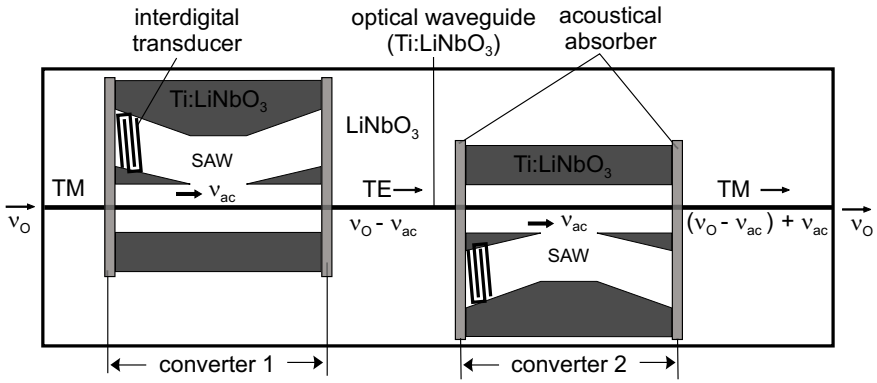

Figure 3.1: The frequency shift compensation with two AO polarization converters. A TM polarized optical wave of frequency ν_0 is converted to a TE polarized wave of frequency $\nu_0 - \nu_{ac}$ (downshifted) through the first AO polarization converter and is converted back to a TM polarized wave of frequency ν_0 (upshifted) through the second AO mode converter. In both converters SAWs (of frequency ν_{ac}) are codirectional with the optical wave.

If the required basic elements for an acoustooptically tunable waveguide laser and their properties are known, the laser can be designed. The schematic diagram of the laser is shown in figure 3.2. A X-cut, Y-propagation $LiNbO_3$ substrate is chosen for efficient excitation of the SAW for AO interaction. There are two Ti-indiffused single mode optical channel waveguides along the length of the substrate with two cross over regions. These cross over regions are the waveguide polarization splitters. These devices split the optical wave composed of two states of polarization (SOP) into two different waveguides after crossing the common waveguide section. Most of the substrate surface and thereby of the optical waveguides is doped by Er indiffusion except a small part at the left hand side of the structure including the first polarization splitter. The Er-doped waveguide section can provide the optical amplification in the wavelength range 1530–1620 nm if it is pumped optically with an external laser diode at 1480 nm wavelength.

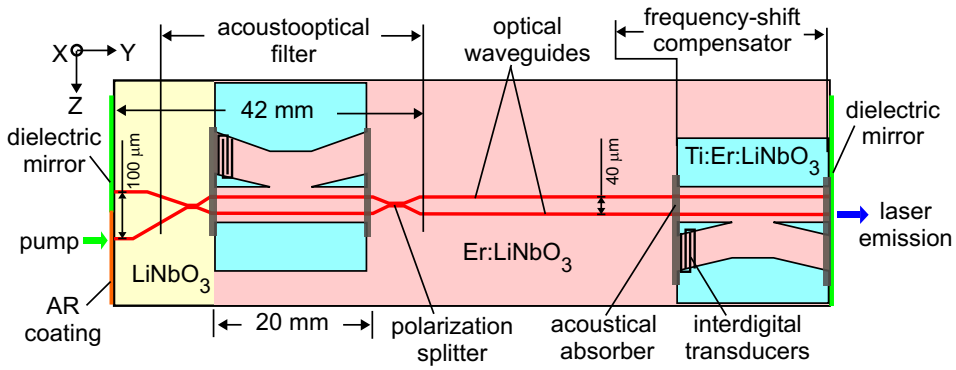

Figure 3.2: Schematic of the design of an acoustooptically tunable Ti:Er:$LiNbO_3$ waveguide laser. Basic elements and their positions are labelled. X, Y, Z are the crystal axes.

The laser cavity is formed by two broad-band multilayer dielectric mirrors deposited at both end faces of the waveguides. There is a broad-band multilayer antireflection (AR) coating at the left hand side on the end face of the lower arm of the first polarization splitter which facilitates efficient pump coupling. The mirror at the right hand side also serves as pump reflector to achieve double pass pumping. It is used as output coupler of the laser.

Since at the left hand end face only the upper waveguide branch is coated with a mirror, the waveguide resonators for both polarizations are now fixed. For TM (for TE) polarized pump, the resonator includes the lower (the upper) waveguide inside the filter region (compare figure 2.13). This will be explained in more detail in section 'laser operation' later. The upper waveguide branch at the right hand side is not used in this case. But it is useful for studying the characteristics of the polarization splitters and of the AO filter before the mirror deposition (those are described in the previous chapter). If at the left hand side the upper branch is used as pump input (with AR coating) and lower one (with dielectric mirror) as part of the laser resonator then the upper waveguide at the right hand side will become a part of the laser resonator.

There are two AO polarization converters in the cavity. The first one, at the left hand side between two polarization splitters is the essential component of the optical wavelength filter. The second converter at the right hand side serves as frequency shift compensator. The acoustical waveguides are defined such that the optical waveguides lie centrally inside the straight acoustical waveguide sections in both converters. Interdigital transducers at the beginning of each polarization converter can excite the SAWs. The propagation of the SAWs is stopped by acoustical absorbers (which can be a very thin sheet of plastics) at both ends of each polarization converter. So there are no SAWs outside the regions of polarization converters.

The separation between the two optical waveguides on the left hand side end face is 100 μm. The separation of the parallel waveguides is 40 μm. The length of the waveguides from the left hand end face to the end of the second polarization splitter, thereby, up to the end of the AO wavelength filter is 42 mm. The length of the second polarization converter is 20 mm. So the minimum length of such a laser structure

is 62 mm. If the substrate is longer than 62 mm, the second polarization converter can be shifted further right to the end of the structure. To avoid spatial hole burning effects (which will be explained later), both polarization converters should be free from Er doping. In this situation the length of the Er-doped optical waveguide between the two polarization mode converters should be long enough to provide the optical amplification for the laser to set in.

3.3 Laser Fabrication

The laser is fabricated on the –X face of a 94.2 mm long (along the Y-axis), 1 mm thick (along X-axis) and 12 mm wide (along the Z-axis) substrate. Er^{3+}:$LiNbO_3$ has a ground state absorption around the wavelength 1550 nm. To study and evaluate the optical and acoustooptical properties of the waveguide structure this absorption has to be avoided. On this Substrate 12 laser structures are fabricated monolithically parallel to each other with some straight optical waveguides as reference for measurement purpose. Only 6 of these structure are fabricated in the Er-doped surface as shown in figure 3.3. They only differ by the coupling length L_c of the polarization splitters. L_c is varied from 310 μm to 360 μm with steps of 10 μm (see figure 3.3).

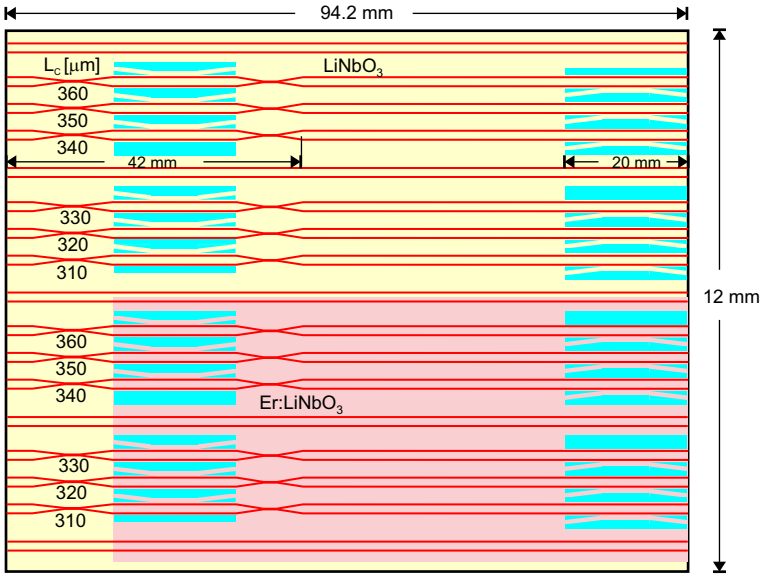

Figure 3.3: Mask layout for the laser sample. There are 12 laser structures, of which only 6 structures are fabricated in the Er-doped surface area and they differ in L_c as indicated in units of μm. Detailed dimensions of waveguides and AO directional couplers are given in the previous chapter, see figure 2.4(a) and 2.12(a), respectively.

The complete fabrication of the acoustooptically tunable laser can be divided into five major steps as shown in figure 3.4: (a) Er-diffusion-doping of the $LiNbO_3$ substrate, (b) Ti-indiffusion to define the claddings of the acoustical waveguides for AO directional couplers, (c) Ti-indiffusion to fabricate the optical waveguides and polarization splitters, (d) Al sputtering to form interdigital transducers and (e) deposition

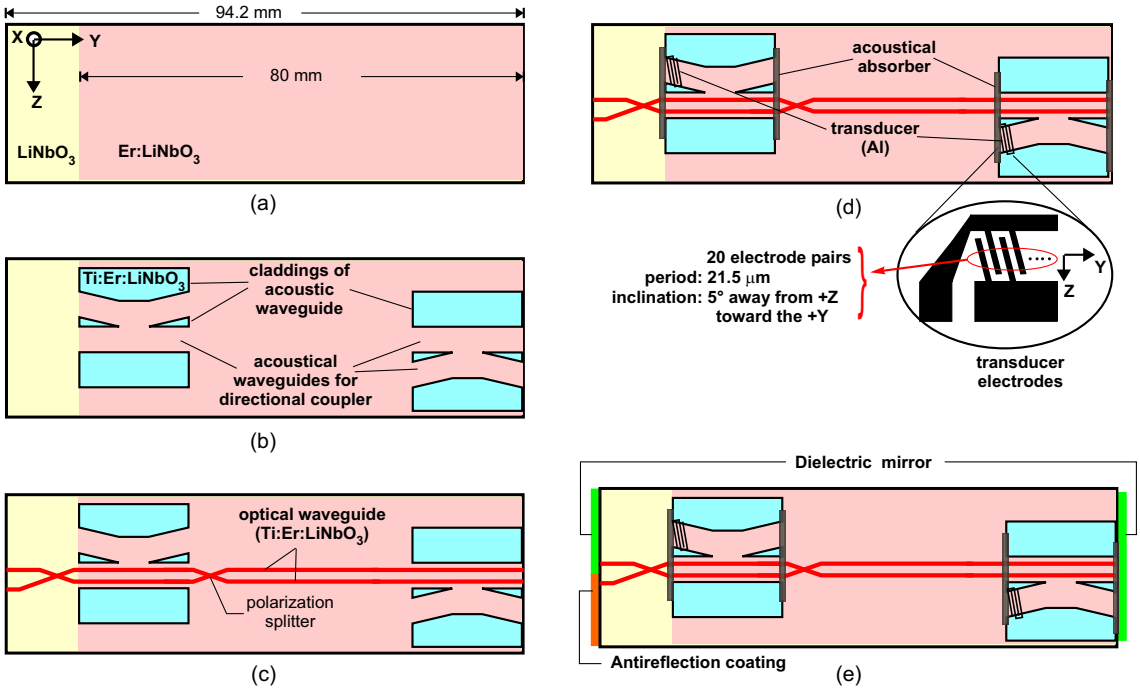

Figure 3.4: Five major fabrication steps for the laser. For better clarity only one laser structure is shown here (not the whole mask region as in figure 3.3): (a) Er-diffusion in $LiNbO_3$, (b) Ti-indiffusion to define the claddings of the acoustical waveguides for AO directional couplers, (c) Ti-indiffusion for optical waveguides and polarization splitters, (d) Al sputtering to form transducers for SAW excitation, and (e) deposition of dielectric layers as antireflection coating and high reflecting mirrors.

of dielectric layers as anti-reflection coating and high reflecting mirrors, respectively, on the waveguide end faces. Before the mirror deposition all the optical and acoustooptical characteristics have been studied to learn the quality of the fabricated structure.

Due to its low diffusivity, Er-diffusion doping is always the first step. To avoid ground state absorption of Erbium, its doping is restricted to pumped sections only. Such a selective doping can be achieved by indiffusion of a patterned, vacuum-deposited Er-layer. First, an aluminium foil is wrapped over the surface of the substrate to protect the area from Er-deposition where Er-doping is not required. A planar 21.1 nm thick metallic Er-layer is deposited on the substrate surface using vacuum evaporation technique. Approximately 80 mm of the 94.2 mm long sample surface is coated by the Er-layer as shown in figure 3.4(a). It is indiffused during 150 hours at 1130 °C, close to the Curie-temperature (approx. 1145 °C) of the ferroelectric $LiNbO_3$. These parameters lead to a nearly Gaussian concentration distribution of $1/e$ depth of 6.2 μm with a corresponding surface concentration of about $2.0 \times 10^{20} cm^{-3}$. The resulting Er concentration profile has a good overlap with the optical mode distribution inside the Ti-indiffused optical waveguides to be fabricated later.

The acoustical directional couplers are fabricated in the next step. A metallic Ti film of 160 nm thickness is evaporated in vacuum all over the surface. The cladding regions of the acoustical waveguides are then defined photolithographically and by

chemical etching. Dimensions of core and claddings of the acoustical waveguides are shown in figure 2.12(a). The Ti-structure (see figure 3.4(b)) is now indiffused at 1060 ℃ during 24 hours. These parameter yield a monomode waveguide with a $LiNbO_3$ core for surface acoustic Raleigh waves. The propagation losses of such an acoustical mode can be as low as 0.5 dB/cm [40].

In the next step, the optical waveguide structure with the two polarization splitters has been fabricated. The dimensions of the waveguides and polarization splitters are shown in figure 2.4(a). A metallic Ti film of 104 nm thickness is evaporated in vacuum all over the substrate surface. Then the optical waveguide structure is defined photolithographically and by chemical etching (as shown in figure 3.4(c)) inside the core of the straight acoustical waveguides. Then 7 μm wide, 104 nm thick Ti-stripes are indiffused at 1060 ℃ during 7.5 hours. This results in a formation of monomode optical channel waveguides for both TE and TM polarization in a broad wavelength region around 1550 nm.

Then the substrate end faces are carefully polished perpendicular to the waveguides. In this phase, optical mode size and propagation loss are studied in the undoped straight optical waveguides for both TE and TM polarized optical waves. To avoid reflections of the optical waves at the waveguide end faces, broad-band antireflection coatings are deposited at both of the substrate end faces. Then the polarization splitting ratio is evaluated for all values of L_c in the waveguide structures in the Er-free region. Then optical absorption and gain is measured in the Er-doped waveguides. Once we find that the waveguides have good optical properties, like, single mode optical waveguiding with low loss (~ 0.1 dB/cm), low polarization splitting ratio (~ -30 dB) and good optical gain (> 0.25 dB/cm) in the wavelength region 1530 nm to 1580 nm, then we proceed to investigate the acoustooptical polarization conversion.

Therefore, next step is to fabricate interdigital transducers to excite a SAW in the acoustic waveguides as shown in figure 3.4(d). A magnified view of the transducer structure with electrode pads is shown as well (see the photograph in figure 3.5). The 500 nm thick interdigital transducers with 20 finger pairs (see section 2.5) are fabricated by aluminium sputtering using the lift-off photolithography technique. An impedance matching circuit allows to excite a SAW with high efficiency. Then the characteristics of acoustooptical polarization conversion is studied to determine the phase matching frequencies and driving power level for optimized conversion efficiency (see figure 2.17).

Finally, broad band anti-reflection and high-reflection coatings are deposited directly on the polished end faces as shown in figure 3.4(e). They are comprised of alternating SiO_2 and TiO_2 layers: for high reflection mirrors, there are 12 alternating layers of quarter wave thickness at wavelength 1560 nm and for antireflection coatings there are 4 alternating layers of optimized thicknesses. O_2-ion beam assisted e-beam evaporation is used to deposit fully oxidized (non absorbing) layers of high density at low substrate temperature. Characteristics of these coatings are described in figure 2.19 in the previous chapter.

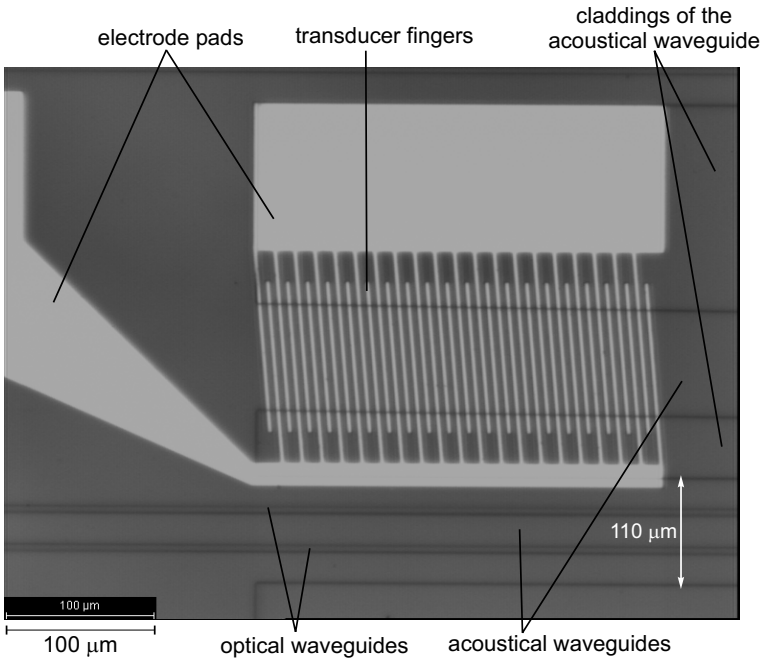

Figure 3.5: Photograph of the Al-transducer on the $LiNbO_3$ substrate. The optical waveguides and acoustical waveguides are visible too.

3.4 Laser Operation

After the discussions of design and fabrication of the laser structure we can follow now the optical field inside the cavity to understand the laser operation and wavelength tuning of its emission. The laser has two polarization splitters. As stated before, those are designed to guide the TM (the TE) polarized optical wave in bar (in cross) state, respectively (see figure 2.4(a)). There are two AO polarization converters inside the cavity. We know that the AO interaction is a phase matched and therefore, wavelength selective process. Depending on the chosen frequency of the SAW, the optical wave

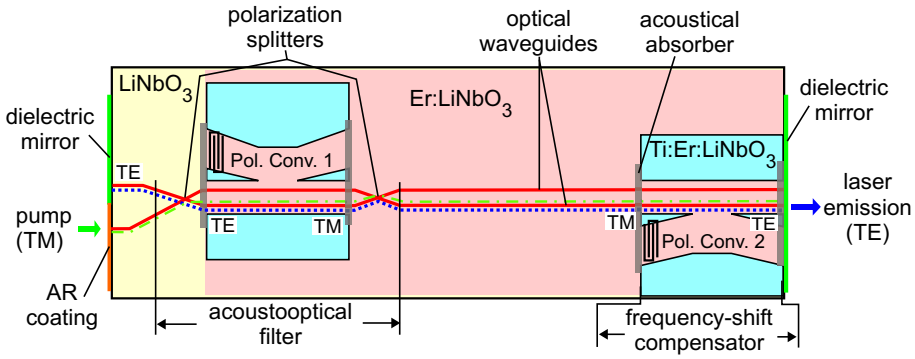

Figure 3.6: Schematic diagram of the acoustooptically tunable Ti:Er:$LiNbO_3$ laser, pumped with TM polarized light. The paths of the pump and intracavity laser field are indicated by the dash-dotted and dotted lines, respectively. The states of polarization (TE, TM) of the intracavity laser field are written in the figure along its path.

at the corresponding wavelength will experience four times a change of the state of polarization during each round trip through the cavity. The guiding channel of the oscillating optical wave will be different inside the filter region for different input polarization to the filter. So to understand all the phenomena of the laser operation, it is better to start with a particular polarization (TE or TM) of the pump light.

Let us consider the case when the laser is pumped with TM polarized light from the lower branch at the left hand side which has a broadband antireflection coating (see figure 3.6, previous page). Since TM-polarized light is guided in the bar states through the polarization splitters, the pump light will be guided along the lower waveguide all through the length of the waveguide as shown by the dash-dotted line. The SAW with its frequency corresponding to a lasing wavelength around 1550 nm will not induce any change of the state of polarization of the pump light at 1480 nm wavelength. So when the laser is pumped in TM polarization the amplified spontaneous emission (ASE) in the wavelength range from 1530 nm to 1620 nm (figure 2.9) is generated in the Er-doped section of the lower waveguide only.

The broadband ASE signal has components in the both states of polarization. The TM component generated at any point between the two polarization converters and travelling along both directions will pass the polarization splitters in the bar state. So it will be guided along the lower waveguide in all sections and as a result it will walk out of the cavity through the antireflection coated end face. But a narrow band signal of this component, whose wavelength is selected by the phase matched frequency of the SAW and whose bandwidth is defined by the AO filter, will experience a polarization conversion due to the AO interaction. The path of this narrowband signal is shown in figure 3.6 by the dotted line. While travelling from right to left through the filter region, it changes its state of polarization from TM to TE and will be guided towards the upper waveguide branch (cross state) and reach the cavity mirror at the left hand end. Since this waveguide section is free from Er-doping, there is no absorption and this signal will be reflected back without much loss.

After reflection by the mirror this TE polarized signal travelling from left to right will be guided back to the lower waveguide inside the filter region. It will experience again a polarization conversion to a TM polarized signal. Now it will be guided in the lower waveguide for the rest of the path to reach the mirror at the right hand end, where it will be reflected back in the same path.

It should be noted that both the polarization converters are driven simultaneously by one RF generator to excite the SAWs with the same frequency. So when the second AO polarization converter has the same phase matched condition, the same optical signal while travelling from left to right will be converted from TM to TE and then will be converted back to TM during travel from right to left from the end face. This polarization conversion is accompanied by a frequency shift by the amount of SAW frequency; it is necessary to compensate the frequency shift induced by the first polarization converter.

The TE polarized component of the broad band ASE generated at any point in the lower waveguide and travelling along both directions will pass through the polarization splitters in cross state. So it will be guided towards the upper waveguide and will be

absorbed in the Er-doped section since there is no pump light in this waveguide.

So while the pump is in the state of TM polarization, a narrowband (wavelength selected by the applied SAW frequency) TM polarized ASE can follow the resonance path through the filter and it is amplified in each round trip. It is to be noted that the filtered and amplified optical wave appears in TE polarization at both mirrors. So a TM polarized pump leads to a TE polarized laser output.

Now the frequency shift of the phase matched optical wave (laser field) is discussed for a round trip path inside the cavity. Let us assume that the frequency of the TE polarized laser field at the left hand end is ν_0 and the corresponding SAW frequency is ν_{ac}. The laser field propagating from left to right (from right to left) is co-directional (contra-directional) with respect to the propagation direction of the SAWs. Then the change in frequency of the laser field associated with the change in state of polarization due to the AO interaction can be followed from table 2.3 and it is shown in figure 3.7. The laser field will experience a frequency upshift to $(\nu_0 + \nu_{ac})$ while crossing the AO filter from left to right. This frequency shift will be compensated while travelling through the second AO polarization converter. Since the state of polarization is changed from TM to TE, it will now experience a downshift in frequency to $(\nu_0 + \nu_{ac}) - \nu_{ac} = \nu_0$. So the laser field starting with frequency ν_0 from the left hand side reaches the mirror at the right hand side with the same frequency ν_0.

During travelling from right to left the laser field now first experiences a downshift in frequency to $(\nu_0 - \nu_{ac})$ inside the second AO polarization converter and then an upshift in frequency to $(\nu_0 - \nu_{ac}) + \nu_{ac} = \nu_0$ inside the AO filter to reach the mirror at the left hand side. So due to the presence of two AO polarization converters/frequency shifters inside the laser cavity, the phase matched oscillating optical field, is reproduced after each round trip to satisfy the resonance condition for a conventional laser operation.

If the frequency of the SAW is varied, the phase matched optical wavelength will also vary correspondingly. That means, another narrowband optical signal from the broadband ASE will be selected by the AO filter to produce the resonant laser emission. Thus an electronically tunable laser operation is possible by simply tuning the frequency of the RF generator driving the SAW.

Since the TE polarized optical wave passes through the polarization splitters in cross state, a TE polarized pump from the lower waveguide branch at the left hand side (AR coated end face) will be guided along the upper waveguide section inside the filter. It will be coupled back to the lower waveguide section by the second polarization splitter (as shown by the dash-dotted line in figure 3.8).

In this case, the TM polarized component of the generated broadband ASE will walk out of the cavity through the AR coated end face or will be absorbed by the Er-doped inactive waveguide sections. Also most of the broadband TE polarized ASE will exit from the cavity through the pump input branch. But a narrowband TE polarized ASE, whose wavelength is selected by the phase matched SAW frequency, will experience a change of its state of polarization from TE to TM and will reach the cavity mirror at the left hand side. All states of polarization of this narrowband optical signal are shown on the figure 3.8. Here the TE polarized pump leads to TM

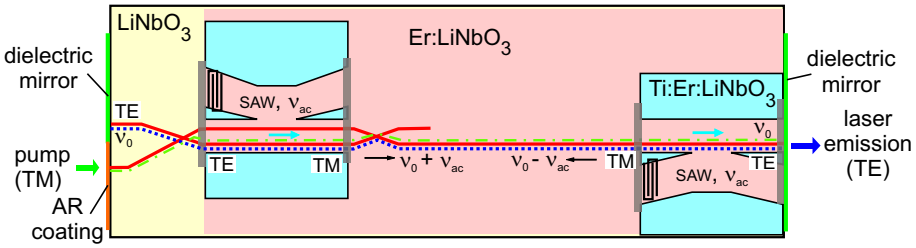

Figure 3.7: The states of polarization and the frequency shifts of the laser field when the laser is pumped with a TM polarized wave. Starting from left: TE, $\nu_0 \rightarrow$ TM, $\nu_0 + \nu_{ac} \rightarrow$ TE, $\nu_0 \rightarrow$ TM, $\nu_0 - \nu_{ac} \rightarrow$ TE, ν_0. In the center region there are two different frequencies of the modes travelling in opposite directions.

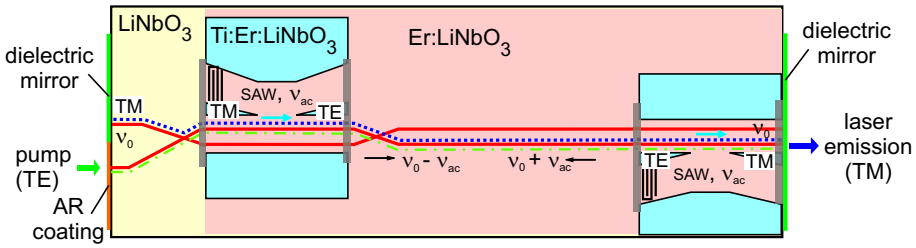

Figure 3.8: The states of polarization and the frequency shifts of the laser field when the laser is pumped with a TE polarized wave. Starting from left: TM, $\nu_0 \rightarrow$ TE, $\nu_0 - \nu_{ac} \rightarrow$ TM, $\nu_0 \rightarrow$ TE, $\nu_0 + \nu_{ac} \rightarrow$ TM, ν_0.

polarized laser output as we have seen above that TM polarized pump leads to TE polarized laser output. Although the amount of frequency shift and its compensation is similar to the case of TM polarized pump, the directions of the frequency shifts are opposite in case of TE polarized pump as shown in figure 3.8. In the round trip path it can be described as (starting from left): TM, $\nu_0 \rightarrow$ TE, $\nu_0 - \nu_{ac} \rightarrow$ TM, $\nu_0 \rightarrow$ TE, $\nu_0 + \nu_{ac} \rightarrow$ TM, ν_0.

We have seen from figure 2.17 that the bandwidth of the AO filter is of the order of 2.5 nm and that of the second AO polarization converter is similar. The conversion efficiency depends on the power of the excited SAW. The required power for 97% conversion efficiency in the developed AO filter is 19.5 dBm (or about 90 mW). It can also be noted from the filter tuning characteristics (see figure 2.18) that a RF frequency of around 170.70 MHz yields a phase matched interaction with an optical mode of a wavelength around 1560 nm; the corresponding tuning slope is –8.2 nm/MHz. When a RF signal of frequency 170.70 MHz with the required level of power is applied simultaneously to both AO polarization converters, a narrowband optical signal at 1560 nm wavelength will be resonant in the cavity. This optical signal will be amplified if the waveguides are optically pumped with sufficient power. Laser emission starts when the amplification overcomes total internal loss of the cavity.

Without any longitudinal mode selective element (like an etalon or coupled external cavity) single mode laser emission is expected as Er:$LiNbO_3$ should be a homogeneously broadened gain medium. In an ideally homogenous laser transition the

atomic lineshape is fixed and identical for all the atoms in the laser medium. The magnitude of the gain and phase shift measured at any given frequency will move up and down as the population inversion ΔN varies, but the lineshapes versus frequency will remain unchanged. In such a laser system under steady state condition of the gain, the laser should oscillate in only one preferred mode, the first mode to reach the threshold; and the gain in the laser medium will be clamped at the level that just causes that mode to reach threshold [124]. Pumping harder will make that preferred mode oscillate more strongly, but will not increase the gain or start new mode to oscillate. In practice, however, homogeneously broadened lasers do indeed oscillate on multiple modes due to the effect known as spatial hole burning (whose details will be discussed in the next section). When oscillation of most central mode creates a standing-wave pattern in the active laser medium, it allows another mode, whose peak fields are located near the energy nulls of the central mode, the opportunity to lase as well. Moreover, in Er:$LiNbO_3$ there could be a stable inhomogeneity in crystal fields due to the structural defects and internal stresses that develop during the course of crystal growth and subsequent technological processing [95, 125]. There are a few data available on the measured values of homogeneous and inhomogeneous line broadening in Er:$LiNbO_3$ [126]. But experimentally, single mode laser emission is already confirmed with measured line width of $\sim$10 pm [42].

Depending on the length of the optical path inside the laser cavity, there is a set of discrete wavelengths (or frequencies) known as longitudinal modes of the cavity for which the total round trip phase shift is an integral multiple of 2π. The frequency difference between two successive longitudinal modes is known as free spectral range of the cavity. The fabricated laser has a geometrical length of 94.2 mm which corresponds to a free spectral range of about 5.7 pm (or 714 MHz in frequency). Now the RF generator which is used to excite the SAW has a minimum frequency step of 100 Hz. Since we know the tuning slope of the acoustooptical filter as –8.2 nm/MHz, a 100 Hz change of the SAW frequency will induce a 0.82 pm change of the central filter wavelength. But all those wavelengths are not resonant in this cavity. In general, by tuning the SAW frequency only, laser emissions at the wavelength steps corresponding to cavity longitudinal modes are expected. For continuous tuning (at any wavelength) of the laser it is necessary to introduce an equivalent change of the cavity length together with the SAW frequency. One way to change the cavity length is by changing the equivalent refractive index of the optical waveguide, but this is not an easy option in this form of design. Another alternative option is to introduce a phase change of the optical wave. This can be achieved by changing the relative phase between the two RF signals of the AO polarization converters. It is mentioned that both AO converters are driven by the RF signals derived from a single RF generator to ensure an exact frequency shift compensation, thereby, to fulfill the necessary condition for the conventional laser operation. At a particular frequency of the SAWs, there is a band of optical wavelengths at the peak of the AO filter pass band which will satisfy all the necessary conditions for lasing except the cavity resonance. Depending on the cavity longitudinal mode, at any time only one wavelength is resonant. Now changing the relative phase between the two RF signals to the AO converters, a phase change will

be induced on the optical waves also. This is equivalent to the change of the optical path length and as a result another wavelength will be resonant in the cavity. It is easy to change the phase between the two RF signals with the help of an electronic phase shifter attached to the electrodes of the frequency shift compensator. Thus changing the relative phase between the two electrodes for the AO polarization converters in a systematic way can help to see the laser at the desired wavelengths or to achieve a continuous tuning of the laser. To observe this tuning it is required to ensure a stable single mode oscillation in the laser by removing all types of mode competition or time dependent variables like spatial hole burning, relaxation oscillations. We will discuss these two remaining issues for such laser to understand its operation and properties. Effective solutions of those problems will also be discussed.

3.4.1 Spatial Hole Burning

When two waves are travelling in opposite directions in a laser medium, interference between these two waves will produce a standing wave pattern of the optical intensity along the length of the cavity. This interference effect gives rise to spatial variations of the population inversion in the laser medium. This effect is known as spatial hole burning effect, which can lead to mode competition or multimode operation even in a homogeneously broadened laser medium [124].

Consider a general situation in which two propagating waves with complex amplitudes $\mathbf{E}_1$ and $\mathbf{E}_2$, frequencies ω_1 and ω_2, and propagation vectors β_1 and β_2 are simultaneously present in a gain medium. The total electric field strength E at any point in the gain medium can be given as

$$\begin{aligned} E(z,t) &= E_1(z,t) + E_2(z,t) \\ &= Re\left[\mathbf{E}_1(z)\exp\left(j(\omega_1 t - \beta_1 z)\right) + \mathbf{E}_2(z)\exp\left(j(\omega_2 t - \beta_2 z)\right)\right] \end{aligned} \tag{3.1}$$

and so the total optical intensity $I(z,t)$, at any point z along the length and at any instant of time t, must then in general be written in the form

$$\begin{aligned} I(z,t) = |E(z,t)|^2 &= |\mathbf{E}_1(z)|^2 + |\mathbf{E}_2(z)|^2 \\ &+ \mathbf{E}_1^*(z)\mathbf{E}_2(z)\exp[j\{(\omega_2-\omega_1)t - (\beta_2-\beta_1)z\}] + c.c. \end{aligned} \tag{3.2}$$

Equation 3.2 shows that the local intensity will contain, in addition to the average intensities $|\mathbf{E_1}|^2$ and $|\mathbf{E_2}|^2$ associated with the two waves separately, an interference term proportional to the dot product of $\mathbf{E}_1^*\mathbf{E}_2$. This interference term contains both a time-variation, at the beat frequency $\omega_{beat} = \omega_2 - \omega_1$ between the two signals and a spatial variation along the length with a spatial periodicity given by $\beta_2 - \beta_1$.

Even if the two optical waves have the same frequency (as in case of laser field oscillation), they will produce spatial modulation of the local optical intensity. Thus, if $\omega_1 = \omega_2$, $|\beta_1| = |\beta_2| = |\beta|$, but, $\beta_1 = -\beta_2$, then the intensity I in equation 3.2 will have a spatial variation of the form

$$I(z) = I_1(z) + I_2(z) + 2\sqrt{I_1 I_2}\cos[2\beta z + \phi] \tag{3.3}$$

where I_1 and I_2 are the intensities of the two waves separately, and the sinusoidal standing-wave portion has a spatial phase angle ϕ related to the relative phases of the two electric fields. If an intensity pattern of this form is present in a homogenously saturable atomic medium, it will presumably produce a spatially varying population inversion of the form [124]

$$\begin{aligned}\frac{\Delta N(z)}{\Delta N_0} &= \frac{1}{1 + I(z)/I_{sat}} \\ &= \frac{1}{1 + \left[I_1 + I_2 + 2\sqrt{I_1 I_2}\,\cos(2\beta\, z)\right]/I_{sat}}\end{aligned} \tag{3.4}$$

where $\Delta N(z)$ is the population difference along the length, ΔN_0 is an unsaturated or small-signal inversion value, and I_{sat} is the saturation intensity or the value of the signal intensity passing through the laser medium that will saturate the gain (or loss) coefficient down to half its small-signal or unsaturated value.

Equation 3.4 describes the spatial hole burning, the spatial variation of gain (or loss) in an atomic medium as shown in figure 3.9. This spatial variation will lead to complex wave-coupling effects in laser. This phenomenon may lead to mode competition between adjacent modes also.

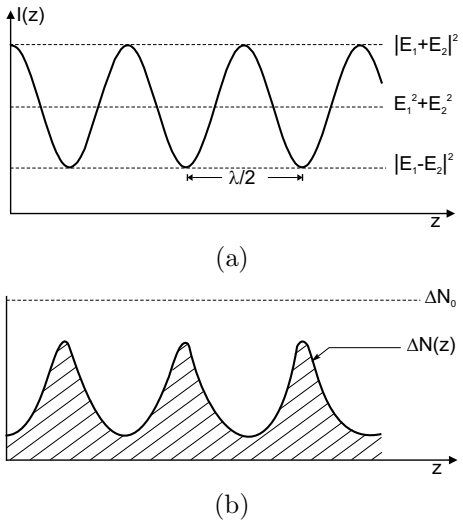

Figure 3.9: (a) Spatial intensity pattern due to interference between two waves having the same optical frequency but travelling from opposite directions. (b) Resulting spatial hole burning or saturation grating pattern of the population difference $\Delta N(z)$. (Ref. [124]).

Suppose a linear or standing-wave laser is initially oscillating in the q-th axial mode. This leads to a standing-wave pattern for the field amplitude or optical intensity along the z-axis, with peaks and nulls spaced by one-half of the optical wavelength (between each null). The inverted population in this laser will then be saturated in a similar spatially periodic fashion as shown in figure 3.10.

As a result, near the center of the cavity, the standing-wave pattern of the (q+1)-th mode–which squeezes one more half optical wavelength into the cavity length–will

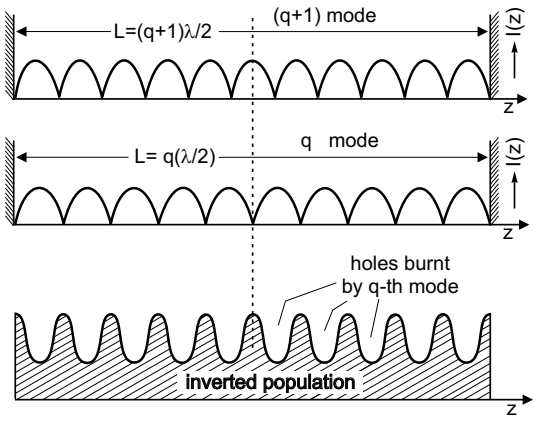

Figure 3.10: Spatial hole burning by the q-th mode of oscillation. (Ref. [124]).

have its maximum intensity located just at the points that left unsaturated by the q-th mode, the same is true equally for (q-1)th axial mode. Consequently, the gain competition between the two adjacent axial modes is much reduced, and both axial modes may well be able to oscillate simultaneously, even within a homogeneous laser medium, by using in essence different groups of atom. Thus two axial adjacent modes will oscillate and bring a saturation uniformity, at least in the center of the cavity. If the saturation in gain is not uniform along the whole length, these two modes cannot achieve equal amplitudes and there will be a competition between them.

There are many ways in which the spatial interference effects between two waves can be washed out. One of those is, if the waves are in fact at different frequencies, then the interference fringes or standing-wave patterns produced by the two waves will move or sweep through the material, because of the temporal part of the interference effect as described in equation 3.2. If the difference in frequency $(\omega_2 - \omega_1)$ between the two waves is large compared to the population recovery time, τ, then the time-varying part of this modulation will be so rapid that the atomic population difference will simply not respond to this frequency, and hence all the terms oscillating sinusoidally in time can be ignored.

Inside the integrated acoustooptical laser cavity there are two acoustooptical polarization converters. They effectively impose individual frequency shifts on the phase matched resonant optical wave. It is seen from figures 3.7 and 3.8 that the oscillating optical waves travelling from opposite directions have two different frequencies in the central section between the two polarization converters. If the wave travelling from left to right has a frequency $\nu_0 + \nu_{ac}$, the wave travelling from right to left has a frequency $\nu_0 - \nu_{ac}$ or vice versa. Thus the frequency difference of these two waves is twice that of the SAW frequency (ν_{ac}), which is here of the order of 170 MHz. This is fast enough compared to the population recovery time, τ in Er:$LiNbO_3$ which is of the order of 2.6 ms. At the same time, the frequency shift imposed by one AO converter is compensated by the second AO converter in each round trip.

3.4.2 Relaxation Oscillations

Some transient behaviors of the laser oscillators and its output are discussed here which are termed as spiking and relaxation oscillations. The term spiking refers to the discrete, sharp, large amplitude pulses that typically occur during the initial turn-on of many lasers and it evolves with decaying amplitude. On the other hand, most of the solid state lasers exhibit relaxation oscillations, which are described as a small-amplitude, quasi-sinusoidal, exponentially damped oscillations around the steady-state amplitude which occur when a continuously operating laser is slightly disturbed. Any small perturbation, such as a sudden change of the pumping rate or of cavity loss, will trigger transient relaxation oscillations. Relaxation oscillations are typical of those lasers in which the recovery time of the excited state population inversion is substantially larger than the laser cavity decay time. Er:$LiNbO_3$ waveguide lasers are characterized by a comparatively long radiation life time (concentration independent fluorescence life time is 2.6 ms) and a short cavity decay time (round trip time divided by total cavity loss factor) of the order of few nanoseconds. A theoretical modelling comparing experimental observations of relaxation oscillations in Er:$LiNbO_3$ waveguide lasers is described in reference [127].

Relaxation oscillations are caused by an interplay between the instantaneous amplitude of the laser field (say signal s), amplitude of the pump (say p), and the population densities (say N_1 for ground state and N_2 for excited state). At the beginning when the signal amplitude is very low, energy from the pump is used to build up the inversion: the population of the ground state decreases and of the excited state, corresponding to the laser level, increases. During this time, the pump amplitude is less than the incident amplitude (due to absorption) and increases exponentially against a position of equilibrium (saturable absorber). After a certain time the inversion will become large enough to slowly increase the amplitude of s due to stimulated emission. The build up of s from its initial value produced by spontaneous emission takes some time; during this time the inversion can continue to grow until the signal amplitude overcomes a specific value. Then inversion decreases with time due to the increased rate of stimulated transitions. After its maximum the signal starts to decrease but as long as it is large enough it further decreases the inversion. As a result the inversion is small enough to be build up by the pumping process again and so on. Thus a increase in the laser field amplitude causes a reduction in the inversion due to increased rate of stimulated transition and consequently this causes a reduction in the gain that tends to decrease the field amplitude which is to be build up by the pump.

The observed relaxation oscillations of this laser is shown in figure 3.11. As shown in the figure 3.11(a) the measured frequency of relaxation oscillation is 164 kHz. Such a low relaxation oscillation frequency allows to develop an optoelectronic feedback loop for the laser stabilization. A scheme for a feed back control loop through a photodiode to the pump source is described in the next section. The transient behavior in the laser output power without and with feedback loop is shown in the figure 3.11(b). Suppression of relaxation oscillations by controlled pumping is possible if spatial hole burning is suppressed sufficiently.

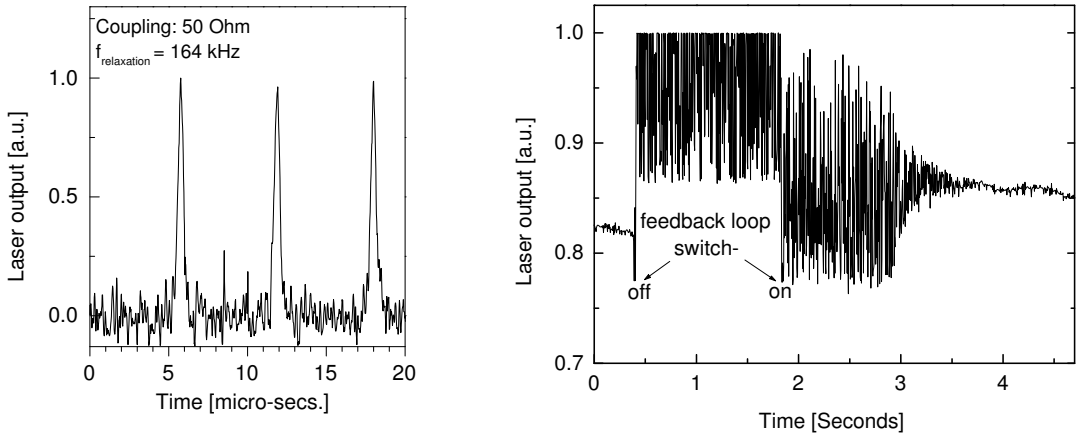

(a) (b)

Figure 3.11: Relaxation oscillations in the laser: (a) Oscillation frequency: $\sim$ 164 kHz (recorded with 50 Ohm load resistance to the photodiode) and (b) Transient behavior of the oscillations when feedback loop is switched off and on.

3.5 Properties of the Laser Output

After the descriptions of design, fabrication and operation principle, the experimental investigation of the laser output is presented. The schematic diagram of the experimental arrangement to operate the laser and to study the laser output characteristics is shown in figure 3.12. Only one laser structure with L_c=330 μm is investigated for the output characteristics. A photograph of the experimental setup with input and output coupling (without external optical and electrical components) and a close view of the pumped optical waveguide with green upconverted light is shown in figure 3.13.

It is discussed in section 2.6 that to achieve a same phase-matched condition for both AO polarization converters of the fabricated laser, it is required to maintain a temperature of 20 °C for the AO filter and of 25 °C for the frequency shift compensator. So for laser operation a temperature difference between the two sections of the laser structure is maintained by arranging two heaters from the bottom with proper thermal isolation. Thermo-electric Peltier elements are used as heating elements; 10 K-Ohm thermistors are used as temperature sensors and two ILX-lightwave temperature controllers are used to maintain these temperatures.

The laser is pumped with a fiber Bragg grating stabilized diode laser at 1480 nm wavelength. A fiber optic isolator was spliced with the fiber of the laser diode behind the Bragg grating. A fiber optic polarization controller is used to select the state of polarization of the pump input. The pump fiber is butt-coupled to the lower waveguide branch at the left hand side (anti-reflection coated end face) of the laser with the aid of a three axes piezoelectric Positioner. The laser output from the lower waveguide at the right hand side is collimated using a free space lens coupling. At a distance of nearly 30 cm the output is coupled to the common branch of a fiber optical WDM to

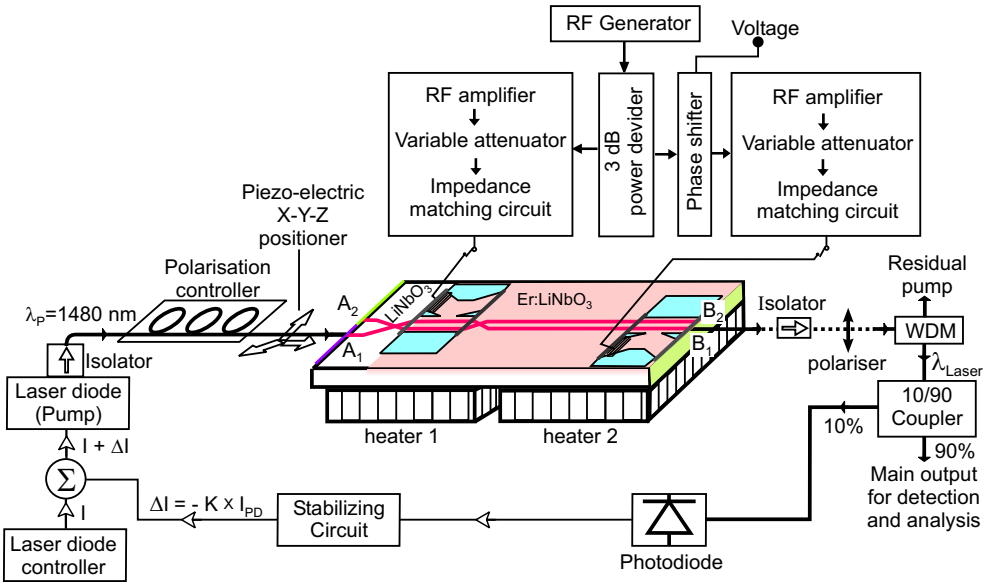

Figure 3.12: Schematic diagram of the experimental setup to investigate the laser. A optoelectronic feedback loop is used to remove the relaxation oscillations. Components are labelled in the figure.

separate the residual pump at 1480 nm from the lasing wavelength around 1550 nm. The states of polarization of pump and laser output are monitored within the free space propagation of the collimated laser output.

The output from the laser wavelength brach of the WDM is divided by a 10/90 coupler. Then the laser output from the 90% branch is used for detection and analysis through a photodiode or an optical spectrum analyzer (OSA).

To suppress the relaxation oscillations of this laser an optoelectronic feedback loop is arranged to control the input pump power. From the 10% branch the laser output is coupled to a fiber pigtailed, biased, InGaAs-PIN photodiode and the corresponding electrical signal is fed to a specially designed stabilizing circuit. The stabilizing circuit eliminates the DC part of the photodiode signal and amplifies the AC components. A current is generated which is inversely proportional to the AC components. The gain of this photodiode signal is continuously variable within almost 2 orders of magnitude. This is important to adjust the optimum point of operation for the stabilization. The bandwidth of the amplifier is above the resonance frequency of the relaxation oscillation. The output current of the stabilization circuit is directly superimposed to the current of the pump laser diode to avoid any limit in frequency modulation of the laser diode controller. As shown in the figure 3.11(b) the relaxation oscillation is thus suppressed successfully.

Only one RF generator is used to excite SAWs of the same frequency for both the polarization converters. Since the required power levels for maximum conversion of the polarization are different for both converters, individual RF amplifiers, attenuators and impedance matching circuits are used behind a 3 dB power divider as shown in the figure. A voltage controlled phase shifter is used to change the relative phase of the two SAWs.

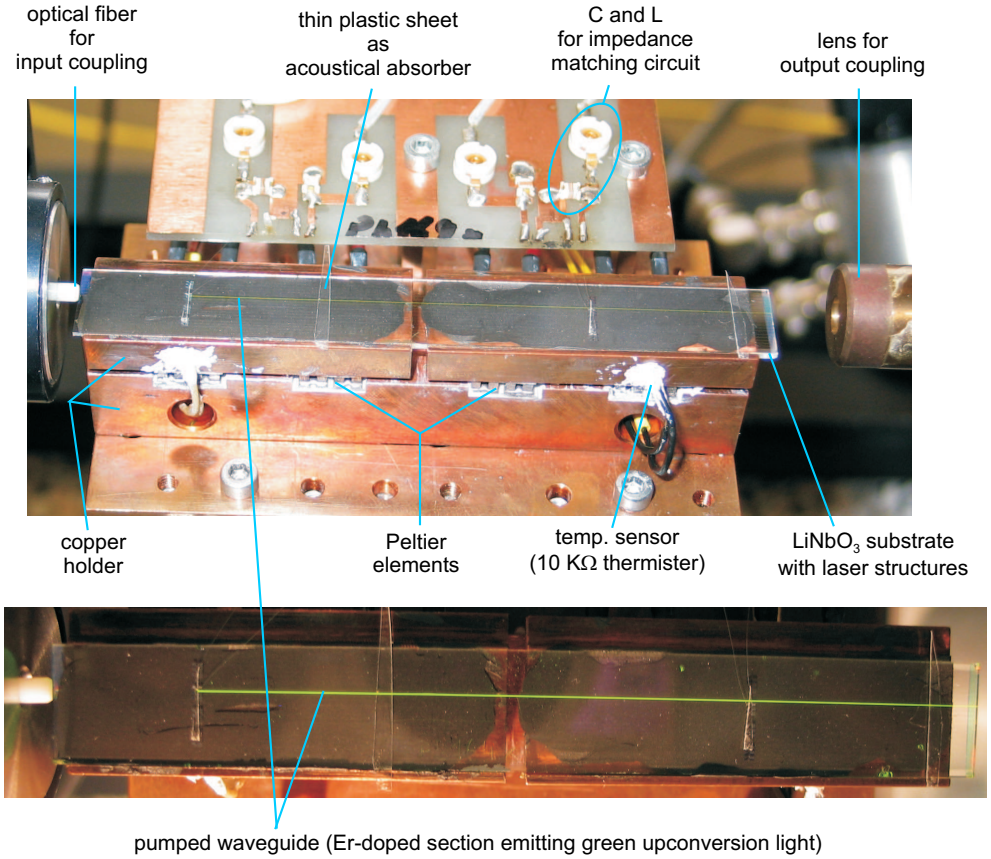

Figure 3.13: Photograph of the experimental setup with input output coupling (without external optical and electrical components). The laser sample is mounted on a copper holder to control the temperatures in two sections. Lower part is the close view of the pumped waveguide emitting green upconversion light.

The laser can be operated via the pump polarization in both TE and (or) TM using the same input/output configuration of the cavity. However, as there is a considerable photorefractive effect if a high power (of the order of 100 mW) pump is launched in TE polarization, the laser performance is studied mainly with TM polarized pump input and, consequently, the state of polarization of the laser output was TE. The laser output characteristics are discussed in the following sections.

3.5.1 Power Characteristics

From the gain characteristics in TM polarization (shown in figure 2.9), it is observed that there are peaks of the gain at wavelengths about 1531, 1545, 1561 and 1568 nm. Therefore, we studied the power characteristics of the laser output at these wavelengths. The corresponding SAW frequency to select these wavelengths are 174.28, 172.55, 170.57, 169.7 MHz, respectively. These SAW frequencies corresponding to the wavelengths are sensitive to the operating condition of the laser, particularly with the temperature variation. A slight change in temperature difference between the two

AO polarization converters may cause a shift of the the laser emission wavelength. Even the increase of pump power causes an increase of temperature of the waveguide locally resulting in a shift of the the laser emission wavelength by the order of tens of pm. This shift of the wavelength could be readjusted by changing the differential temperature, or by adjusting the SAW frequency. But during the measurement of the power characteristics (laser output power versus input pump power), this small shift is neglected. Actually it is difficult to readjust the wavelength shift while the pump power is changed smoothly by changing the injection current of the pump laser diode by applying a modulation voltage from a ramp generator. The power characteristics of the laser at those four different wavelengths are shown in figure 3.14(a) and the corresponding summary of the characteristics is mentioned in the table 3.1.

The power characteristics is obtained as the function of incident pump power measured at the end face of the fiber just before the sample. The coupled pump power can be estimated if we consider the coupling loss due to alignment and mode overlap between fiber and waveguide as 10% and residual reflection of 8% on the dielectric antireflection coating. The output power is measured behind the WDM and 90% branch of the 10/90 coupler with a fiber coupled optical power meter. For the 1568 nm wavelength, the threshold power is 31.2 mW and at 110 mW coupled pump power, the output is 0.6 mW; the slope efficiency is about 0.7%. It indicates that further optimizations are required for better output coupling.

The stability of the output power is checked by recording the time varying fluctuations as shown in figure 3.14(b). A fraction of the total output power of the laser (when $\lambda = 1560\,\text{nm}$ and the incident pump power is about 80 mW) is fed to a photodiode and photodiode output is recorded by an digital oscilloscope. A record over a time of 20 seconds (with 50 samples/sec) shows that there is nearly $\pm 6\,\%$ fluctuation in the power. This study is performed when relaxation oscillation is suppressed by a feedback control loop. External causes like vibration in the setup, surrounding airflow, spurious reflections at the output coupler have influences for this instability. So a certain reduction of this fluctuation is expected in a packaged and fiber pigtailed (in both ports) laser.

Table 3.1: summary of power characteristics

Output wavelengths [nm]	1531	1545	1561	1568
SAW frequency [MHz]	174.28	172.55	170.57	169.7
Threshold power [mW] (incident)	65	52	40	38
Laser output at 130 mW incident pump power [mW]	0.28	0.43	0.55	0.57
Slope efficiency [%]	0.3	0.5	0.6	0.6

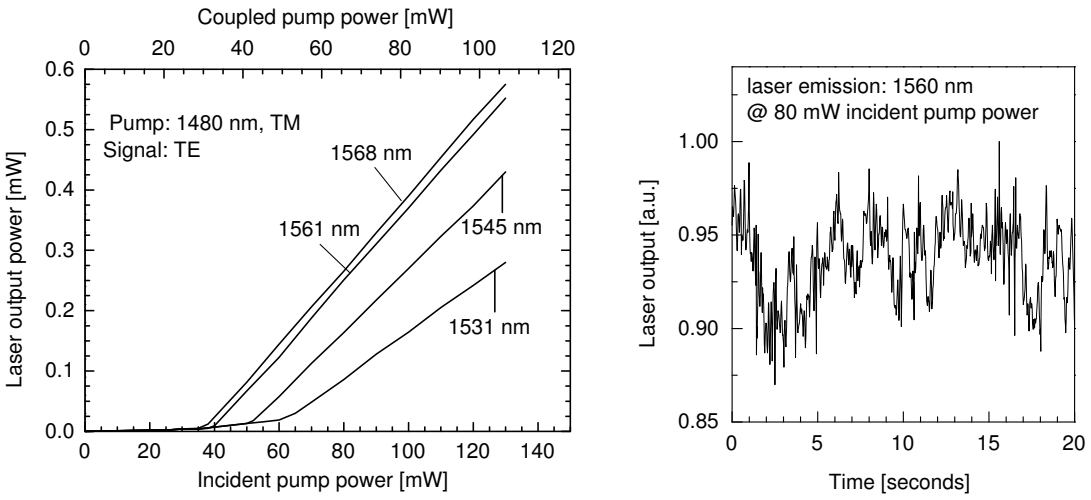

(a) (b)

Figure 3.14: Laser power characteristics: (a) output power versus pump power in single mode emission, and (b) output power versus time; photodiode load resistance: 50 Ohm.

3.5.2 Tuning Characteristics

The laser output wavelength is tuned electronically by tuning the SAW frequency of the AO filter and frequency-shift-compensator driven by a RF signal generator. A very wide tuning range is observed with this integrated Er:$LiNbO_3$ laser.

The tuning characteristics of the laser emission wavelength is shown in figure 3.15. It is observed that it is possible to tune the output wavelength of the laser from 1530 nm to 1577 nm. For the first time, a 47 nm wide tuning range is observed in an acoustooptically tunable integrated Ti:Er:$LiNbO_3$ laser. This tuning range is not limited by the bandwidth of the acoustical transducers, but depends on the available optical gain at the selected resonant wavelength inside the cavity. Since the gain bandwidth of the Er:$LiNbO_3$ amplifier extends from 1530 nm to 1620 nm wavelength, the maximum range can be expected in this region when the laser structure is pumped appropriately. The total internal loss of the cavity (waveguide propagation loss, losses in the polarization splitters, loss due to polarization conversion) is about more than 3 dB, somewhat higher than the total maximum gain available at longer wavelengths. So no laser emission is obtained at longer wavelengths (> 1577 nm).

Figure 3.15(a) shows the spectral output of the laser at different optical wavelengths at constant input pump power (130 mW, TM) and the corresponding operating SAW frequencies are plotted in the upper scale. The optical spectra are recorded using an optical spectrum analyzer with a spectral resolution bandwidth of 10 pm and a span of 500 pm. The spectral dependence of the peak power of the laser follows approximately the gain curve except in the region at 1531 nm, where the observed peak spectral power is low compared to the region at 1538 nm. The spectra around 1531 nm were broadened comparatively like a multimode emission, so the total power under the spectral envelop was higher at 1531 nm compared to 1538 nm. A much higher coupled pump

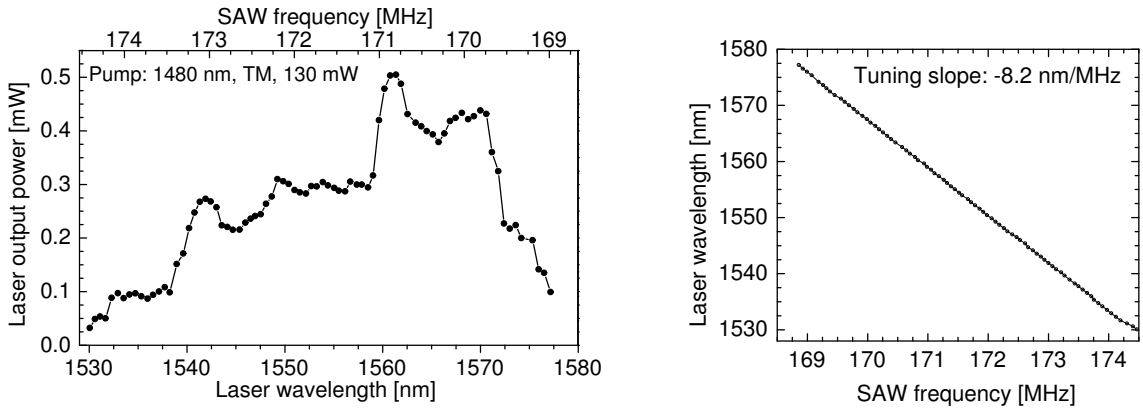

Figure 3.15: Tuning characteristics of the laser. (a) Laser output power versus laser emission wavelength (reading from an optical spectrum analyzer) while the corresponding SAW frequencies are shown in the scale above. The measured data are shown by the black dots. (b) Laser emission wavelength versus SAW frequency; the same data as in (a) plotted to show the tuning slope.

power is required to get a higher emission at 1531 nm which is not possible with the pump laser diode we have used. The applied RF frequency and the corresponding central wavelength (peak spectral wavelength) of the laser emission are recorded manually while appropriate laser operating conditions (input pump coupling, optimum power of the SAW, temperature) have been maintained maintained for optimized and stable emission. The results are plotted in figure 3.15(b). It is clear from this plot that the tuning slope of the laser is –8.2 nm/MHz which corresponds to the observed tuning slope of the acoustooptical filter.

In the frequency range of 170 MHz, the RF function generator (Marconi Instruments, 2022c) has minimum frequency steps of 100 Hz. If the appropriate operating condition of the laser is maintained, the 100 Hz change of the SAW frequency results in a 0.82 pm change of the wavelength of the laser output. So an optical spectrum analyzer with 10 pm resolution would show a continuous change in wavelength if the change in SAW frequency steps is 100 Hz. But it is observed that the tuning is not continuous. The laser cavity of geometrical length of 94.2 mm has a corresponding longitudinal mode spacing of 5.7 pm. So it is expected that the laser cannot be tuned in finer steps unless the cavity length is adjusted to be resonant for those wavelengths.

Since the laser is driven by two RF signals (derived from a single RF generator) for two AO polarization converters (for filter and frequency shift compensator), it is expected that the relative phase change between these two SAWs will introduce a change of the effective optical path length inside the cavity due to a induced change of the phase of the optical wave. A voltage controlled phase shifter has been connected to the second AO polarization converter as shown in figure 3.12. The shift of the lasing wavelength is observed indeed by changing the relative phase between the two SAWs of

this laser. It indicates the possibility that by changing the relative phase between two SAWs together with the frequencies in an appropriate manner, a continuous mode-hop free tuning should be possible. Systematic recording of this tuning is not possible at this moment mainly because of random jumps between the longitudinal modes with time and also often it is multimode. There are external disturbances in the setup like input coupling instability, vibrations, reflections at the output coupling lens and fiber, there are also internal causes like spatial hole burning which influence the laser oscillations and stability in single mode operation. A substantial improvement is expected when the laser will be packaged properly with fiber pigtails.

The oscillating laser signal in the section of the waveguide between the two AO polarization converters has the two different frequency $\nu_0 + \nu_{ac}$ and $\nu_0 - \nu_{ac}$ (see figure 3.7). So there is no standing wave pattern in this central section. Sections of the waveguides inside the polarization converters are doped with Er and contribute to the effective gain inside the cavity. At the rear ends of both AO polarization converters, there is an overlap of waves of the same frequency ν_0 from both directions, which causes spatial hole burning effects resulting a permanent source of mode competition. So it is necessary to have the AO polarization converters outside the Erbium doped waveguide section to avoid this spatial whole burning. This design is considered for next investigation of a new laser sample.

3.5.3 Spectral Characteristics

The spectral characteristics of this laser emission is studied using an optical spectrum analyzer (OSA) with the maximum resolution of 10 pm. The operating temperature, the driving SAW frequency and other conditions are maintained carefully for laser emission at about 1562 nm wavelength. As recorded by the optical spectrum analyzer a typical spectrum is shown in figure 3.16(a) (peak spectral power is normalized to one). As expected, we observe a single mode emission from this laser. The measured spectral linewidth (at FWHM) is 12 pm. As shown in the figure, the clear and smooth spectral envelop certainly indicates a stable output. Since the measured (with the OSA) linewidth is near to the resolution limit of the instrument, we may assume that the true linewidth is smaller corresponding to single mode operation.

The laser emission is also investigated by a scanning Fabry-Perot spectrum analyzer (with 15 GHz free spectral range) to see if the laser is truly single mode. Indeed, it shows a single mode emission as shown in figure 3.16(b). But at this moment there are jumps between the modes. This is due to the technical noises arise mainly from the experimental setup. Though there is a fairly stable single mode emission at wavelength longer than 1540 nm, it is never stable in the range around 1531 nm wavelength. The exact cause is not yet clear to us.

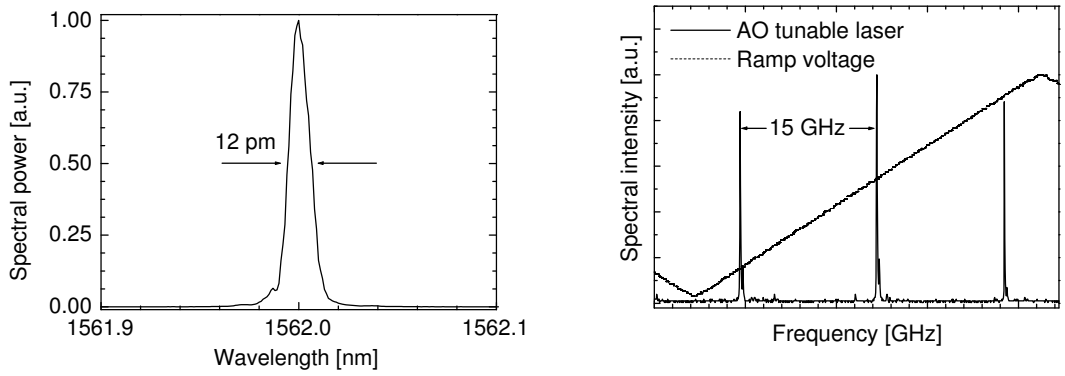

(a) (b)

Figure 3.16: Spectral characteristics of the laser: (a) spectrum of the laser output observed through optical spectrum analyzer with resolution bandwidth 10 pm. Measured linewidth at FWHM is 12 pm. (b) Laser emission spectrum from a scanning Fabry-Perot spectrum analyzer of 15 GHz free spectral range.

3.6 Conclusions

Design, fabrication, operation and output characteristics of an integrated acoustooptically tunable Ti:Er:$LiNbO_3$ laser are presented in this chapter. In this mode of operation, it is termed as conventional frequency shift compensated (FSC) laser since most of the lasers work in this principle of operation. Another mode of operation termed as frequency shifted feedback and the corresponding output characteristics of the same laser structure will be presented in the next chapter.

Single mode laser emission is achieved with a 47 nm (1530 nm $< \lambda <$ 1577 nm) wide tuning range. The tuning slope is –8.2 nm/MHz. Single mode laser emission is confirmed by analyzing through a scanning Fabry-Perot spectrum analyzer. The measured line width of the laser is 12 pm while the spectral resolution of the optical spectrum analyzer is 10 pm. So the true linewidth is narrower. A maximum output power is measured to be 0.5 mW at 1560 nm wavelength for 105 mW coupled pump power. A higher output power is expected if the reflectivity of the output mirror is optimized. At present the laser output properties are investigated in a normal laboratory environment causing a nearly ±6 % fluctuations. Relaxation oscillations are removed using a feedback control loop for the pump power.

The design is considered to minimize the total internal loss and to have a maximum length of the Er-doped section to achieve a high gain. But it leads to a mode competition due to a spatial hole burning effect inside the AO polarization converters. So a new design is to be considered to keep the AO polarization converters outside the gain section.

Chapter 4

Frequency Shifted Feedback (FSF) Laser

4.1 Introduction

In the previous chapter an integrated acoustooptically tunable FSC laser and its output characteristics is described. The frequency shifting of the optical wave by the AO tunable filter and its compensation by another AO polarization converter (named as frequency shift compensator) is essential to fulfill the condition of conventional laser operation forming the resonant modes like in a Fabry-Perot cavity. Now we will investigate the output from the same cavity but turning off the frequency shift compensator. In such a case (as explained in figure 2.10 in chapter 2), the optical wave will be frequency shifted in each round trip. An optical wave of frequency ν_0 is shifted to $\nu_0 - 2\nu_{ac}$ after a round trip through the AO filter, where ν_{ac} is the frequency of the corresponding acoustic wave. Thus, the continuous change in frequency disturbs the feedback conditions to build up the discrete modes of fixed resonant frequencies, i.e., the frequency shifted feedback changes the emission characteristics considerably from that of a conventional FSC laser. The immediate question is if there will be any useful emission from such cavity. The answer is positive. The investigation of such output with unusual frequency properties started in 1970s for acoustooptically tunable dye lasers [128, 129]. Such lasers are described as frequency shifted feedback (FSF) lasers [46]. Initially, a modeless laser emission has been assumed [48–50] but further investigations reveal the emission of chirped modes [62, 67].

An integrated tunable FSF laser in Erbium doped Lithium Niobate is described for the first time. Experimental studies of the properties of the laser output are also presented here with investigation using an optical spectrum analyzer and by heterodyne experiments. The basic elements for this AO tunable FSF laser, like Er-doped optical waveguide amplifier, waveguide polarization splitter, AO polarization converter, dielectric coatings for high-reflection and antireflection are described in chapter 2. Since the same integrated AO tunable FSC laser can be operated as AO tunable FSF laser by simply switching off the frequency shift compensator, the characteristics of the

basic components and the fabrication steps for the FSF laser can be followed from chapter 2 and chapter 3, respectively. An interesting application of this FSF laser for frequency domain ranging is presented in the following chapter.

4.2 Laser Operation

A schematic diagram of the integrated acoustooptically tunable waveguide FSF laser is shown in figure 4.1. There is a Ti-indiffused channel waveguide structure in the Er diffusion-doped surface of a 94.2 mm long X-cut (Y-propagating) $LiNbO_3$ substrate. If optically pumped by an external laser diode (λ=1480 nm) of suitable pump power an intracavity optical amplification can be obtained in the wavelength range 1530–1620 nm (see figure 2.9).

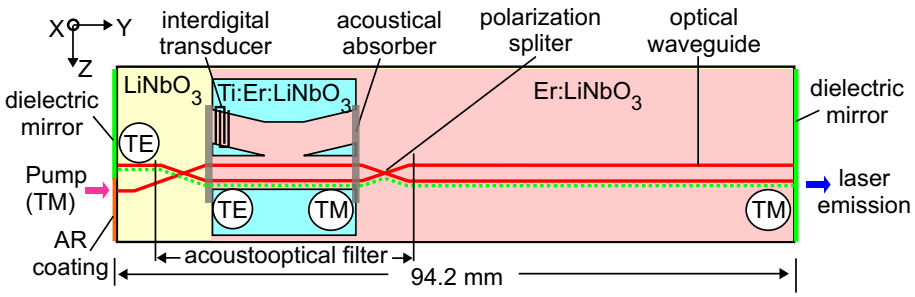

Figure 4.1: Schematic diagram of the acoustooptically tunable frequency shifted feedback Ti:Er:$LiNbO_3$ laser. The acoustooptical filter serves as polarization converter and frequency shifter simultaneously. The waveguide path of the intracavity laser field is indicated by the dotted line when the laser is pumped with a TM polarized wave. The corresponding states of polarization of the internal laser field are shown inside the circles. X, Y, Z (≡ optical c-axis) are the crystal axes.

There is an integrated AO filter inside the cavity which is the key element of this laser. As described before, the AO filter consists of two polarization splitters and an AO polarization converter with a tapered acoustical directional coupler in between. It serves two purposes in this laser. It acts as an optical wavelength selective element for tuning its emission wavelength and also as a frequency shifter. The selected optical wave experiences a frequency shift by the amount of the frequency of the surface acoustic wave (SAW) in each pass through the filter.

The SAW is excited in the tapered acoustical waveguide of the acoustical directional coupler via the interdigital transducer driven by a RF generator. It will interact with the guided optical mode in the optical waveguides embedded in the core of the straight acoustic waveguide. Since the AO interaction is a phase-matched (wavelength selective) process, depending upon the frequency of the SAW, a narrow band optical wave of selected wavelength from the broadband amplified spontaneous emission (ASE) will be converted to the orthogonal polarization and will experience a frequency shift by the amount of the SAW frequency. This selected and polarization converted optical wave is separated from the rest of the unconverted ASE through the waveguide polarization splitters. Thus a narrow-band wavelength filtering ($\Delta\lambda_{FWHM} \approx 2.4$ nm, see

figure 2.17(a)) is achieved.

The polarization splitters are designed to route TM-polarized light to the bar-state and TE-polarized light to the cross-state. Thus wavelength filtering is achieved between the upper left channel and the lower right intracavity guide. The internal laser field follows the path marked by the dotted line, if the laser structure is pumped via the lower left guide in TM-polarization. As a consequence the state of polarization (SOP) of the internal laser field is TE on the left and TM on the right side. Alternatively, a TE-polarized pump selects the upper channel inside the filter structure and therefore leads to a TE-polarized laser output on the right side with orthogonal SOPs internally in comparison with those indicated in figure 4.1.

A frequency upshift is obtained for a codirectional (contradirectional) acoustooptical polarization conversion with a TE-polarized (TM-polarized) input field (see table 2.3); this corresponds to the mode of operation as indicated in figure 4.1. During each round trip the laser field undergoes two polarization conversions with two frequency shifts in the same direction. The spectral width of the filter for net intracavity gain determines the effective number of round-trips and, therefore, the spectral width of the laser emission. On the other hand, a frequency downshift occurs if the device is pumped in TE-polarization and the orthogonal SOPs are observed internally. Contrary to a conventional laser, the internal laser field is not reproduced in amplitude and phase after each round-trip. The frequency shifted feedback broadens the spectral width of the laser emission and suppresses the formation of resonant longitudinal cavity modes.

The laser cavity is formed by two dielectric multilayer mirrors deposited on the waveguide end faces. Only the end face of the lower arm of the left polarization splitter is anti-reflection coated which facilitates efficient pump power coupling from a fiber-coupled laser diode. Also the rest of the optical waves generated from ASE whose wavelengths are not phase-matched with the SAW frequency walk out of the cavity through this AR-coated end face.

4.3 Analysis of a FSF Laser Cavity

Within the pass band of the AO filter (of the order of 2.5 nm) there are hundreds of cavity resonances in absence of the FSF. Then one can consider the effect of FSF on these cavity resonances. In the FSF cavity each is continuously swept in frequency after each pass through the filter and increased in amplitude by the gain of the optically pumped Er:$LiNbO_3$ amplifier. When the gain is more than unity, the modes will build up from the noise level to the appreciable level in several round trips before they are running out of the filter pass band frequency. Thus, for a consecutive upshift of the frequency, the output spectrum will shift towards the high frequency end of the filter, resulting in a line narrowing. For a downward shift of the frequency this happens towards the low frequency end of the filter. Therefore, a comb of frequencies separated by the cavity FSR exists in the output of the FSF laser. For a steady-state solution for the continuous chirped modes a quantitative model is presented by

Nakamura et. al. [62] which is discussed below.

A frequency shifted feedback cavity can be analyzed by using a self-consistent equation of the intracavity field. We can consider an ideal cavity model for simplicity, i.e., a Fabry-Perot type resonator containing a modulator as shown in figure 4.2. A reference plane is considered for analysis as shown by the dashed line in the figure.

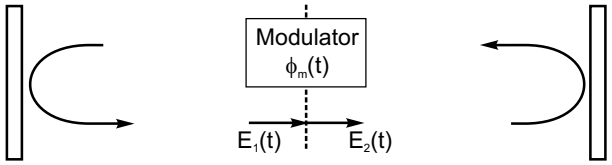

Figure 4.2: An simplified analytical model for the FSF laser: the cavity contains a modulator. The reference plane of the intracavity field is given by a dashed line.

The time dependent intracavity field on the reference plane can be expressed as

$$E(t) = E_0 \exp\left[j2\pi\phi(t)\right] \tag{4.1}$$

$$\text{with,} \quad \phi(t) = \nu_0\, t + \phi_c(t) \tag{4.2}$$

where ν_0 is the frequency at which the seeding electric fields are repeatedly generated, and $\phi_c(t)$ is a temporal variation of the phase caused by the modulation. In this FSF laser the intracavity modulator is an AO polarization converter and the change of the optical field through the modulator can be expressed as

$$E_2(t) = E_1(t) \exp\left[j\phi_m(t)\right] \tag{4.3}$$

$$\text{with,} \quad \phi_m(t) = \nu_{ac}\, t \tag{4.4}$$

where $E_1(t)$ and $E_2(t)$ are input (incident) and output (diffracted) fields, respectively, and ν_{ac} is the driving frequency of the AO polarization mode converter. For a continuous wave (cw) oscillation, the intracavity field should be a replica of itself after one round trip. That is, it should satisfy the self-consistency condition. At this point, we allow the laser to sustain several phase variations separated by a time delay ΔT. Under this condition, $\phi(t)$ is required to satisfy the following relation [62]

$$\phi(t - q\Delta T) = \phi(t - q\Delta T - \tau_{RT}) + \phi_m(t) + \phi_m(t - \tau_{RT}) \tag{4.5}$$

where q is an integer which represents the longitudinal mode number, time interval $\Delta T = 1/\nu_{FS},\ \nu_{FS} = 2\nu_{ac}$ is the round trip frequency shift of the oscillating laser field in the cavity, and τ_{RT} is the round trip time in the cavity.

A solution of this difference equation can be written as

$$\begin{aligned} \phi_q(t) &= \phi(t - q\Delta T) \\ &= \left(t - \frac{q}{\nu_{FS}}\right)\nu_0 + \left(t - \frac{q}{\nu_{FS}}\right)^2 \frac{\nu_{FS}}{2\tau_{RT}} + \Phi_q \end{aligned} \tag{4.6}$$

where Φ_q is an initial phase. An instantaneous frequency $\nu_q(t)$ of the field is given by a differentiation of equation 4.6 which is given by,

$$\nu_q(t) = \frac{d}{dt}\phi_q(t) = \nu_0 - \frac{q}{\tau_{RT}} + \frac{\nu_{FS}}{\tau_{RT}}t \tag{4.7}$$

The equation 4.7 shows that the frequency shifted feedback cavity is potentially able to sustain continuously chirped frequency components. The chirp rate of each component equals to the frequency shift per round trip time: $\gamma = \nu_{FS}/\tau_{RT}$, and they are spaced by the cavity mode separation: $1/\tau_{RT}$. To derive the solution 4.6, it was assumed that $\phi_c(t)$ always exists or is varying even before the AO converter is turned on. This assumption is physically justified by a dephasing effect of a lasing medium, since the dephasing effect is regarded as a random and rapid phase modulation of an atomic transition frequency. In other words, a random phase modulation in the lasing medium is a seed of the oscillation in the frequency shifted feedback cavity. The chirped frequency components are estimated to be strongly correlated in phase and later it is experimentally proved [67].

On the basis of this analysis, a model on the spectral properties of the FSF laser emission is proposed and verified by different experimental observations. This model is developed for a bulk optics all solid-state diode pumped Nd:YVO_4 FSF laser [64,65]. The graphical presentation of this model is shown in figure 4.3. It also explains the experimental observations related to this integrated FSF laser emission.

Figure 4.3(a) shows the instantaneous frequency of the FSF laser emission versus time. The grey scale schematically represent the amplitude change of each instantaneous frequency component. Figure 4.3(b) illustrates the spectral properties of the FSF laser. ν_c is the center frequency of the filter function. ν_0 is the frequency at which the seeding electric fields are generated, and ν_m is the instantaneous oscillation frequency at peak-spectral intensity. In the proposed model, the seed of the electric field is assumed to be generated always at the frequency ν_0 near ν_c and is regeneratively amplified by the phase shift according to each round trip in the cavity. The evolution of single component (or of all components) after generation can be followed in the same way. The seeding electric fields are repeatedly generated at intervals of $1/\nu_{FS}$. The instantaneous spectrum consists of a continuously chirped comb of frequency components with a regular spacing equal to the longitudinal cavity mode $1/\tau_{RT}$. Since during each round trip time τ_{RT}, the frequency shift of the oscillating laser field is ν_{FS}, the chirp rate (frequency shift per second) is given by ν_{FS}/τ_{RT}. Instantaneous spectral intensity is shown in the middle trace of figure 4.3(b). There are number of frequency components with different intensity level with a frequency spacing $1/\tau_{RT}$. Intensity of the component of the comb increases due to regenerative amplification along with the frequency shift after the creation and then decreases due to gain reduction as shown in the upper trace of the figure 4.3(b), in which the AO filter bandwidth is given as $\Delta\nu_a$ (FWHM) and is centered at ν_c. The instantaneous oscillation frequency at peak spectral intensity ν_m is detuned from the central frequency ν_c. In effective, the gain curve will be modified by the filter function of the AO filter. The lower trace of the

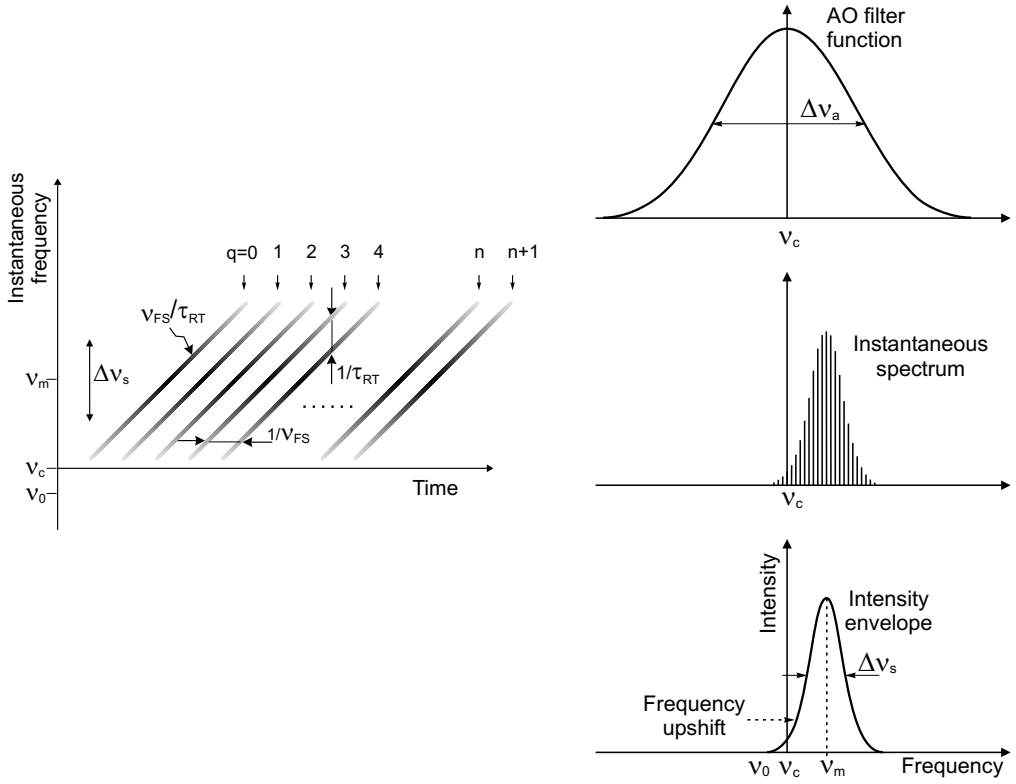

Figure 4.3: A model for the spectral properties of the FSF laser emission. (a) Instantaneous frequency versus time; q is an integer indicating the components of the comb. The frequency components are generated repeatedly at intervals $1/\nu_{FS}$, (ν_{FS}: the round trip frequency shift). The separation between adjacent components is $1/\tau_{RT}$, the free spectral range of the laser cavity. The chirp rate of each component: ν_{FS}/τ_{RT}, the rate of frequency shift. (b) Instantaneous spectrum and intensity envelope of the FSF laser emission; ν_c and $\Delta\nu_a$ are the center frequency and spectral linewidth of the AO filter, ν_0 is the seed frequency at which each component are generated repeatedly, ν_m is the instantaneous frequency of a component at the peak spectral intensity, and $\Delta\nu_s$ is the spectral linewidth of the FSF laser emission.

figure 4.3(b) shows the envelope of the spectral intensity with a peak at the frequency ν_m; it has the oscillation bandwidth $\Delta\nu_s$.

Experimental observations, which will be shown later and numerical simulation [62, 65] show that the spectral envelop of the FSF laser output has a nearly Gaussian profile with slight asymmetric but for simplicity it can be assumed to be a Gaussian profile. Then the amplitude variation $E_q(t)$ of each instantaneous frequency component is given by:

$$E_q(t) \propto \exp\left[-\left\{\frac{\gamma(t-q\Delta T)}{(\Delta\nu_s/2)}\right\}^2\right] \tag{4.8}$$

where $\gamma = \nu_{FS}/\tau_{RT}$ is the frequency chirp rate and $\Delta\nu_s$ is the oscillation bandwidth.

Then the total output of the FSF laser can be expressed as:

$$I(t) = \left| \sum_q E_q(t) \exp\{j2\pi\phi_q(t)\} \right|^2 \tag{4.9}$$

Considering the Fabry-Perot cavity configuration for the FSF laser, the corresponding complex electric field of its output can be expressed as the summation of frequency component with the phase shift $\phi_q(t)$ and can be written as [65]:

$$\varepsilon(t) = \sum_q E_q \left\{ \sqrt{R}\, \eta_{ac} G(\nu) \right\}^{(\nu-\nu_0)/\nu_{FS}} \times \exp\{j\phi_q(t)\}, \qquad |t| \leq \frac{T_0}{2} \tag{4.10}$$

where $T_0 = \Delta\nu_a(\tau_{RT}/\nu_{FS})$ is the time duration of the qth electric field of comb between its creation and annihilation, E_q is the amplitude of the qth electric field of comb, and ν, $G(\nu)$, R, η_{ac} are the instantaneous frequency, the power gain per single pass, the reflectance of the output coupler and the conversion efficiency of the AO polarization converter, respectively. The expression $(\nu - \nu_0)/\nu_{FS}$ indicates the number of round-trip. The temporal variation of the phase $\phi_q(t)$ can be given by the equation 4.6.

This model and the equation 4.6 can be used to show how the FSF laser output and its spectral characteristics depend on the cavity parameters. This model is used to study various parameter of a bulk optics diode pumped Nd:YVO_4 FSF laser. There it is shown that the spectral linewidth ($\delta\nu$) of the frequency component of the comb can be expressed as [65]:

$$\delta\nu = \frac{4\sqrt{2}}{3\pi} \cdot \frac{1}{T_0} = \frac{4\sqrt{2}}{3\pi} \cdot \frac{1}{\Delta\nu_a} \cdot \frac{\nu_{FS}}{\tau_{RT}} \tag{4.11}$$

This spectral linewidth therefore is proportional to the frequency chirp rate and inversely proportional to the effective gain bandwidth. For our integrated Er:$LiNbO_3$ laser: $\Delta\nu_a$= 296 GHz (the filter linewidth is 2.4 nm), τ_{RT}= 1.4 ns, and ν_{FS}= 341.4 MHz. So the spectral linewidth of the frequency component of the comb is of the order of 0.5 MHz.

The instantaneous central frequency of the FSF laser is defined by ν_m where the instantaneous spectrum has the peak spectral intensity. In this model, it is seen that the instantaneous frequency of the FSF laser depends on the saturated gain coefficient, the gain medium length, the output coupler reflectance, conversion efficiency of the AO polarization converter, and the active medium loss, but does not depend on the round trip frequency shift and the round trip time.

The spectral bandwidth of the FSF laser emission, or the width of the instantaneous spectral envelope $\Delta\nu_s$ at half-peak intensity level is also defined in this model. This bandwidth depends on the effective number of round trips by the optical field within the net gain available for the oscillation. It is shown that the spectral bandwidth has a minimum value at the particular normalized net gain available. This bandwidth is defined as the product of the saturation-broadened bandwidth and the number of all resonant modes contributing to the frequency shifted feedback operation [65]. The

spectral bandwidth depends on the conversion efficiency of the AO mode converter (η_{ac}), the reflectance of the output coupler (R), the round trip frequency shift (ν_{FS}), the length of the gain medium, the pump power, and the loss coefficient of the gain medium, but does not depend on the round trip time or the cavity length.

After this brief discussion on a model, the experimental investigations of the integrated tunable FSF laser are presented in the following sections.

4.4 Properties of the FSF Laser Output

The experimental setup for the FSF laser operation to study its emission characteristics is shown in figure 4.4. The FSF laser is pumped using a fiber-coupled Bragg-grating stabilized laser diode of 1480 nm wavelength providing an output power up to 135 mW behind a fiber isolator. The polarization of the pump radiation is adjusted either to TM or TE polarization using a fiber optical polarization controller. The fiber to

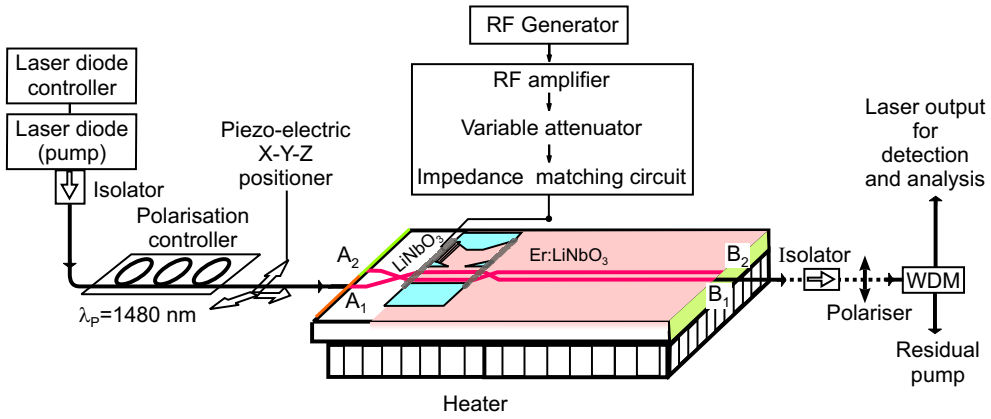

Figure 4.4: Schematic diagram of the experimental setup for the FSF laser operation to study the properties of its output. Components are labelled in the figure.

waveguide coupling is controlled by a piezoelectric X-Y-Z positioner. The electrical drive power for the RF signal to excite the SAW is optimized by adjusting minimum threshold of the laser. The whole substrate is maintained at 20 °C, with a temperature controller consisting of peltier elements and a 10 K-Ohm thermistor as temperature sensor. The laser output is coupled to a WDM to separate the residual pump from the actual laser output.

4.4.1 Power and Tuning Characteristics

The power characteristics of the FSF laser is measured at 1562 nm wavelength (here the Er:$LiNbO_3$ waveguide amplifier has a gain peak). The corresponding frequency of the SAW to select this wavelength is $\sim$ 170.60 MHz (see figure 2.18); the electrical drive power for complete polarization conversion is about 80 mW. The laser output power is measured by a photodiode while the input pump power is increased from

zero to maximum smoothly. Figure 4.5(a) shows the measured power characteristics at 1562 nm wavelength as laser output power versus incident pump power. The results for both modes of operation are presented, for TM- (TE-) polarized pump leading to TM- (TE-) polarized output. The threshold pump power of the laser is ~ 35 mW for TM polarization and ~ 40 mW for TE polarization. The low slope efficiency of about 2.1×10^{-3} and 1.8×10^{-3}, leads to a maximum output power of 130 μW for TM and of 105 μW for TE, respectively, at the incident pump power 95 mW. Mirrors at the both end faces have a high reflectivity of $\sim$97%, which helps to reduce the laser threshold, but the output coupling is not optimized. With the increase of pump power beyond 100 mW (incident), the laser output increases but also the temporal instability grows slowly. The analysis of the output spectrum with an optical spectrum analyzer shows that for TM polarized pump, the spectral distribution is changed slowly with time due to waveguide heating. In case of TE polarized pump, apart from waveguide heating effects, the photorefractive effect (damage) caused a slow variation of the output power.

Tuning of the laser emission wavelength is achieved by tuning the AO filter by changing the SAW frequency. The tuning behavior is shown in figure 4.5(b). There are two curves in the figure; one is the laser wavelength (left ordinate) versus acoustic frequency and the other is the output power of the laser (right ordinate) at different optical wavelengths versus acoustic frequency. For the first curve, the acoustic frequency is changed manually and the corresponding peak wavelength of the laser emission spectrum is recorded by an optical spectrum analyzer with a resolution bandwidth of 10 pm. The pump input is kept fixed at 90 mW incident pump power in TM po-

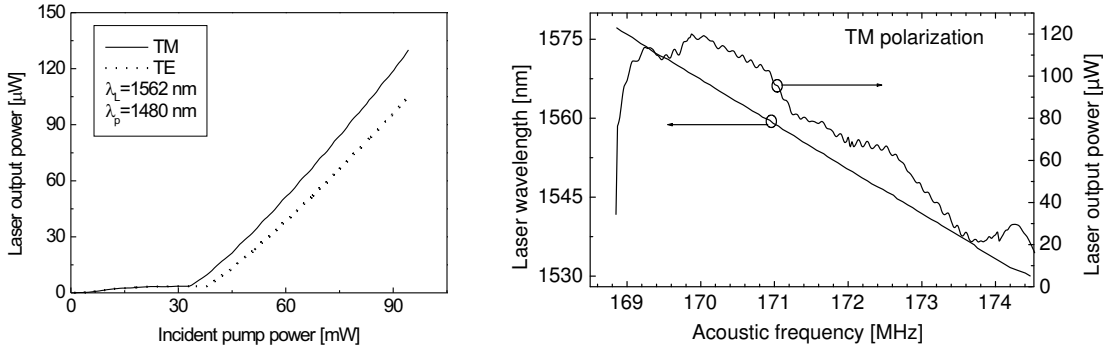

(a) (b)

Figure 4.5: (a) The FSF laser output power versus incident pump power for two modes of operation in TM- and TE- polarization respectively. (b) Laser emission wavelength (left ordinate) and output power (right ordinate) versus SAW frequency at 90 mW of pump power in TM-mode operation.

larization. Continuous tuning of the laser is demonstrated in the wavelength range $1530\,\text{nm} < \lambda < 1577\,\text{nm}$ with a tuning slope of about –8.2 nm/MHz. For the second curve, the SAW frequency is changed quasi continuously (computer controlled) with steps of 1 kHz and the corresponding laser output is recorded by a combination of photodiode and digital multimeter. Due to the wavelength dependence of gain, losses,

acoustooptical conversion efficiency and mode overlap the laser output power strongly varies as function of the emission wavelength (or SAW-frequency). Apart from this strong variation, there is also a modulation on the output power with a very small depth. The source of this modulation is not yet understood.

4.4.2 Spectral Characteristics

Because of its frequency shifted feedback in each round trip, the FSF laser output has a completely different spectral characteristics in comparison with that of a conventional FSC laser output. As discussed in section 4.3, it consists of a comb of chirped frequency components whose frequency chirp rate ν_{FS}/τ_{RT} is of the order of 10^{17} Hz/sec. Together with the change in frequency, the intensity of each component of the comb also changes due to the effective (defined by the filter) amplification in the active Er:$LiNbO_3$. Since the optical spectrum analyzer (OSA) cannot response with such a fast change of frequency, it is expected that it will produce a time averaged spectral envelope of the laser output. Arranging a setup like a Michelson interferometer we can also study the time averaged spectrum of the interference between a reference and a delayed part of the laser output with the OSA. The spectral intensity distribution of the direct laser output and the interferometer output is studied with the OSA and presented here.

A. Spectrum Directly Measured with the Optical Spectrum Analyzer

To study the spectral characteristics, the FSF laser output behind the WDM is fed directly to the optical spectrum analyzer (as shown in figure 4.4). Figure 4.6(a) shows the measured emission spectrum of the FSF laser when it is pumped with TM polarized light and that with TE polarized light is shown in figure 4.6(b). The corresponding laser emissions were also TM and TE polarized, respectively. The chosen resolution bandwidth of the spectrum analyzer of 10 pm would allow to identify a longitudinal mode spectrum (of 5.7 pm wavelength separation of the longitudinal modes) of the 94.2 mm long cavity. The measurements, however, clearly show smooth envelopes like modeless spectra of a linewidth of 180 pm (FWHM) for TM polarized emission and of 165 pm width (FWHM) for TE polarized emission. Er:$LiNbO_3$ is a homogeneous gain medium which should leads single mode emission in the case of conventional FSC laser operation. So these broad spectra confirm the FSF laser operation. The spectral envelopes are slightly asymmetric. As a result of the frequency upshift for TM-polarization the envelope of the spectrum is steepened at the short wavelength side (higher frequencies) (figure 4.6(a)), whereas downshifting of the frequency in the TE-polarized case results in a steepening on the longer wavelength side (figure 4.6(b)). In comparison with TE polarized light, the TM polarized light has lower waveguide losses, bigger mode size, and also for the TM polarized light the polarization splitters have a lower splitting ratio. So the net gain in TM polarization is larger than in TE polarization for this particular laser (pb164x_y). Since the spectral width of the FSF laser output depends on the effective available number of round-trips, i.e., on the net

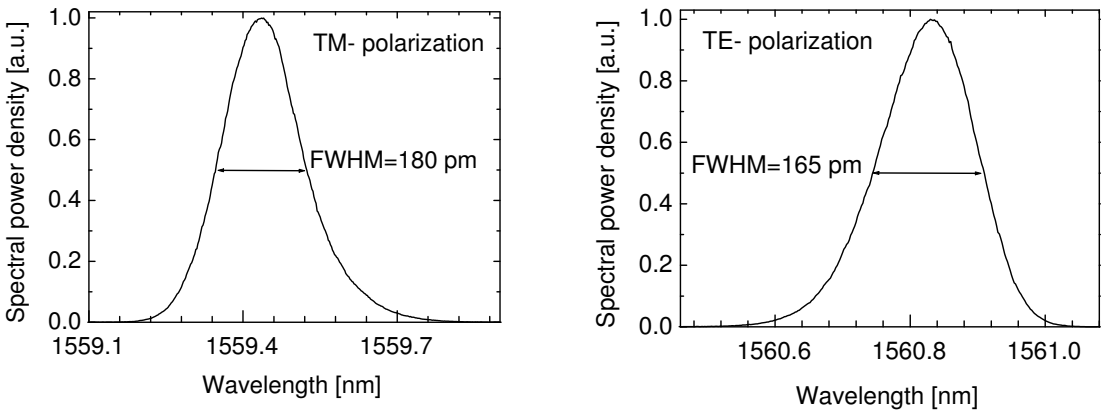

Figure 4.6: Spectra of the FSF laser output measured directly on the optical spectrum analyzer (the spectral resolution bandwidth is 10 pm). (a) pump input and emission output in TM-polarization and frequency upshifted, (b) pump input and emission output in TE-polarization and frequency downshifted.

gain, we can qualitatively understand the wider spectral linewidth of the TM polarized output in comparison with the TE polarized output when the coupled pump power is the same in both cases.

When the pump light has both components of polarization, the laser can also oscillate in both polarizations simultaneously. The spectrum of the laser output in such an operation is shown in figure 4.7. Since the laser fields in TM and TE polarizations

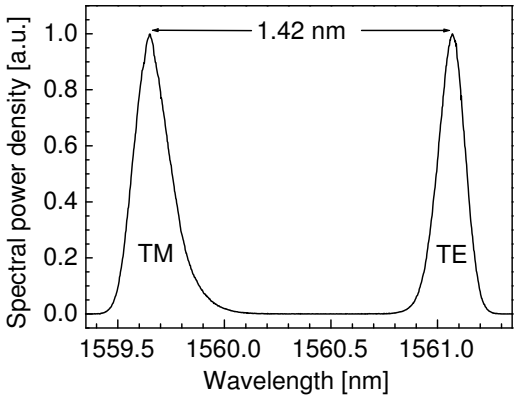

Figure 4.7: Spectrum of the FSF laser emission when the input pump has both TM and TE polarized components simultaneously. The spectrum has two spectral peaks of two polarizations with a wavelength separation of 1.42 nm.

experience the same frequency shift but in opposite directions (upshift and downshift, respectively), the peak emission wavelengths are separated. Also the polarization dependent waveguide losses, available net gain under the AO filter contribute to some extent to this wavelength separation. But these causes are not sufficient to explain the observed separation of 1.42 nm between the peaks in two polarizations. Since the

polarization splitter guides the orthogonally polarized modes in two different branches, the pump light and the laser field of both polarizations will be guided in two different waveguides inside the filter region. The waveguide birefringence decides the phase matched optical wavelength with the applied SAW. The difference of the birefringence of both waveguide sections (which may arise due to inhomogeneities during the fabrication process) causes the wavelength separation for the TE- and TM- pass bands of the filter. In this experiment the polarization of the input pump is adjusted such that the peak spectral power density is the same for the laser output in both polarizations. If the pump polarization is adjusted at 45° the laser output in TM polarization has a higher spectral power density in comparison to that in TE polarization output.

B. Interference Observed with the Optical Spectrum Analyzer

The spectrum of the FSF laser output on the OSA shows the time averaged spectral distribution (nearly Gaussian) of the intensity. The time averaged intensity distribution due to interference of this FSF laser emission is also investigated with the OSA. The schematic diagram of the experimental setup with a Michelson interferometer is shown in figure 4.8(a). The FSF laser output is split into two waves by the beam splitter. The waves are reflected back by the mirrors to recombine by the beam splitter after travelling along unequal path lengths. The output of the interferometer is directly detected with a OSA behind a WDM.

The resulting spectral distribution $I(\lambda)$ due to this two-beam interference (see figure 4.8(b)) shows constructive and destructive interference as a function of wavelength.

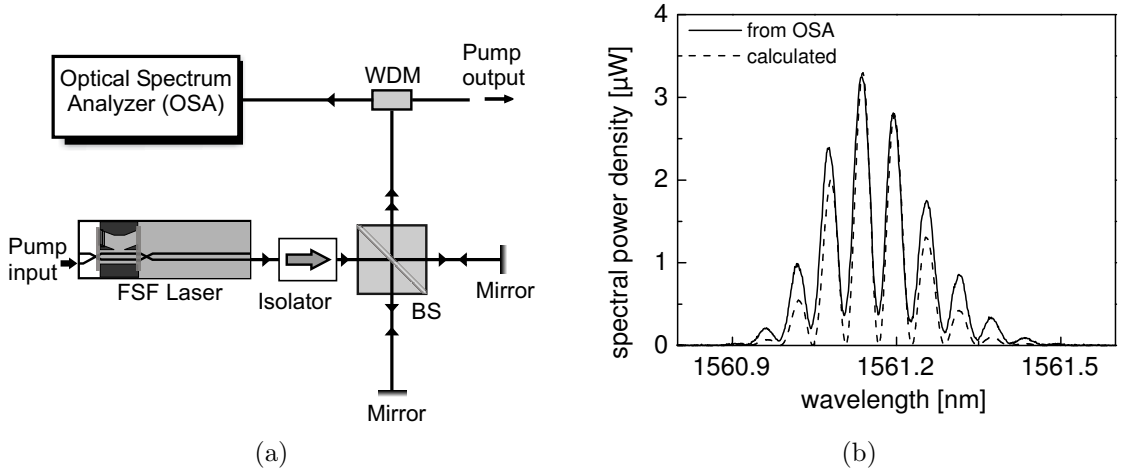

(a) (b)

Figure 4.8: (a) Schematic diagram of the Michelson interferometer setup to study the interference of two beams of the FSF laser output. (b) Spectral distribution of the resultant interference as observed with the optical spectral analyzer (OSA); resolution bandwidth of the OSA is 10 pm.

It can be modelled by a two-beam interference using the spectral intensity distribution $I_0(\lambda)$ of the individual interfering wave and can be expressed as

$$I(\lambda) = 2I_0(\lambda)\left[1 + \cos\left(2\pi\frac{d}{\lambda}\right)\right] \tag{4.12}$$

where d is the optical path difference between the two mirrors. For model calculation, $I_0(\lambda)$ is obtained directly from OSA with spectral resolution bandwidth 10 pm, when the wave from any one branch is allowed to reach OSA. For this set of data the optical path difference between the two mirror is 40.5 mm and it agrees well the calculated result as shown by the dashed line in figure 4.8(b).

In comparison with the model for the FSF laser emission properties described in section 4.3, this time averaged spectral intensity distribution does not represent much details of the spectral content. So further investigations are performed with fast photodiodes and RF spectrum analyzer to measure the time resolved fine spectral structure of the FSF laser output; this will be discussed in the following section.

4.4.3 Spectral Fine Structure

A. Moving Comb of Frequency Components

It is described in the model (see section 4.3) that the spectrum of the FSF laser emission consists of a comb of chirped frequency components with a frequency spacing equal to the laser cavity FSR. If the FSF laser output is directly detected with a fast photodiode, its output can be considered as the result of an interference of the different frequency components of the comb. The instantaneous intensity $I(t)$ detected directly by a photodiode can be given by $|\varepsilon(t)|^2$ (see equation 4.10). This intensity is described as

$$\begin{aligned} I(t) &= \left[\sum_q \left\{\sqrt{R}\,\eta_{ac}G(\nu)\right\}^{(\nu-\nu_0)/\nu_{FS}} \cos\{\phi_q(t)\}\right]^2 \\ &\quad + \left[\sum_q \left\{\sqrt{R}\,\eta_{ac}G(\nu)\right\}^{(\nu-\nu_0)/\nu_{FS}} \sin\{\phi_q(t)\}\right]^2, \quad t > q/\nu_{FS} \end{aligned} \tag{4.13}$$

The corresponding RF spectrum $I_{RF}(\nu)$ of the photodiode output is given as the Fourier spectrum of this intensity and can be expressed as

$$I_{RF}(\nu) = \int_{-\infty}^{+\infty} I(t)\exp(-j2\pi\nu t)dt \tag{4.14}$$

The term $\{\sqrt{R}\,\eta_{ac}G(\nu)\}^{(\nu-\nu_0)/\nu_{FS}}$ is considered to be constant with respect to the temporal variance; then the normalized RF spectrum $\overline{I}_{RF}(\nu)$ can be expressed as

$$\overline{I}_{RF}(\nu) \propto \int_{-\infty}^{+\infty} \left[\left\{\sum_q \cos(\phi_q(t))\right\}^2 + \left\{\sum_q \sin(\phi_q(t))\right\}^2\right] \times \exp(-j2\pi\nu t)dt \tag{4.15}$$

The solutions of equation 4.15 are very complex functions, but analyzing the function $\phi_q(t)$ (see equation 4.6), we know that the solutions must content the terms with $1/(\nu - q/\tau_{RT})$ and $1/(\nu + q/\tau_{RT})$. These terms indicate that the power of the RF spectrum is concentrated at the frequencies q/τ_{RT} where q is an integer. Hence, it

is clear that the RF spectrum of directly detected intensity consists of frequencies which correspond to multiples of the cavity longitudinal mode spacing $1/\tau_{RT}$, also the beating of the frequency combs leads to that result.

To verify this information the following experiment is done. The output of the integrated FSF laser is allowed to pass through a bulk optics isolator and is then coupled to a fast photodiode (frequency bandwidth 50 GHz). The photodiode output is then observed with a RF spectrum analyzer (of a bandwidth of 40 GHz) as shown in figure 4.9. The power of the RF spectrum is concentrated at the frequencies of integer multiples of 711 MHz which is equal to the free spectral range (longitudinal mode spacing) of the laser of length 94.2 mm. The increasing noise level is due to the RF spectrum analyzer itself, not arising from the laser output or from the detector. This observation indicates that the photodiode produced beat signals as a result of the interference between the different components of the frequency comb which are separated by the free spectral range of the cavity of the laser. In this FSF laser the intracavity optical filed experiences a frequency shift of $\nu_{FS} \sim 341\,\text{MHz}$ (twice the frequency of SAW) during each round trip in 1.41 ns. As a result each frequency component of the comb has a very high chirp rate $\gamma \sim 2.42 \times 10^{17}\,\text{Hz/sec}$. The optical spectrum analyzer cannot resolve this highly chirped components, and as a result we see a continuous envelop of the moving frequency comb as shown in figure 4.6.

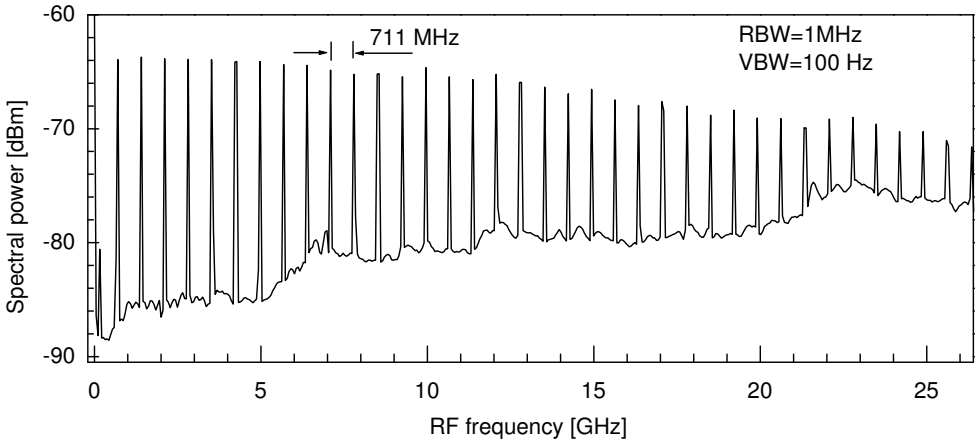

Figure 4.9: RF spectrum of the intensity of the FSF laser emission measured with a fast photodiode. The discrete spectral peaks are the result of the beating of the discrete frequency components with separation of 711 MHz (equal to the laser cavity FSR). RBW: Resolution Bandwidth, VBW: Video Bandwidth of the RF spectrum analyzer.

In the observed RF spectrum (as shown in figure 4.9), the spectral line at frequency zero can be denoted as 0th order beat and that at frequency of 711 MHz as first order beat and so on. These spectral lines of different beat order can be investigated with higher resolution to study the characteristics of this individual beat spectrum. Figure 4.10 shows the beat spectrum of the 1st oder and the 15th order beat. Nearly similar spectral characteristics of different beat order imply that the components of the comb are strongly correlated in phase. The spectral width (at -3 dB of peak power) of

the beat spectrum is measured as 7.5 MHz when the resolution bandwidth is 100 kHz (video bandwidth 50 Hz) of the RF spectrum analyzer. This spectral broadening is due to the limited chirp range of the comb components, here it is (observed on the optical spectrum analyzer, the oscillation bandwidth at FWHM of the peak, $\Delta\nu_s$) ~ 30 GHz. The frequency components in the comb are amplitude-modulated as they are moving under the envelope of the emission spectrum at very high chirp rate. We can easily calculate, that with a chirp rate of 2.42×10^{17} Hz/sec, it takes 124 ns [$= \Delta\nu_s\,(\tau_{RT}/\nu_{FS})$] to cross the FWHM of the emission envelop (of 30 GHz). Thus the broadened beat spectrum can be about 8 MHz, which is nearly equal to the experimentally observed value.

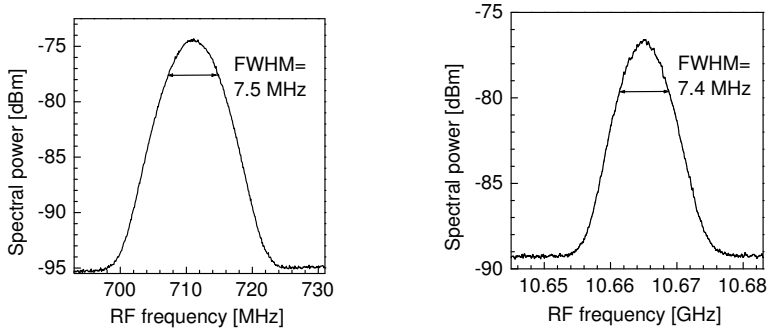

(a) (b)

Figure 4.10: The spectra of the beat signals of different order at the frequencies equal to the integer multiples of the laser cavity FSR (with RBW: 100 kHz and VBW: 50 Hz); (a) spectrum of 1st order beat signal and (b) spectrum of 15th order beat signal.

B. Phase-correlated Chirped Frequency Comb

In the previous experiment it is seen that the FSF laser output consists of a chirped frequency comb evenly spaced at integer multiples of the cavity FSR. The comb components are frequency chirped at a fixed rate and the chirp range of a comb component is limited by the pass band of the AO filter together with the net gain available in the cavity. The comb components are periodically generated at every $1/\nu_{FS}$. The spectral characteristics of the beat signals of different order reveal that there is a phase correlation between the comb components. To understand the phase correlation between the components of the comb experimentally a homodyne detection of the FSF laser output is carried out with a Michelson interferometer setup.

A schematic diagram of the experimental interferometric setup for this detection is shown in the figure 4.11. Here the output of the interferometer is routed via a WDM to a fast photodiode and the corresponding beat signal is analyzed with a RF spectrum analyzer. The mirrors in the two branches of the interferometer are denoted by X and Y to describe the respective reflected waves on the photodiode.

In this interferometer, the two optical fields from two different arms interfere on

the photodiode and the corresponding homodyne signal $I_M(t)$ can be expressed as

$$\begin{aligned} I_M(t) &= \left| \frac{1}{\sqrt{2}} \sum_q E_q(t) \exp[j2\pi\phi_q(t)] + \frac{1}{\sqrt{2}} \sum_{q'} E_{q'}(t-\tau_M) \exp[j2\pi\phi_{q'}(t-\tau_M)] \right|^2 \\ &= \frac{1}{2} \left(\sum_q E_q^2(t) + \sum_{q'} E_{q'}^2(t-\tau_M) \right) \\ &\quad + \sum_q \sum_{r \neq q} E_q(t) E_r(t) \cos[2\pi\{\phi_q(t) - \phi_r(t)\}] \\ &\quad + \sum_{q'} \sum_{s \neq q'} E_q(t-\tau_M) E_s(t-\tau_M) \times \cos[2\pi\{\phi_{q'}(t-\tau_M) - \phi_s(t-\tau_M)\}] \\ &\quad + \sum_{q'} \sum_{q \neq q'} E_q(t) E_{q'}(t-\tau_M) \times \cos[2\pi\{\phi_q(t) - \phi_{q'}(t-\tau_M)\}] \end{aligned} \tag{4.16}$$

where τ_M is a time delay between the optical signals reaching the photodiode due to the optical path difference between the two arms of the interferometer. In this expression, the first term is a dc signal, the second and third term contain frequencies at integral multiples of the cavity FSR. The last summation term gives a signal (say $I_{B(q'-q)}$) related to this path difference in the interferometer.

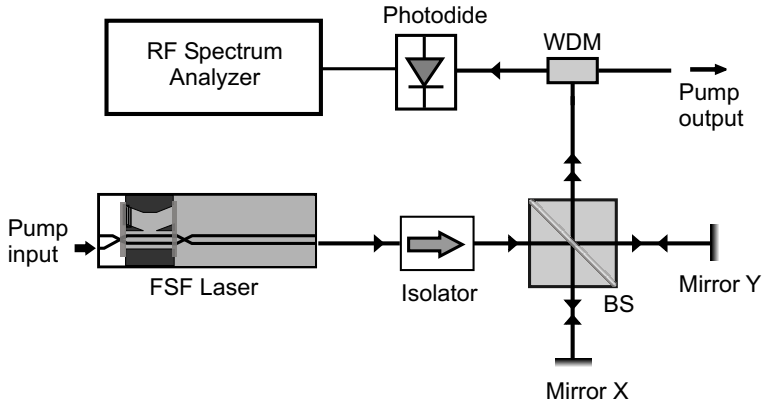

Figure 4.11: A schematic diagram of the Michelson interferometer setup for homodyne detection of the FSF laser output.

The beat signal between the qth and q'th (say $q' = q - m$) comb components I_{Bm} can be expressed by following equations:

$$I_{Bm}(t) = \sum_q E_q(t) E_{q-m}(t-\tau_M) \cos\{2\pi\phi_{Bm}(t)\} \tag{4.17}$$

with (following equation 4.6)

$$\begin{aligned} \phi_{Bm}(t) &= \phi_q(t) - \phi_{q-m}(t-\tau_M) \\ &= \left(\gamma\tau_M - \frac{m}{\tau_{RT}}\right) t - \frac{q}{\nu_{FS}} \left(\gamma\tau_M - \frac{m}{\tau_{RT}}\right) \\ &\quad + \theta + \Phi_q - \Phi_{q-m} \end{aligned} \tag{4.18}$$

where $m = q - q'$ is the "beat order" and θ is a constant phase (independent on both t and q) and expressed as:

$$\theta = m\frac{\tau_M}{\tau_{RT}} - \gamma\frac{\tau_M^2}{2} + \nu_0\tau_M - m\frac{\nu_0}{\nu_{FS}} - \frac{\gamma}{2}\left(\frac{m}{\nu_{FS}}\right)^2 \tag{4.19}$$

Then the beat frequency of the mth order beat is given by

$$\nu_{Bm} = \frac{d}{dt}\phi_{Bm} = \gamma\tau_M - \frac{m}{\tau_{RT}} \tag{4.20}$$

So the beat frequency is proportional to the optical path difference (equivalent to the time delay, τ_M) and is observed at every cavity free spectral range ($1/\tau_{RT}$). Using this expression of ν_{Bm}, the equation 4.18 for the phase relation can be expressed as

$$\phi_{Bm}(t) = \nu_{Bm}t - q\frac{\nu_{Bm}}{\nu_{FS}} + \theta + \Phi_q - \Phi_{q-m} \tag{4.21}$$

The experimental observation of this interferometer output is demonstrated in figure 4.12 when the optical path difference between the mirrors is 29.5 cm. The figure 4.12(a) shows the comb of frequency components as received by the photodiode from the two mirrors X and Y of the two arms of the interferometer. The time delay between X and Y components to reach the photodiode is τ_M. Figure 4.12(b) shows the RF spectrum of the resultant beat signals due to the interference of the comb components. Interference of all X and all Y components produce the beat signals at integer multiples of the laser cavity FSR (=711 MHz) which correspond to the 2nd and 3rd summation of the equation 4.16. The spectral lines at frequencies other than multiples of the cavity FSR are the result of the interference of the delayed components (between X and Y) and correspond to the last summation of the equation 4.16. It is evident that the spectral power levels of these lines are lower than those at the frequencies at integer multiples of the laser cavity FSR. From the knowledge of τ_M, the frequencies of these spectral lines (ν_{Bm}) can be determined from equation 4.20 when the order of the beat signals m are known or vice versa. Interference between X1 and Y1, or X2 and Y2 and so on produce the 0th order beat signal. Interference between Y1 and X2 produce the +1st order beat signal and between Y2 and X1 produce the −1st order beat signal. Similarly, we can follow the other higher order beat formation from the interference of different frequency components of the combs (see figure 4.12(a)). On the other hand, the time delay τ_M can be evaluated if (ν_{Bm}) is measured from the RF spectrum analyzer and its beat order m is known, using the same equation 4.20. Then the optical path difference ($2z$) between the mirrors can be determined via the relation $2z = \tau_M c$, where c is the speed of light, and z is the geometrical path difference along the optical path.

Analyzing the individual spectrum of all the beat signals with higher spectral resolution, it is seen that the spectral characteristics are similar for all possible values of m. There is only a difference of the spectral power density. The spectral characteristics are exactly same as demonstrated in figure 4.10 with a spectral linewidth (FWHM) of

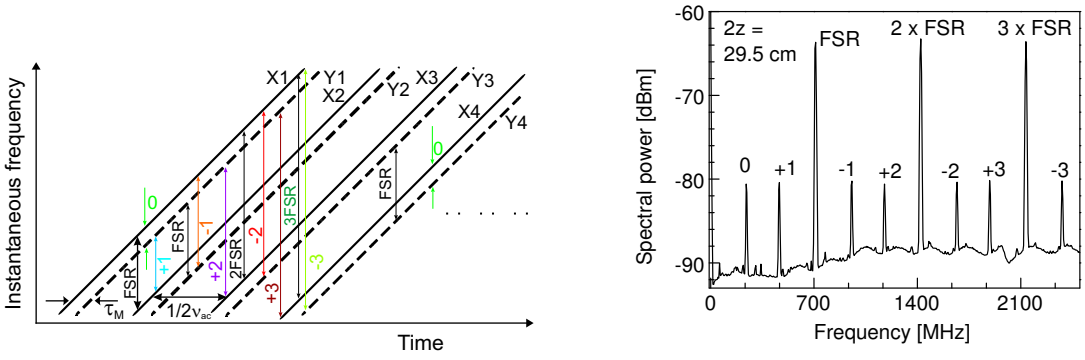

(a) (b)

Figure 4.12: (a) Comb of chirped frequency components as received by the photodiode. X and Y indicate the reflected components from the mirrors X and Y, respectively, and τ_M is the time delay between them. (b) Corresponding RF spectrum of the photodiode output observed with a RBW 500 kHz. Optical path difference between the mirrors: $2z \approx 29.5$ cm. The number with $+/-$ sign indicates the beat order $m(= q - q')$. FSR =711 MHz.

8 MHz. This observation reveals that the chirped frequency components are strongly correlated in phase.

For a better understanding of this phase relation a further experiment is carried out by increasing the path difference between the mirrors of this interferometer. The resultant changes in the RF spectrum of the beat signals (particularly of 0th and 1st order beat) at some points of interest are shown in figure 4.13. The optical path difference between the mirrors is denoted by $2z$ in units of mm in the figure. With the increment of z, the frequency of the 0th order beat is increased and that of the 1st order beat is decreased. At some value of z ($2z > 435$ mm) these two beat signals overlap (as shown in figure 4.13.e) and then again are separated for a further increase of z (figure 4.13.f). In the spectra shown in figure 4.13(b,c,d and e) apart from these 0th and 1st order beat signal there is another sharp spectral line denoted by S (spectral linewidth less than a kHz). Despite the change of z, the frequency of spectrum S remains fixed at 341.4 MHz but the spectral power changes very sharply with z.

The characteristics of this component S will be discussed later in this section. It is to be noted from figure 4.13 that with the change of z, there is a change in frequency of 0th and 1st order beat signals (also of the other higher order beat signal which are not shown here) but the characteristics of the spectra of the individual beat signals remain unchanged.

The changes in frequency of the 0th order beat spectrum with the shifts of the optical path difference $2z$ between the two mirrors are shown in figure 4.14(a). It has a linear relationship with a slope of 815 kHz/mm which is given by γ/c, where γ is the chirp rate and c is the velocity of light (see equation 4.20). In this plot there are no experimental data in the range between 352 MHz and 360 MHz because the 0th order beat spectrum overlaps with the 1st order beat spectrum in this frequency region. The continuous and linear change of the frequency of the beat signal with z indicates that the chirp in the frequency components under the spectral envelop would

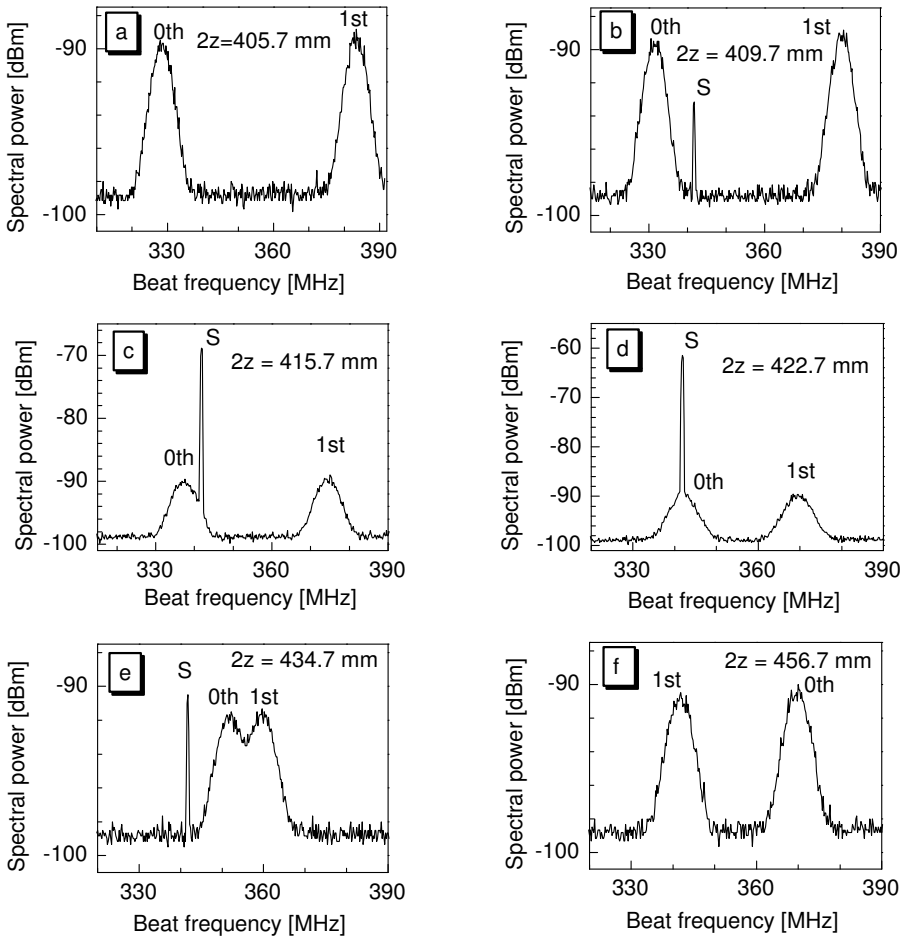

Figure 4.13: The RF spectrum of 0th and 1st order beat signals when the path difference $2z$ [in mm] between the mirrors is increased. The spectra from (a) to (f) show the change in frequency of the beat signals without any change of the individual spectrum characteristics as function of z. Spectra from (b) to (e) show another sharp spectral component S whose frequency is fixed at 341.4 MHz ($=\nu_{FS}$); its spectral power changes rapidly with the change of z.

be a continuous one.

To see more details of the phase relation between the frequency components we can have a close look at the RF spectrum when the 0th order beat is passing through the integer multiple of ν_{FS}. When the m-th order beat frequency ν_{Bm} equals the integer multiples of round trip frequency shift ν_{FS}, the second term of equation 4.21 becomes integer. Thus the $\phi_{Bm}(t)$ no longer depends on q, leaving the dependence of the initial phase difference $\Phi_q - \Phi_{q-m}$ on q. This consideration is useful to analyze the characteristics of the sharp component S.

It is mentioned previously that the spectral component S appears at the fixed frequency 341.4 MHz which is the amount of round trip frequency shift (ν_{FS}) experienced by the laser filed inside the cavity. Figure 4.13.b shows that the component S appears when the 0th order beat is near to 341.4 MHz for $2z$ =409.7 mm. The spectral power of S increases with the increase of z when frequency of the 0th order beat is close to 341.4 MHz (as shown in figure 4.13.c) and reaches a maximum when the frequency of the 0th order beat is exactly 341.4 MHz (as shown in figure 4.13.d). At this point the difference in spectral power levels between component S and the 0th order beat is near by 30 dB. With the further increase of z, the spectral power of S decreases (as shown in figure 4.13.e). But the component S does not appear at all when the 1st order beat signal appears at 341.4 MHz for at path difference of $2z$=456.7 mm (as shown in figure 4.13.f).

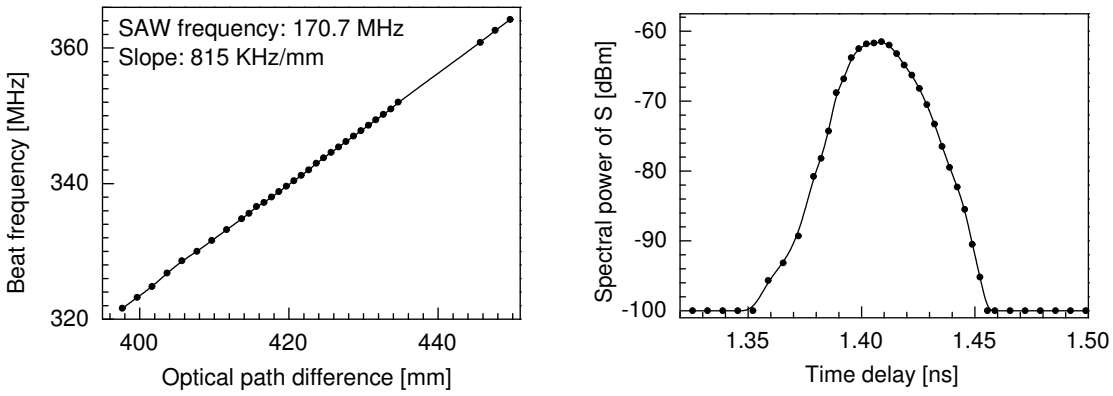

(a) (b)

Figure 4.14: (a) Change of frequency of 0th order beat signal with the change of the optical path difference $2z$ between the mirrors. (b) Variation of spectral power of component S with the time delay τ_M between the comb of frequency components to reach the photodiode.

The variation of the spectral power of the component S is recorded as function of the optical path difference $2z$ between the mirrors. This path difference $2z$ is converted to an equivalent time delay τ_M between the two comb of frequency components to reach the photodiode using the formula $\tau_M = 2z/c$. The figure 4.14(b) shows the variation of the spectral power of the component S with this time delay. It is clear from this analysis that the closer the time delay to the cavity round trip time of the laser (1.41 ns) is, the stronger the intensity of the component S becomes.

When the 0th order beat frequency reaches an integer multiple of ν_{FS}, the phase of the 0th order beat as given by equation 4.21 becomes completely independent of q, then every term in the summation of equation 4.17 interferes constructively and the result is the sharp peak. In other words, when τ_M is set to τ_{RT}, all the beat components are in phase and constructively interfere at the detector. From the analysis of the FSF laser cavity it is seen that the frequency components of the comb are generated continuously with a time interval $1/\nu_{FS}$. So the sharp peak S appears at the integer multiples of ν_{FS}. This component will again appear when the 0th order beat signal will approach the 682.8 MHz ($2\nu_{FS}$), or -in other words- when $\tau_M = 2\tau_{RT}$.

The lack of the sharp peak in the higher order beats (other than 0th order) can be be explained by the dependence of the initial phase difference $\Phi_q - \Phi_{q-m}$ on q. If $\Phi_q - \Phi_{q-m}$ is not constant, i.e., depends on q, the terms in the summation of equation 4.17 interfere destructively. Then the sharp peak is not stimulated and only the broadened beat spectra are observed. The broadened beat spectrum is observed even under the destructive interference condition, since the amplitudes of the comb components are fluctuating. The origin of this amplitude fluctuation is not clear, however, gain saturation of the lasing medium by chirping frequency component might be considered as an origin [62, 67].

4.4.4 FSF Laser Operation with Two SAW Frequencies

In section 2.6 we have seen that simultaneous optical wavelength filtering is possible with a set of corresponding SAW frequencies excited in the AO wavelength filter. The frequencies and power levels of those SAWs can be controlled in a such a way that they will combine to produce a single optical pass-band of wider bandwidth (see figure 2.15(b)). Since the spectral bandwidth of the FSF laser emission ($\Delta\nu_s$) depends mainly on the frequency dependent net gain, an increased spectral width of the FSF laser emission is possible by a simultaneous excitation of SAW frequencies if those are controlled appropriately.

The spectral properties of the integrated FSF laser output are studied experimentally when two SAW frequencies are excited simultaneously. The spectral characteristics of the laser emission (studied directly with the optical spectrum analyzer) are shown in figure 4.15.

The power levels of the two RF signals at frequency 170.70 MHz are optimized individually to get the minimum threshold of the FSF laser emission at the corresponding optical wavelength of 1561.85 nm. One RF source is kept fixed in power and frequency (denoted by f_1) and while the second one is shifted to the frequency 171.41 MHz (denoted by f_2). When only f_2 is excited at frequency 171.41 MHz, the corresponding FSF laser emission is observed at 1556.1 nm (as shown in the figure 4.15). When both f_1 and f_2 are excited simultaneously, only one laser peak is observed at 1561.576 nm (close to the longer wavelength emission for only f_1). It might be due to the lower internal loss at the longer laser wavelength. This shift of 0.27 nm is predicted as sideband shift of the longer wavelength filter when two filters are excited simultaneously [122]. When the frequency of f_2 is varied to bring it near to f_1, the

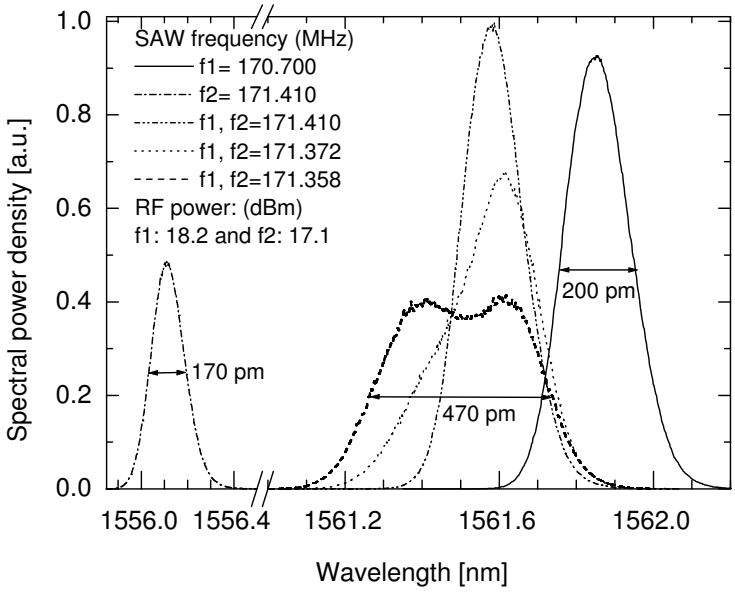

Figure 4.15: Spectra of the FSF laser emission with two SAW frequencies: emission spectra corresponding to only f_1(=170.70 MHz) and only f_2(=171.41 MHz) appear at wavelengths 1561.85 nm and 1556.1 nm, respectively. When they are excited simultaneously the resultant spectrum appears at wavelength 1561.58 nm. Frequency f_1 is kept fixed and f_2 is changed to get other spectra when both SAWs are excited simultaneously. An emission spectral linewidth of 470 pm is observed when f_1=170.7 MHz and f_2=171.358 MHz. The electrical drive power on the transducer for f_1 and f_2 are 18.2 and 17.1 dBm, respectively.

spectral envelope of the FSF laser emission starts to deform as shown in figure 4.15 and the corresponding linewidth increases gradually. When the frequency difference between f_1 and f_2 is set to 0.658 MHz, the linewidth of the spectral envelope of the laser emission reaches a maximum and at this position, the power level of f_2 is adjusted to obtain a symmetrical spectral power distribution around the central wavelength of the laser emission. The measured spectral linewidth of the envelope is 470 pm which is more than doubled in comparison with that of 200 pm when only f_1 is excited. Further closing of the gap between f_1 and f_2 results in a shrinking again and spikes are generated over the envelope. So adjusting the frequencies and power levels of these two RF signal the spectral distribution of the FSF laser output can be adjusted to be used as a broadband laser source. For another set of parameters, a linewidth of 500 pm is also observed [20].

Some details of the spectral properties of the laser emission with two SAWs are not yet understood. The homodyne detection of this FSF laser using the Michelson interferometer does not show any reduction or broadening of the spectral linewidth of the beat signals compared to that with normal emission of the FSF laser with only one SAW. A reduction of the spectral linewidth of the beat signal is expected due to increased chirp range. When the chirp range is doubled, the RF spectra of the beat signals show nearly the same linewidth of about 8 MHz as before. Then it can be thought that the two SAWs produced its independent combs of frequency components

which do not interfere. Then individual combs could produce their own beat signals which are separated in frequency due to different chirp rates of the frequency components. Since the difference in chirp rate is small, we can expect to resolve these frequencies in the same order of beat signal when the beat order m is very high. To observe higher order beat with better resolution, we need a longer optical path difference between the two arms of the interferometer. Since the spectral power density of the laser emission is reduced with the increase of linewidth, it is not possible to carry out this experiment with increased path difference in the present experimental condition.

4.5 Conclusions

Design, operation and output properties of an integrated tunable frequency shifted feedback laser are described in this chapter. An intracavity integrated AO filter is used as tuning element as well as frequency shifter for this laser. Analyzing with an optical spectrum analyzer, it is seen that the laser emission has a relatively broad spectral linewidth with smooth envelope (without any Fabry-Perot mode structure). With a further analysis of an interferometric study, it is revealed that the spectrum of the FSF laser output consists of a comb of chirped frequency components with a regular spacing equal to the cavity free spectral range; they are strongly correlated in phase. A model is presented to describe the laser emission in a time-frequency plane. It explains the nearly Gaussian profile of the spectral envelop. It also shows that the instantaneous frequency ν_m and the spectral linewidth $\Delta\nu_s$ depend on the net gain available in the cavity. But it could not explain the origin of the seed frequency ν_0 from a continuous ASE and how the phase correlation exists between the components. There is also no clear idea to explain the spectral broadening of the beat frequencies. However, the knowledge of the presence of these phase correlated, very fast frequency chirped components in the laser emission lead to apply this laser for frequency domain ranging which will be discussed in next chapter. FSF laser emission also can be used for spectroscopy; however, the linewidth is relatively broad.

Chapter 5

Optical Frequency Domain Ranging with the FSF Laser

5.1 Introduction

Optical frequency domain ranging (OFDR) is an alternative technique to the well known optical time domain ranging (OTDR) [130–133]. This technique is used to measure the distance between a reference plane and a target plane by analyzing the frequency of the beat signal produced by the interference between the optical waves coming from these two planes. The interference signal can be obtained from an arrangement like a Michelson interferometer. In OFDR, a frequency chirped cw laser is used as optical source. Then the frequency of the beat signal is proportional to the time delay caused by the optical path difference between the two waves from the two arms of the interferometer. Among the optical distance measurement techniques, OFDR has attracted attention for its applications to long distance measurements with high resolution and large dynamic range.

The frequency shifted feedback (FSF) laser output has a moving comb of chirped frequency components. The chirp rate is very high and linear and also the comb components have a fixed phase relationship. The FSF laser output can be launched directly to a Michelson interferometer and the optical path difference between the two arms can be evaluated by measuring the frequency of the beat signal. The advantage of using the FSF laser is that it emits frequency chirped optical waves due its frequency shifted feedback (without the aid of any external high frequency electronics control). We can see in the following discussions that there will be always a beat signal of a frequency within the free spectral range (FSR) of the laser cavity. Therefore, the determination of the frequency of the beat signal is easy with a FSF laser source. OFDR using a FSF laser has already been demonstrated for long [76] and short [83] distances with good resolution. This chapter is intended to describe OFDR using the integrated FSF laser presented in the previous chapter.

5.2 The Principles of OFDR

In OFDR, the optical frequency of the conventional laser output is swept linearly over a finite range through some modulation scheme and the light is launched into the input arm of the Michelson interferometer (as shown in figure 5.1). In the Michelson interferometer the frequency chirped light from the reference and target branches interfere on the photodiode.

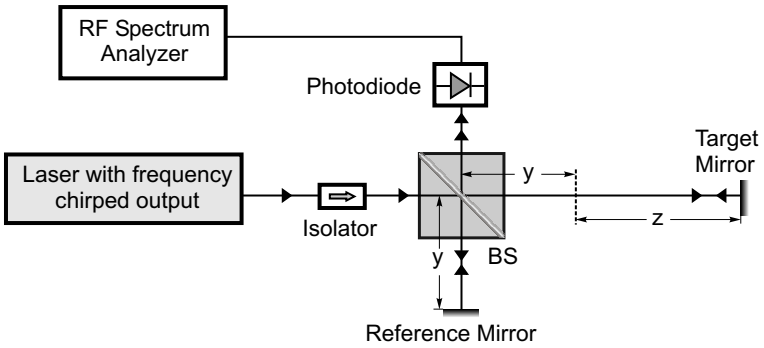

Figure 5.1: Schematic of the setup for measurement of optical path difference ($2z$) between the reference and target mirrors based on optical frequency domain ranging (OFDR) using a Michelson interferometer. BS: Beam Splitter.

Let us first consider the fundamental equations to describe the range and resolution of the OFDR technique. In this reflectometry, the distance z of the target (reflector) is defined with respect to the position of the reference mirror as shown in the figure 5.1. The frequency ν_B of a beat signal corresponding to an optical path difference of $2z$ between the mirrors is given by

$$\nu_B = \frac{d\nu}{dt} \cdot \tau_M = \gamma \frac{2z}{c} \tag{5.1}$$

where $d\nu/dt = \gamma$ is the frequency chirp rate of the laser emission, $\tau_M = 2z/c$ is the time delay between the signals to reach the photodiode from the two branches and c is the velocity of light.

The measurement range and resolution of OFDR are determined by the frequency chirp range (ν_{chirp}) and the chirp rate. The measurement range z_{max} is limited by the frequency chirp range and is given by

$$\begin{aligned} \frac{2z_{max}}{c} &= \frac{\nu_{chirp}}{\gamma} \\ \text{or,} \quad z_{max} &= c\nu_{chirp}/2\gamma \end{aligned} \tag{5.2}$$

and the corresponding maximum beat frequency ν_{Bmax} is given by

$$\nu_{Bmax} = \nu_{chirp} \tag{5.3}$$

If the frequency chirp is ideally linear, ν_{chirp} also determines the spectral width of the beat signal ν_{BW} as [130, 131]

$$\nu_{BW} = \gamma/\nu_{chirp} \tag{5.4}$$

and the spatial resolution is given by

$$\Delta z = c/2\nu_{chirp} \tag{5.5}$$

Equation 5.5 shows that the spatial resolution of the measurement can be improved by increasing the frequency chirp range. In addition, equation 5.2 shows that the measurement range also will increase with an increase of the frequency chirp range. Thus the OFDR can be used for a long-distance high-resolution optical ranging.

Equation 5.2 shows that to increase the measurement range, it is necessary to increase the chirp range ν_{chirp} or to decrease the chirp rate γ. Whereas, equation 5.3 shows that with the increase of the chirp range, the beat frequency ν_{Bmax} also increases and therefore we need a correspondingly wider frequency range of the measurement electronics (say a RF spectrum analyzer). On the other hand, according to equation 5.4, a decrease of the frequency chirp rate requires higher frequency resolution of the spectrum analyzer. Practically, there is a tradeoff between frequency range and resolution of the measurement electronics. It is hard to achieve a high resolution of frequency at a higher range of frequency. Thus, in case of OFDR using a conventional laser source with a frequency chirped output, there is a tradeoff between measurement range and resolution.

This limitation can be overcome by using a FSF laser emission as light source [75]. The difference between the conventional laser and FSF laser outputs is that while the conventional laser output may have longitudinal modes at some fixed frequencies, the FSF laser output has no standing longitudinal mode but has a comb of chirped frequency components with a frequency separation of the longitudinal mode spacing. This spectral characteristics of an integrated FSF laser is described in the previous chapter. Now we will try to describe the principle of a distance measurement using the FSF laser as light source introduced in section 4.4.3 in the previous chapter.

Figure 5.2 shows the spectral output of the FSF laser in the time-frequency plane. The FSF laser output consists of a comb of frequency components which are evenly spaced by the laser cavity FSR ($1/\tau_{RT}$) and the comb components are frequency-chirped with a fixed rate $\gamma = 2\nu_{ac}/\tau_{RT}$ where τ_{RT} is the cavity round trip time and ν_{ac} is the driving frequency of the SAW for acoustooptical polarization conversion. New comb components are periodically generated at every $1/2\nu_{ac}$. The grey scale schematically represents the amplitude envelope of the comb components. The amplitude envelope has approximately a Gaussian profile. The full-width at half-maximum of the envelope is the chirp range and is denoted by ν_{chirp} which is described as $\Delta\nu_s$ in the previous chapter.

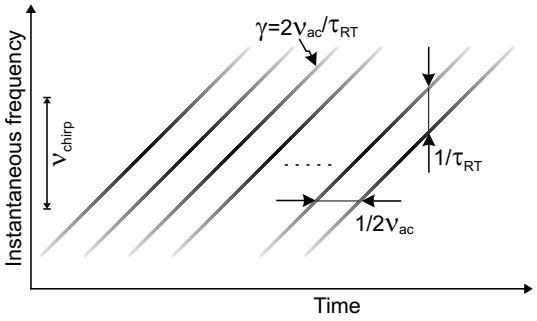

Figure 5.2: Spectral content of the FSF laser emission in the time frequency plane; ν_{chirp}: frequency chirp range; ν_{ac}: SAW frequency; τ_{RT}: round trip time inside the cavity.

5.3 OFDR Using the FSF Laser

5.3.1 Beat Frequency

An arrangement like the Michelson interferometer can also be used for OFDR using a FSF laser as light source. The photodiode receives the optical waves travelling back from the two branches of the interferometer. Each of the waves has its own comb of frequency components which can interfere on the photodiode and produce multiple beat signals. There will be a time delay between the combs to reach the photodiode when there is a path difference ($|z|$) between the two branches along the optical wave propagation. The frequencies of these beat signals are directly related to this time delay and thereby, can be used to evaluate the optical path difference. The homodyne signal on the photodiode is described already by the equations 4.16 to 4.20. Here we can express the time delay τ_M in terms of the optical path difference $2z$ as $2z/c$. Then following the equation 4.20 the beat frequency of the mth-order beat signal is given by

$$\begin{aligned} \nu_{Bm} = \frac{d}{dt}\phi_{Bm} &= \gamma\,\frac{2z}{c} - m\frac{1}{\tau_{RT}}, \qquad \text{with} \quad m = 0, \pm1, \pm2, \pm3, ... \\ &= \frac{4\nu_{ac}}{\tau_{RT}}\,\frac{z}{c} - m\frac{1}{\tau_{RT}} \end{aligned} \tag{5.6}$$

where m is an integer corresponding to the "beat order". Since there are multiple frequency components in each comb in the two branches, the interference will produce multiple beat frequencies for one particular path difference between the branches. These frequencies can be identified with the beat order m. The figure 5.3 shows the beat frequency as function of the distance z.

The zeroth-order beat frequency ($m = 0$) is proportional to the distance, and starts from frequency zero when the path difference is zero. Since the frequency chirp rate γ is very high ($\sim 10^{17}$ Hz/sec) for the FSF laser, the slope of the beat frequency with respect to the distance is large (of the order of 1 MHz/mm). This large slope is very advantageous as it reduces the necessary frequency resolution of the spectrum analyzer. The mth-order beat frequency is m times of the cavity FSR for the distance $z = 0$ and it decreases as the distance increases and then starts to increase when the

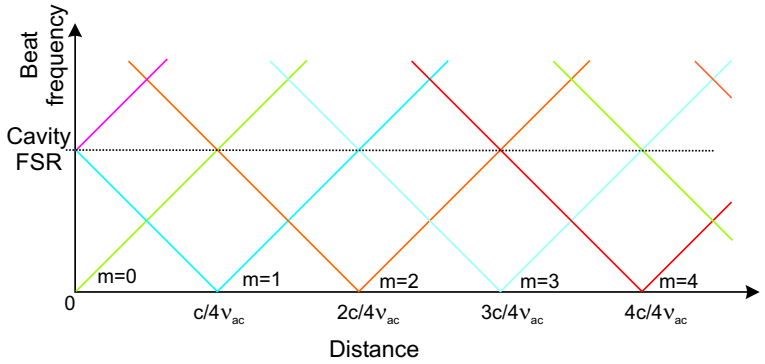

Figure 5.3: The beat frequencies produced by the interference between the components of the combs as a function of the distance. m is the beat order. $mc/4\nu_{ac}$ is the distance where the frequency of the mth beat signal is zero.

distance z exceeds $m(c/4\nu_{ac})$. The range of the distance where the mth-order beat frequency is observed within the cavity FSR can be given by

$$(m-1)c/4\nu_{ac} < \ z \ < (m+1)c/4\nu_{ac} \tag{5.7}$$

So using the FSF laser, it is beneficial for optical ranging since one beat signal is always observed within the cavity FSR for any distance. This reduces the necessary frequency range of the spectrum analyzer down to the laser cavity FSR. However to determine the distance using this technique with a FSF laser, it is essential to know the exact order of the beat signal observed within the FSR of the laser cavity.

5.3.2 The Beat Order Determination

One technique of beat order determination is described by Nakamura et. al. [76] which is described here in brief. Since the relation between the SAW frequency ν_{ac} and the beat frequency ν_{Bm} is known from equation 5.6, it is possible to determine the beat order uniquely using this relation. From equation 5.6 we see that

$$\frac{d\nu_{Bm}}{d\nu_{ac}} = 4\frac{1}{\tau_{RT}}\frac{z}{c} \tag{5.8}$$

Replacing z from equation 5.6, we get

$$\begin{aligned} \frac{d\nu_{Bm}}{d\nu_{ac}} &= \frac{m+\nu_{Bm}\tau_{RT}}{\nu_{ac}\tau_{RT}} \\ \text{or,} \qquad m &= \left(\frac{d\nu_{Bm}}{d\nu_{ac}}\right)\nu_{ac}\tau_{RT} - \nu_{Bm}\tau_{RT} \end{aligned} \tag{5.9}$$

So, when the parameter $1/\tau_{RT}$, the cavity FSR is known, then the beat order m can be determined by measuring the change of the beat frequency as a function of the SAW frequency and using equation 5.9. Thus, once the beat order m is known, the distance can be calculated using equation 5.6. Equation 5.9 indicates that the slope

of the m-th order beat frequency ν_{Bm} as a function of the SAW frequency ν_{ac} is a function the beat order m.

Figure 5.4 shows the beat frequencies as a function of distance for two different values of the SAW frequencies. With the growing beat order, the rate of change of the beat frequency with respect to the SAW frequency increases (see equation 5.9). Again, when the distance is larger, this slope (as given by equation 5.8) becomes steeper and as a result, the relative frequency difference between adjacent orders becomes smaller. It is obvious (as shown in figure 5.3) that the order of the beat observed within the cavity FSR is big indeed, when the distance is long. So there is a limitation on the distance range over which the determination of the beat order m can be done using equation 5.9. There are two factors to address the limitations: the first one is the frequency resolution of the RF spectrum analyzer and the second one is the minimum frequency step of the RF generator to change the SAW frequency.

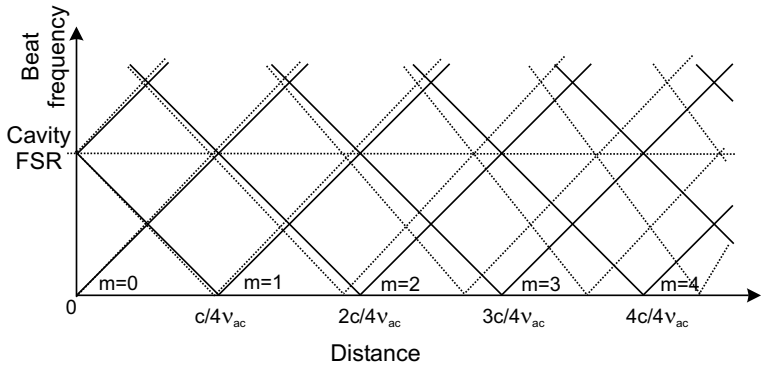

Figure 5.4: The beat frequencies as a function of distance for two different values of SAW frequencies. The dotted line is for a higher value of the SAW frequency. The slope is changed due to the change of the frequency chirp rate γ.

To understand the advantage in numerical examples, let us consider some experimental studies of OFDR using the FSF laser for a long distance measurement. In an experiment, a distance of 150 km is measured with a resolution of 4 mm by analyzing the frequency of the 50,000th-order beat using an erbium-doped fiber FSF laser [134]. In another experiment the 19,832nd beat order is analyzed for a distance measurement of 18.6 km with a resolution of 20 mm using a solid-state Nd:YVO_4 FSF laser [76]. If we wish to use the developed integrated Er:$LiNbO_3$ FSF laser (described in the previous chapter) to measure a distance of 20 km, a beat signal of the 45,713th order would be found within the cavity FSR. The resolution of this measurement would be of 5 mm (a calculated value using equation 5.5). The spectral width of the beat signal is approximately 8 MHz (following equation 5.4). The time interval between the comb components which are forming this beat order is 134 μs. The parameter $d\nu_{Bm}/d\nu_{ac}$ in this beat order can be calculated as $\approx$ 186,480. So a change of the SAW frequency by 100 Hz will produce a shift of 18.648 MHz of the beat frequency.

For OFDR using a cw conventional laser as optical source, a frequency chirp rate of 2.3×10^{14} Hz/sec is required to achieve the same spatial resolution of 5 mm at a distance

of 20 km. The corresponding frequency of the beat signal is 30.6 GHz and the spectral linewidth of the beat signal would be 7.6 kHz. So the advantage is obvious to use a FSF laser emission for a long distance high resolution measurement. For a longer distance, in principle, the limitation may come only in the minimum step available in a RF generator to change the SAW frequency if we restrict to analyze the beat frequency within the laser cavity FSR.

To understand the limitations, an example is considered to point out the corresponding numerical figures associated with the different parameters. When the target distance is 2 km, a beat signal of the order m=4,571 will appear within the cavity FSR if the developed integrated FSF laser is used.

Let us define a parameter $\Delta\nu_{ac}(m,n)$ as the required change of the SAW frequency to shift the mth-order beat by n times the cavity FSR which can be expressed as

$$\Delta\nu_{ac}(m,n)\cdot\frac{d\nu_{Bm}}{d\nu_{ac}}=\frac{n}{\tau_{RT}}$$

Using equation 5.9, we get

$$\begin{aligned}\Delta\nu_{ac}(m,n) &= \frac{n/\tau_{RT}}{d\nu_{Bm}/d\nu_{ac}}\\ &= \frac{n\nu_{ac}}{m+\nu_{Bm}\tau_{RT}}\end{aligned}\tag{5.10}$$

So to shift the mth-order beat frequency ν_{Bm} from frequency 0 to a frequency equal to $1/\tau_{RT}$ (the cavity FSR), the required change in SAW frequency can be given by (following equation 5.10)

$$\begin{aligned}\Delta\nu_{ac}(m,1) &= \frac{1/\tau_{RT}}{d\nu_{Bm}/d\nu_{ac}}\\ &= \frac{\nu_{ac}}{m}\end{aligned}\tag{5.11}$$

since the initial mth-order frequency is assumed to be zero, i.e., $\nu_{Bm}=0$. The change of the beat frequency is

$$\Delta\nu_{Bm}=\frac{1}{\tau_{RT}}\tag{5.12}$$

In our example, using the integrated FSF laser, the required change in SAW frequency is 37.2 kHz. With the same amount of change of the SAW frequency $\Delta\nu_{ac}(m,1)$, the frequency shift of the $(m+1)$th-order beat is given by (assuming the initial frequency of $\nu_{B(m+1)}$ is zero)

$$\begin{aligned}\Delta\nu_{B(m+1)} &= \Delta\nu_{ac}(m,1)\,\frac{d\nu_{B(m+1)}}{d\nu_{ac}}\\ &= \frac{1+1/m}{\tau_{RT}}\end{aligned}\tag{5.13}$$

From equations 5.12 and 5.13, the frequency difference between the two adjacent beat orders, m and the $(m+1)$ is given by

$$\Delta\nu_{B(m+1)} - \Delta\nu_{Bm} = \frac{1/\tau_{RT}}{m} \tag{5.14}$$

The corresponding difference in our example is only 153 kHz. If the spectral linewidth of the beat signals are of the order of 8 MHz, it is difficult to resolve these two adjacent beat orders. So this equation gives an important conclusion that when distance is very long and the corresponding beat order m observed within the cavity FSR is very big: if the frequency resolution of the RF spectrum analyzer is not sufficient to resolve $(1/\tau_{RT})/m$, it is not possible to distinguish the mth-order beat from the $(m+1)$th-order beat within the cavity FSR.

Now we can look at the limitation of the minimum frequency step of the RF generator for the SAW. Using equation 5.11 we can calculate the required change in SAW frequency to shift the frequency of mth and $(m+1)$th order beat signals by the amount of cavity FSR which is given by:

$$\Delta\nu_{ac}(m,1) - \Delta\nu_{ac}(m+1,1) \simeq \frac{\nu_{ac}}{m^2} \tag{5.15}$$

The corresponding value in our example is 8 Hz. Really it is a limiting factor for the RF generators. Thus, if the minimum frequency step of the RF generator is larger than ν_{ac}/m^2, the frequency of the beat signal will cross the cavity FSR with one step change in ν_{ac} and then it is not possible to determine the beat order within the cavity FSR.

Equations 5.14 and 5.15 show that for successful beat order determination within the cavity FSR, the frequency resolution of RF spectrum analyzer ν_{res} and the minimum frequency step of the RF generator ν_{step} should satisfy the following conditions:

$$\nu_{res} < \frac{1/\tau_{RT}}{m} \tag{5.16}$$

$$\nu_{step} < \frac{\nu_{ac}}{m^2} \tag{5.17}$$

If the above conditions are not satisfied by the measuring electronics (for a long distance high resolution measurement) this method of beat order determination is not effective. Still the method is useful if we accept that the beat frequency shift is larger than the cavity FSR. If the beat frequency is shifted by n times the cavity FSR, the required frequency resolution and minimum frequency step are n times those as given by equations 5.16 and 5.17. Then the main advantage is not satisfied for the OFDR using the FSF laser that every measurement can be done within the the frequency bandwidth of the cavity FSR. So for any distance measurement using the FSF laser, we can consider a better way by introducing a technique called as "beat order shift" [76].

As shown in figure 5.5, with the change of the SAW frequency when the frequency of mth-order beat is shifted by the amount of n times the cavity FSR, effectively, the original frequency of the mth-order beat is now replaced by the $(m+n)$th-order beat. The required change of the SAW frequency for this shift is $\Delta\nu_{ac}(m,n)$ and is given by equation 5.10. The parameter n is now the beat order shift. So by considering the

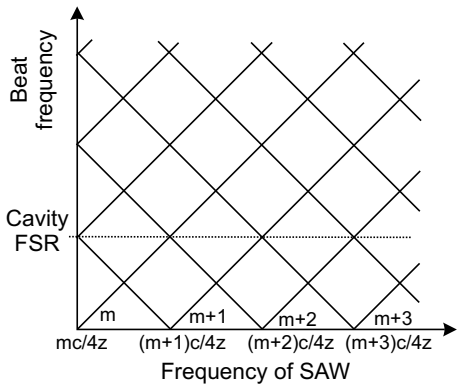

Figure 5.5: The beat frequencies as a function of SAW frequency. With a change of the SAW frequency, if the mth order beat is shifted by n times the cavity FSR, the original frequency of the mth order beat is now occupied by the $(m+n)$th order beat.

beat order shift, the frequency range of the RF spectrum analyzer can be expanded and the order of the beat can be determined within the cavity FSR of the FSF laser even when the distance is very long. So from equations 5.16 and 5.17, we can write the required conditions of frequency resolution of the RF spectrum analyzer and the minimum frequency step of the RF generator are

$$\nu_{res} \quad < \quad \frac{n/\tau_{RT}}{m} \tag{5.18}$$

$$\nu_{step} \quad < \quad \frac{n\nu_{ac}}{m^2} \tag{5.19}$$

Practically, for long distance measurement the condition given by equation 5.19 for ν_{step} is dominant. Then the required beat order shift n can be expressed as

$$n \; > \; m^2 \frac{\nu_{step}}{\nu_{ac}} \tag{5.20}$$

In our example, if the RF generator has a minimum step of 100 Hz, then the value of $n > 12$. Since the beat order shift is proportional to m^2, with the increase of m, this problem of beat order determination will increase very fast which sets the limit of a practical use of this technique.

5.3.3 Range and Resolution

From the previous discussion we have seen that if the beat order is determined by measuring the beat frequencies within the free spectral range of the FSF laser cavity,

the OFDR using a FSF laser has an advantage for long distance measurements compared to OFDR using a conventional laser. This reduces the requirement of frequency range and resolution of the RF spectrum analyzers. If we restrict to perform the measurement within the cavity FSR, then the condition for maximum distance range is given by

$$\Delta\nu_{ac}(M,1) = \nu_{step} \tag{5.21}$$

where M is the maximum value of the beat order for which the ν_{step} of the RF generator will produce the shift of beat frequency by $1/\tau_{RT}$. Then from equation 5.10 and 5.21 we get

$$\nu_{step} = \frac{\nu_{ac}}{M}$$

or,

$$M = \frac{\nu_{ac}}{\nu_{step}} \tag{5.22}$$

Here the distance is assumed such that $M >> \nu_{Bm}\tau_{RT}$. Then using equations 5.7 and 5.22, the distance measurement range z_{max} can be given by

$$z_{max} = \frac{Mc}{4\nu_{ac}} = \frac{c}{4\nu_{step}} \tag{5.23}$$

Then the maximum beat frequency to be measured for this distance is:

$$\nu_{Bmax} = \frac{1}{\tau_{RT}} \tag{5.24}$$

The minimum frequency step, ν_{step} of the commercially available RF generators in the range of SAW frequency of 170 MHz is 100 Hz. With these parameters, we get, $M = 17 \times 10^5$ and the corresponding z_{max} is calculated as 7.5×10^5 meter!

For such a long distance the light propagation loss through the optical path should be considered and so the distance measurement range of the OFDR using FSF laser is practically limited by the dynamic range of the measurement. The dynamic range depends on the laser output power, the propagation loss through the optical path at the laser emission wavelength, and the sensitivity of the measurement equipment [132].

In this measurement technique, a particular factor is not yet considered, that is the coherence of the chirped frequency comb [67]. The main condition to produce a well defined beat signal is that there should be a constant phase relation between the interfering waves. A beat signal of the order of 20,000 is measured without any significant degradation of the spectral width [76]! This experimental observation indicates that there is a phase correlation between the comb components separated by the 20,000 order. But the mechanism of such a highly phase correlated chirped frequency comb generation in the FSF laser is not yet understood.

Like OFDR using a conventional laser, the measured spatial resolution of the OFDR using a FSF laser is determined by the spectral width of the beat signal. The resolution and the spectral width of the beat signal are given by the equations 5.5 and 5.4, respectively, for a conventional laser source and can be re-written for the FSF laser as

$$\Delta z = c/2\nu_{chirp} \tag{5.25}$$

and

$$\nu_{BW} = \gamma/\nu_{chirp} \tag{5.26}$$

The performance of OFDR using a FSF laser is described by the equations from 5.23 to 5.26. So, the advantage is now obvious. Using a frequency modulated conventional laser source, the maximum frequency and the spectral width of the beat signal are related to each other through the frequency chirp range ν_{chirp} as given by equations 5.3 and 5.4. Thus there is a tradeoff between the distance measurement range and the resolution. On the other hand, by using a FSF laser as light source, the tradeoff is removed as given by equation 5.24 and 5.26. Therefore, one can improve the resolution of the distance measurement without considering the range of distance measurement.

5.4 Experimental Results

A laboratory experiment is performed to study OFDR using the integrated FSF laser. The schematic diagram of the measurement setup used in our laboratory is shown in figure 5.6. A Michelson interferometer with free space light propagation and reflections by two plane mirrors terminating the two branches is used. The optical path difference between these two mirrors along the propagation of light is measured using the OFDR technique. The path difference is small (within one meter); therefore the full advantage of the technique, allowing a much large measurement range is not completely exploited here.

The output power of the integrated FSF laser at 1560 nm wavelength is about 130 μW when the incident pump power is 95 mW at 1480 nm wavelength (TM polarized) from a Bragg grating stabilized laser diode. The length of the laser cavity is 94.2 mm. The corresponding cavity FSR ($1/\tau_{RT}$) therefore is 711 MHz. The SAW frequency ν_{ac} corresponding to 1560 nm emission wavelength is 170.70 MHz. The frequency chirp rate γ is calculated as

$$\gamma = \frac{2\nu_{ac}}{\tau_{RT}} = 2.43 \times 10^{17}\,\mathrm{Hz/s}$$

During this experiment, the linewidth of the envelope of the emission spectrum of the laser is 240 pm (measured as FWHM with the optical spectrum analyzer of 10 pm spectral resolution). The equivalent frequency chirp range of the laser output, ν_{chirp}

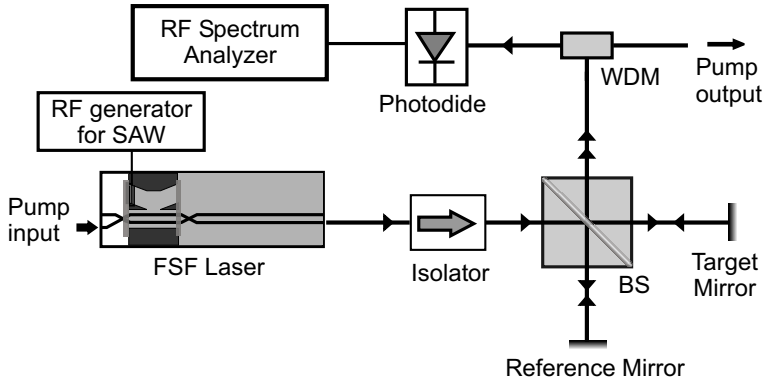

Figure 5.6: Schematic diagram of the experimental setup to study OFDR using FSF laser emission as optical source. BS: 50/50 Beam Splitter and WDM: Wavelength Division Multiplexer.

therefore is about 30 GHz. Then the spatial resolution of the distance measurement is calculated as (from equation 5.25)

$$\Delta z = \frac{c}{2\nu_{chirp}} = \frac{3 \times 10^{11}}{2 \times 30 \times 10^{9}} = 5 \text{ mm}$$

The corresponding spectral width of the beat signal is calculated using the equation 5.26 as

$$\nu_{BW} = \frac{\gamma}{\nu_{chirp}} = \frac{2.43 \times 10^{17}}{30 \times 10^{9}} = 8.1 \text{ MHz}$$

The experimental setup is arranged to keep a geometrical path difference of 11.5 cm between the mirrors along the optical path. The equivalent optical path difference between the mirrors is 23 cm. The corresponding interference signal on the photodiode is analyzed with a RF spectrum analyzer. The RF spectrum of the photodiode output is shown in figure 5.7(a). The order m of the beat signals are denoted by 0th, +1st, –1st and so on. Apart from the beat signals produced by the interference between delayed frequency components due to the path difference of the mirrors from the beam splitter, the beat signals produced by the frequency components of the individual combs are also visible at integer multiples of the laser cavity FSR. The schematic presentation of the superposition of the chirped frequency components of the two combs from two branches as received on the photodiode is shown in figure 5.7(b).

$R1, R2, R3, ...$ are the comb components from the reference branch of the interferometer and $T1, T2, T3, ...$ are those from the target branch arriving at the photodiode with a time delay of $2z/c$ due to the optical path difference of $2z$ between them. The beat signals with a comparatively higher spectral power density are visible at the laser cavity FSR, e.g. 711 MHz, 1422 MHz and so on as shown in the figure 5.7(a). These beat signals are produced by the interference of the frequency components from both combs (between $R1, R2, R3, ..$ and also between $T1, T2, T3, ..$) on the detector and has no relation with the delayed components (as given by the 2nd and 3rd summations of the equation 4.16). When the frequency components from the reference arm interfere

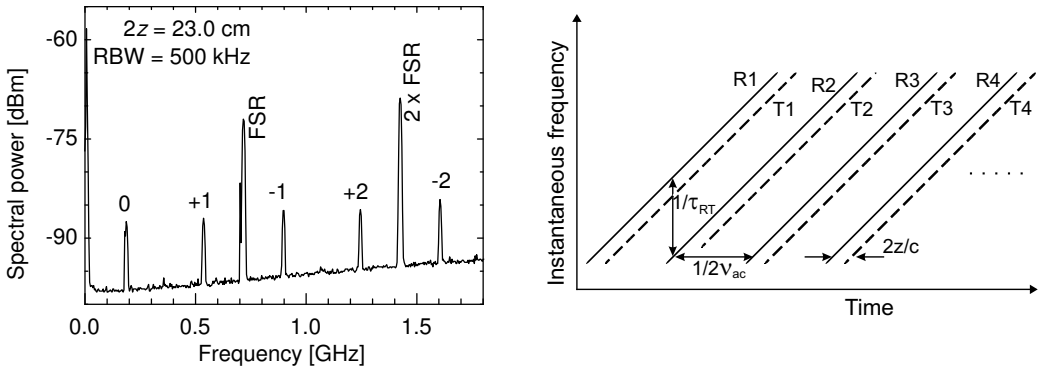

(a) (b)

Figure 5.7: (a) RF-spectrum of the photodiode output when the optical path difference between the mirrors is $2z$=23.0 cm. The frequency range is limited by the bandwidth of the RF spectrum analyzer. Beat order m is indicated by the integers with $+,-$ signs. (b) Two combs of frequency components R and T as received by the photodiode from Reference and Target mirrors, respectively, with a time delay $\tau_M = 2z/c$.

with the same from the target arm with a time delay $2z/c$, multiple beat frequencies are generated as shown in the figure and are denoted by the beat order number, $m = q - q'$. The frequency of the beat signals are given by equation 5.6. When $R1$ interferes with $T1$, $m = 0$. When $T1$ interfere with $R2$, $m = +1$. When $T2$ interfere with $R1$, $m = -1$. From the figure 5.7(b) we can easily find out the combination of frequency components from two combs which produce the RF spectrum as shown in figure 5.7(a). The order m of the beat signals in the measured spectrum can be determined experimentally by varying the SAW frequency and using equation 5.9. Finally the distance z can be calculated using equation 5.6.

An experiment is carried out to determine an unknown optical path difference between the two mirrors in the interferometer. For a certain path difference between the mirrors, a beat signal is found at 686.7 MHz. The frequency is noted from the RF spectrum analyzer with a resolution bandwidth of 30 kHz (while the frequency span is kept 5 MHz/per division). Then the SAW frequency is changed by 300 kHz and the corresponding change of the beat frequency is observed as 2.5 MHz. From this observation, the order of the beat signal is determined as m=1 using equation 5.9. In the experiment, the position of the target mirror is changed with a step of 2 mm. The corresponding frequencies of the beat signal is recorded. Since m is already known, the optical path difference between the mirrors corresponding to those beat frequencies are calculated using equation 5.6. The measured path differences are plotted versus the recorded frequencies of the –1st order beat signal (as shown in figure 5.8(a)). The slope of the beat frequency ν_{B1} as a function of optical path difference ($2z$) is 800 kHz/mm and it agrees well with equation 5.6.

It is to be noted that there are no readings of the beat frequencies when the optical path difference between the two mirrors is near to zero (see figure 5.8(a)). In this situation, the frequency of the beat signal which corresponds to the mirror

positions approaches to 711 MHz. But there is always a beat signal of that frequency (laser cavity FSR) with higher spectral power independent of the mirror positions (as explained before). So, these two signals overlap in this frequency region.

The spectral characteristics of the 1st order beat signal is shown in figure 5.8(b). The FWHM spectral width of the beat signal is 8.0 MHz and it agrees well with the theoretical value calculated according to equation 5.26. The spectral characteristics of all the beat signals are very similar or in other words, the spectral width and intensity of the zeroth order beat signal are very similar to those of the 1st order or 5th order or any higher order beat investigated. A small decrease of the intensities is observed at higher frequencies due to the limited bandwidth of the photodiode.

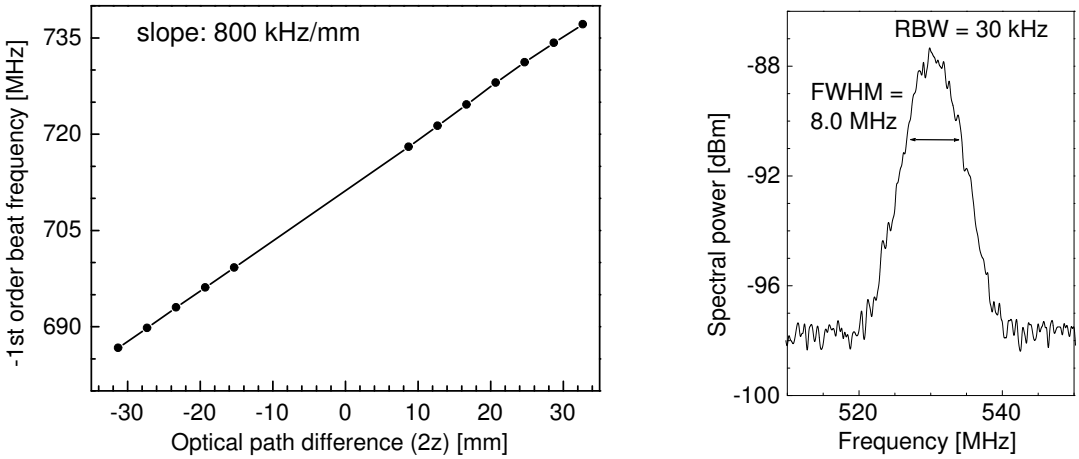

Figure 5.8: (a) Optical path difference versus beat frequency of the –1st order beat signal. (b) Spectral characteristics of the 1st order beat signal appeared in figure 5.7(a).

5.5 Determination of the Length of an Optical Fiber

The length of an optical fiber can be determined by OFDR using a FSF laser. In this experiment, the FSF laser output in the target branch of the Michelson interferometer is coupled into an optical fiber whose length is to be measured, as shown in figure 5.9. Both the end faces of the fiber (denoted by f and r as shown in the figure) act as partially reflecting mirrors and reflect back the optical waves to the photodiode. These two reflected waves interfere and also each of them interferes with the third wave coming from the reference mirror on the photodiode. As a result there will be a beat spectrum produced by the superpositions of the three waves (or three combs of frequency components) or of even more waves if we consider multiple reflections between the fiber ends. The frequencies of the beat signals produced by these interferences are proportional to the positions of the end faces of the optical fiber f and r from which the length of the fiber can be determined if the refractive index of the fiber is known.

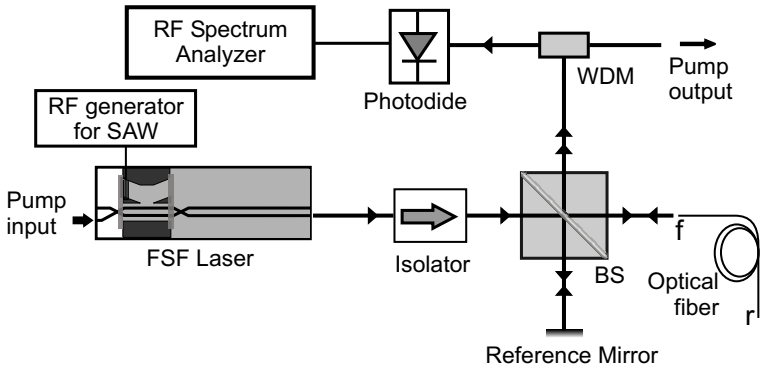

Figure 5.9: Schematic diagram of the experimental setup used to measure the length of an optical fiber. The fiber end faces are denoted by f and r for front and rear ends, respectively.

The RF spectrum of the photodiode signal corresponding to this setup is shown in figure 5.10(a). Apart from the spectral peaks at multiples of the laser cavity FSR there are several spectral peaks in between with different spectral power levels. Let us compare the spectrum shown in figure 5.7(a) with this spectrum. Instead of two spectral peaks in the previous case, now there are four spectral peaks prominent between the cavity FSR. Within the cavity FSR, two spectral peaks appear in different beat order for one reflection point at the target branch (see figure 5.7(a)). So it is clear that these four spectral peaks appear in different beat order and must be due to the reflections from two end faces (f and r) of the optical fiber. The beat orders m of the first four spectral peaks within the cavity FSR are determined by changing the SAW frequency in suitable steps and using equation 5.9. The obtained values of m (in sequence with the increasing frequencies) are 9, 1, 2, and 10. It is evident from the figure 5.3 that within the frequency range from zero to cavity FSR only two consecutive beat orders can appear and they are proportional to the distance of the reflecting source. So the beat orders 1 & 2 correspond to the reflecting plane of the front (f) end face of the fiber and 9 & 10 correspond to that of the rear (r) end of the fiber. The spectral power levels of beat order 1 & 2 is higher than that of 9 & 10. The beat orders m are shown in figure 5.10(a) marked with the letter f or r to indicate the corresponding plane of reflection.

Following equation 5.6, the calculated beat frequencies (ν_{Bm} in GHz) versus the distance of a reflecting plane (z in meter) from a given reference plane for different beat orders m are plotted in figure 5.10(b). This plot is particular for this experiment corresponding to an applied SAW frequency (170.70 MHz) on the FSF laser. The beat orders m are shown by the integers -1, 0, 1, 2, ..., 11. This plot is useful to explain the occurrence of multiple spectral lines of different beat orders for one reflection plane at a particular distance. On this plot a dotted line at the left side (denoted by f) connects the beat frequencies of the spectral lines $1f$ and $2f$ of the spectrum of figure 5.10(a). If this line is extended towards higher frequencies, it touches the line of other beat orders at those spectral frequencies as shown in the 5.10(a). So this line corresponds to the distance for the reflection plane f. Similar observation is true for

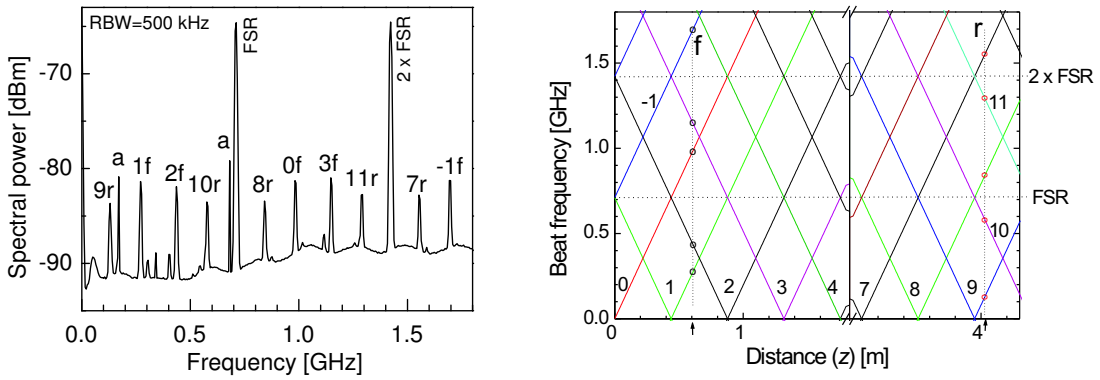

(a) (b)

Figure 5.10: (a) A RF-spectrum of the photodiode output corresponding to the experimental setup using optical fiber (see figure 5.9). Beat signals due to reflections from plane f and r are marked by the letter together with beat order numbers. Beat signal marked by a are harmonics of SAW frequency and has no relevance for measurement. (b) Calculated frequency of the beat signals (of different beat order) versus distance z of the reflecting plane. It is a specific plot corresponding to SAW frequency 170.70 MHz. The planes f and r correspond to the distances of fiber end faces.

another dotted line denoted by r at the right hand side of the plot. It connects all the frequencies of the spectral lines at different beat orders and corresponds to the distance of the plane r.

Since the beat frequencies and their beat orders are known, the distances of the corresponding reflecting planes f and r are calculated (using equation 5.16) as 0.60 m and 4.03 m. These results match with the locations of the planes found on figure 5.10(b). So the distance between these two planes is the measure of the length of the optical fiber if it is divided by refractive index of the fiber. The calculated length of the fiber is 2.29 meter. The actual length of the fiber is 2.27 meter. This difference in the length measurement is within the resolution limit of the OFDR in this experiment. Due to the large spectral line width (8 MHz, as shown in figure 5.8(b)), there is an uncertainty to read the frequency at the peak spectral power.

We can see that for each point of reflection, there are two peaks on the spectrum (beat signals of different order) within the cavity FSR of the laser. It may not be possible to measure the distances of multiple reflection sources, since the beat signal from different points of reflections may accumulate at the same beat frequency but from different beat orders and the determination of an individual beat frequency and its order become ambiguous. So when an optical fiber contains a number of different connectors or components (each one could be a potential source of reflection) along its length then OFDR using FSF laser is not suitable to determine the length.

Apart from the spectral peak denoted by f and r there are some additional spectral peaks with narrow spectral linewidth, which are denoted by a in the spectrum. The frequency of these peaks corresponds to the SAW frequency ($\sim$ 170.70 MHz) and its higher harmonics ($\sim$ 682 MHz). They do not always occur and do not have a constant level of spectral power. Mechanisms of the formation of these spectral components

are not yet known but it is confirmed that those are not due to electronic coupling from the RF generator to the RF spectrum analyzer. They do not exist if the light is blocked at the photodiode.

5.6 Conclusions

The techniques and advantages of frequency domain ranging with the use of a FSF laser as light source is described in this chapter. Simple examples as measurement of distance between two planes and the determination of an optical fibre length are demonstrated experimentally. Main lessons are to understand the beat formation due to the interference between the moving combs of chirped frequency components (which is already described in a previous chapter) and the techniques of its beat order determination. The advantage of the use of a FSF laser is that there is no need of high frequency electronics equipments for source and detection processes for the high resolution long distance measurements. Improvement of the spatial resolution is possible by the increase of the frequency chirp range without any limit in the range of long distance measurement. The high chirp rate of the optical source and its linearity make this technique far superior to the conventional one. These understandings also help to employ this laser for precision measurements in optical fibers like group velocity dispersion [77], chromatic dispersion [78], and polarization mode dispersion [79, 80].

Chapter 6

Summary and Outlook

Two types of acoustooptically tunable integrated lasers are developed and investigated in this work: one is a more conventional frequency shift compensated (FSC) single mode laser and the other is a frequency shifted feedback (FSF) laser demonstrated for the first time as an integrated optical device. The design, operation, and output characteristics of these lasers are presented. As an application of the FSF laser a frequency domain ranging experiment is described to measure distances using an interferometric technique.

Several samples with different laser structures are fabricated by our technology laboratory and investigated to obtain low loss ($<$ 0.1 dB/cm) single mode optical waveguides, good polarization splitters (polarization splitting ratio $<-25\,\mathrm{dB}$), sufficient optical amplification ($>3\,\mathrm{dB}$ in the wavelength range $1530\,\mathrm{nm} < \lambda < 1580\,\mathrm{nm}$) and efficient acoustooptical (AO) polarization conversion ($>97\,\%$) at moderate power level ($<20\,\mathrm{dBm}$) of the driving RF signal. All the experimental data presented in this thesis on characterization of components and laser output are given from only one specific sample.

The key element of these lasers is the acoustooptically tunable filter which is monolithically integrated inside the laser cavity and used as wavelength selective element and as frequency shifter, simultaneously. Using this AO filter, fast and wide tuning is achieved by only changing the frequency of the driving surface acoustic wave (SAW) electronically. A 47 nm ($1530\,\mathrm{nm} < \lambda < 1577\,\mathrm{nm}$) wide tuning range of the laser emission wavelength is observed for the first time for both lasers (FSC and FSF). It is limited by the available gain in the optically pumped Ti:Er:$LiNbO_3$ waveguide. The tuning slope is found to be –8.2 nm/MHz. The tuning speed is limited by the velocity of a SAW on $LiNbO_3$ ($\sim 3700\,\mathrm{m/s}$) to about $5.4\,\mu\mathrm{s}$ and by the SAW frequency addressing system; both are fast enough for practical purposes.

In the FSC mode of operation, single mode laser emission is achieved with a measured linewidth of 12 pm. Since the optical spectrum analyzer has a spectral resolution of 10 pm, it is assumed that the true linewidth is much smaller indicating single mode emission. More than 0.5 mW of laser output power (TE polarized) is obtained in the wavelength range around 1560 nm at a pump power level of 130 mW (TM polarized). An improvement of the output power level is expected if the reflectivity of

the output coupling mirror is optimized. Relaxation oscillations are strongly reduced by an optoelectronic feedback to control the pump power. By changing the relative phase between the two RF signals driving the AO mode converters together with the frequency of the SAWs, a fine tuning is observed. However, due to random jumps between the longitudinal modes in the present experimental environment, the mode hop free tuning of the laser is not evident yet.

As mentioned in section 3.6, future designs are considered to keep the AO mode converters outside the Er-doped waveguide section (gain medium) and to realize an increased length of this medium, simultaneously. Two such possible designs are shown in figure 6.1 where only a TM polarized pump is suitable. The first one has long bent waveguides (figure 6.1(a)). Though bent waveguide of very low losses have already been fabricated on Z-cut wafers in our laboratory [21], further investigations are required to optimize the fabrication parameters for X-cut wafers. There is another option using waveguide reflectors as shown in figure 6.1(b). The waveguide reflector has

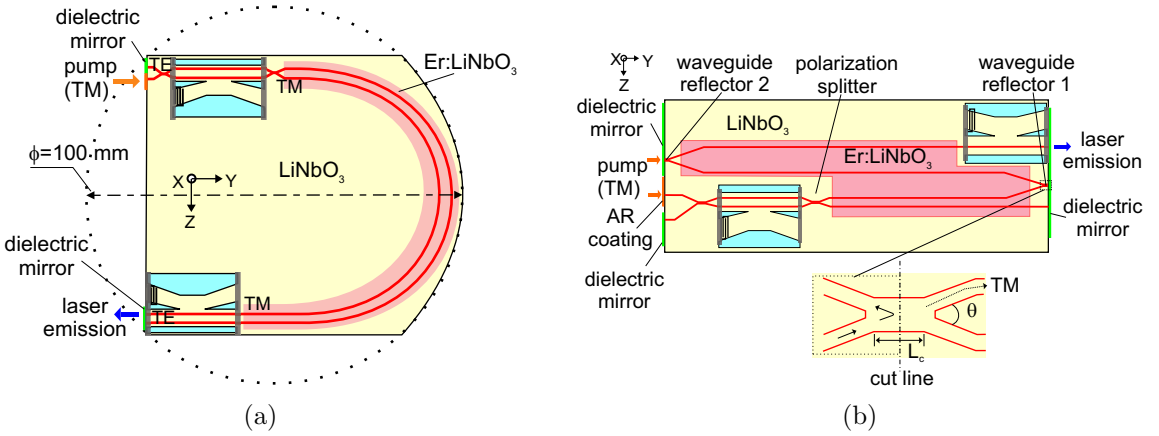

Figure 6.1: Future design to avoid spatial hole burning effects completely and to achieve a high optical amplification by long Er-doped waveguide structures: (a) design with bent waveguides, (b) design with waveguide reflectors

the same configuration as a waveguide polarization splitter as shown in the inset of the figure, but it has to be cut in the middle and needs a reflecting coating on the cut face. The parameters of this waveguide splitter like length of the common waveguide section (L_c) and opening angle between the waveguides (θ) should be carefully adjusted to get the TM-polarized light in the cross state.

The spectral properties of the integrated FSF laser are completely different in comparison with those of the integrated FSC laser. The continuous change in frequency modifies the feedback conditions preventing the build up of discrete longitudinal modes at fixed resonant frequencies. The FSF laser has a very stable emission with a relatively broad spectral linewidth. This linewidth depends mainly on the net round trip gain inside the cavity. At λ=1560 nm a linewidth of more than 180 pm (in TM polarization) is observed. Unique features of this emission are demonstrated when investigated in an interferometric setup. It is demonstrated that in steady state operation, the FSF laser output consists of a comb of chirped (at the rate of 2.43×10^{17} Hz/s) frequency

components with a regular spacing equal to the cavity free spectral range (711 MHz); they are strongly correlated in phase.

The FSF laser investigated here starts from amplified spontaneous emission is investigated. Besides this conventional operation another mode is possible: seeding the laser by coupling a single mode laser emission from outside the cavity. A better signal to noise ratio is expected in such operation. This has been done in a bulk optical configuration with a Titanium-Sapphire (Ti:Sa) gain medium [70]. An analogous experiment will be initiated soon for the integrated laser.

As an application of the FSF laser optical frequency domain ranging (OFDR) is experimentally demonstrated using a Michelson interferometer. The formation of beat signals of different order (due to interference of combs of different frequency components) and their dependence on the object distance are described in detail. Also the use of this technique to measure the length of an optical fiber is presented. The spatial resolution of this measurement is 5 mm. It is limited by the chirp range of the comb components. The distance measuring range is enormously large, only limited by the signal strength. A further improvement in accuracy and resolution can be achieved using a frequency modulated seeding of the FSF laser; the theoretical aspects are reported recently [83]. An experimental investigation will be performed soon using the integrated FSF laser.

Bibliography

[1] S. E. Miller, "Integrated Optics: An Introduction", *Bell System Technical Journal*, **48**, 2059–2069, 1969.

[2] A. Räuber, *"Chemistry and Physics of Lithium Niobate", in Current Topics in Material Science, 1, Edited by E. Kaldis, North-Holland, Amsterdam*, 481–601, 1978.

[3] R. S. Weis and T. K. Gaylord, "Lithium Niobate: Summary of Physical Properties and Crystal Structure", *Applied Physics A*, **37**, 191–203, 1985.

[4] *"Properties of Lithium Niobate"*, Inspec, Institution of Electrical Engineers, 1989.

[5] R. C. Alferness, *"Titanium-Diffused Lithium Niobate Waveguide Devices", in Guided-Wave Optoelectronics*, Springer Series in Electronics and Photonics, 26, Edited by T. Tamir, Springer-Verlag, 145–210, 1988 .

[6] M. Lawrence, "Lithium Niobate Integrated Optics", *Reports on Progress in Physics*, **56**, 363–429, 1993.

[7] L. Arizmendi, "Photonic Applications of Lithium Niobate Crystals", *Physica Status Solidi (A)*, **201**, 253–283, 2004.

[8] E. Lallier, J. P. Pocholle, M. Papuchon, C. Grezes-Besset, M. De Micheli, M. J. Li, Q. He, and D. B. Ostrowski, "Laser Oscillation of Single Mode Channel Waveguide in Nd:MgO:$LiNbO_3$", *Electronics Letters*, **25**, 1491–1492, 1989.

[9] R. Brinkmann, W. Sohler, H. Suche, and Ch. Wersig, "Single Mode Ti-diffused Optical Strip Guides and Lasers in Nd:MgO:$LiNbO_3$", *Technical Digest on Integrated Photonics Research (OSA)*, **5**, 116–117, 1990.

[10] E. Lallier, J. P. Pocholle, M. Papuchon, Q. He, M. De Micheli, D. B. Ostrowski, C. Grezes-Besset, and E. Pelletier, "Integrated Nd:MgO:$LiNbO_3$ FM Mode-locked Waveguide Laser", *Electronics Letters*, **27**, 936–937, 1991.

[11] E. Lallier, D. Papillon, J. P. Pocholle, M. Papuchon, M. De Micheli, and D. B. Ostrowski, "Short Pulse, High Power Q-switched Nd:MgO:$LiNbO_3$ Waveguide Laser", *Electronics Letters*, **29**, 175–176, 1993.

[12] J. Amin, M. Hempsted, J. E. Roman, and J. S. Wilkinson, "Tunable Coupled-cavity Waveguide Laser at Room Temperature in Nd-diffused $LiNbO_3$", *Optics Letters*, **19**, 1541–1543, 1994.

[13] J. P. de Sandro, J. K. Jones, D. P. Shepherd, J. Webjörn, M. Hempstead, J. Wang, and A. C. Tropper, "Tm^{3+}-indiffused $LiNbO_3$ Waveguide Lasers", *Proceedings 7th European Conference on Integrated Optics (ECIO '95), Delft, The Netherlands, post deadline paper*, 17–20, 1995.

[14] J. K. Jones, J. P. de Sandro, M. Hempstead, D. P. Shepherd, A. C. Large, A. C. Tropper, and J. S. Wilkinson, "Channel Waveguide Laser at 1 μm in Yb-indiffused $LiNbO_3$", *Optics Letters*, **20**, 1477–1479, 1995.

[15] W. Sohler, "Erbium Doped Waveguide Amplifiers and Lasers in $LiNbO_3$", *Technical Digest on Integrated Photonics Research (OSA)*, **7**, 212–214, 1995.

[16] W. Sohler and H. Suche, "Erbium-doped Lithium Niobate Waveguide Devices", *Integrated Optical Circuits and Components: Design and Applications; Series of Optical Engineering*, **66**, 127–159, 1999.

[17] I. Baumann, R. Brinkmann, M. Dinand, W. Sohler, L. Beckers, Ch. Buchal, M. Fleuster, H. Holzbrecher, H. Paulus, K.-H. Müller, Th. Gog, G. Materlik, O. Witte, H. Stolz, and W. von der Osten, "Erbium Incorporation in $LiNbO_3$", *Applied Physics A*, **64**, 33–44, 1997.

[18] I. Baumann, S. Bosso, R. Brinkmann, R. Corsini, M. Dinand, A. Greiner, K. Schäfer, J. Söchtig, W. Sohler, and R. Wessel, "Er-Doped Integrated Optical Devices in $LiNbO_3$", *IEEE Journal of Selected Topics in Quantum Electronics*, **2**, 355–366, 1996.

[19] C. Becker, T. Oesselke, J. Pandavenes, R. Ricken, K. Rochhausen, G. Schreiber, W. Sohler, H. Suche, R. Wessel, S. Balsamo, I. Montrosset, and D. Sciancalepore, "Advanced Ti:Er:$LiNbO_3$ Waveguide Lasers", *IEEE Journal of Selected Topics in Quantum Electronics*, **6**, 101–113, 2000.

[20] W. Sohler, B. K. Das, D. Dey, S. Reza, H. Suche, and R. Ricken, "Erbium-doped Lithium Niobate Waveguide Lasers", *IEICE Transactions on Electronics, Joint Special Section on Recent Progress in Optoelectronics and Communicationns, Invited Paper*, **E88-C**, 990–997, 2005.

[21] S. Reza, D. Dey, Y. Min, R. Ricken, and W. Sohler, "Integrated Optical Ring Laser in Er:$LiNbO_3$", *Proceedings of the 12th European Conference on Integrated Optics (ECIO '05), Grenoble, France*, 81–84, 2005.

[22] R. Brinkmann, W. Sohler, and H. Suche, "Continuous-Wave Erbium-diffused $LiNbO_3$ Waveguide Laser", *Electronics Letters*, **27**, 415–416, 1991.

[23] P. Becker, R. Brinkmann, M. Dinand, W. Sohler, and H. Suche, "Er-diffused Ti:$LiNbO_3$ Waveguide Laser of 1563 and 1576 nm Emission Wavelength", *Applied Physics Letters*, **61**, 1257–1259, 1992.

[24] I. Baumann, R. Brinkmann, M. Dinand, W. Sohler, and S. Westenhöfer, "Ti:Er:$LiNbO_3$ Waveguide Lasers of Optimized Efficiency", *IEEE Journal of Quantum Electronics*, **32**, 1695–1706, 1996.

[25] H. Suche, I. Baumann, D. Hiller, and W. Sohler, "Modelocked Er:Ti:$LiNbO_3$-waveguide Laser", *Electronics Letters*, **29**, 1111–1112, 1993.

[26] H. Suche, R. Wessel, S. Westenhöfer, W. Sohler, S. Bosso, C. Carmannini, and R. Corsini, "Harmonically Modelocked Ti:Er:$LiNbO_3$-waveguide Laser", *Optics Letters*, **20**, 596–598, 1995.

[27] H. Suche, T. Oesselke, J. Pandavenes, R. Ricken, K. Rochhausen, W. Sohler, S. Balsamo, I. Montrosset, and K. K. Wong, "Efficient Q-switched Ti:Er:$LiNbO_3$ Waveguide Laser", *Electronics Letters*, **34**, 1228–1229, 1998.

[28] B. K. Das, H. Suche, and W. Sohler, "Single-frequency Ti:Er:$LiNbO_3$ Distributed Bragg Reflector Waveguide Laser with Thermally Fixed Photorefractive Cavity", *Applied Physics B*, **73**, 439–442, 2001.

[29] B. K. Das, R. Ricken, and W. Sohler, "Integrated Optical Distributed Feedback Laser with Ti:Fe:Er:$LiNbO_3$ Waveguide", *Applied Physics Letters*, **82**, 1515–1517, 2003.

[30] B. K. Das, R. Ricken, V. Quiring, H. Suche, and W. Sohler, "Distributed Feedback-Distributed Bragg Reflector Couple Cavity Laser With a Ti:(Fe):Er:$LiNbO_3$ Waveguide", *Optics Letters*, **29**, 165–167, 2004.

[31] J. Söchtig, R. Gross, I. Baumann, W. Sohler, H. Schütz, and R. Widmer, "DBR Waveguide Laser in Erbium-diffusion-doped $LiNbO_3$", *Electronics Letters*, **31**, 551–552, 1995.

[32] Ch. Becker, A. Greiner, Th. Oesselke, A. Pape, W. Sohler, and H. Suche, "Integrated Optical Ti:Er:$LiNbO_3$ distributed bragg reflector laser with a fixed photorefractive grating", *Optics Letters*, **23**, 1194–1196, 1998.

[33] K. Buse, S. Breer, K. Peithmann, S. Kapphan, M. Gao, and E. Krätzig, "Origin of Thermal Fixing in Photorefractive Lithium Niobate Crystals", *Physics Review (B)*, **56**, 1225–1235, 1997.

[34] B. K. Das, *"Integrated Optical Distributed Bragg Reflector and Distributed Feedback Lasers in Er:$LiNbO_3$ Waveguides with Photorefractive Gratings"*, Ph. D. Thesis, Department of Physics, University of Paderborn, Germany, 2003.

[35] J. Frangen, H. Herrmann, R. Ricken, H. Seibert, W. Sohler, and E. Strake, "Integrated Optical, Acoustically Tunable Wavelength Filter", *Electronics Letters*, **25**, 1583–1584, 1989.

[36] F. Tian, Ch. Harizi, H. Herrmann, V. Reimann, R. Ricken, U. Rust, W. Sohler, F. Wehrmann, and S. Westenhöfer, "Polarization-Independent Integrated Optical, Acoustically Tunable Double-Stage Wavelength Filter in $LiNbO_3$", *Journal of Lightwave Technology*, **12**, 1192–1197, 1994.

[37] H. Herrmann, K. Schaefer, and Ch. Smidt, "Low–Loss Tunable Integrated Acoustooptical Wavelength Filter in $LiNbO_3$ with Strong Sidelobe Suppression", *IEEE Photonics Technology Letters*, **10**, 120–122, 1998.

[38] K. W. Cheung, "Acoustooptic Tunable Filters in Narrowband WDM Networks: System Issues and Network Application", *IEEE Journal on Selected Areas in Communications*, **8**, 1015–1025, 1990.

[39] F. Wehrmann, Ch. Harizi, H. Herrmann, U. Rust, W. Sohler, and S. Westenhöfer, "Integrated Optical, Wavelength Selective, Acoustically Tunable 2×2 Switches (Add-Drop Multiplexers) in $LiNbO_3$", *IEEE Journal of Selected Topics in Quantum Electronics*, **2**, 263–269, 1996.

[40] K. Schäfer, I. Baumann, W. Sohler, H. Suche, and S. Westenhöfer, "Diode–Pumped and Packaged Acoustooptically Tunable Ti:Er:$LiNbO_3$ Waveguide Laser of Wide Tunning Range", *IEEE Journal of Quantum Electronics*, **33**, 1636–1641, 1997.

[41] Klaus Schäfer, *"Akustisch abstimmbare Ti:Er:$LiNbO_3$ Wellenlängenfilter mit interner Verstärkung und durchstimmbare Wellenleiterlaser"*, Ph. D. Thesis, Department of Physics, University of Paderborn, Germany, 2003.

[42] S. Reza, H. Herrmann, V. Quiring, R. Ricken, K. Schäfer, H. Suche, and W. Sohler, "Acoustooptically Tunable Integrated Ti:Er:$LiNbO_3$ Laser", *Conference on Lasers and Electro-Optics/Europe (CLEO/Europe-EQEC '03), Munich ICM, Germany*, CL1-5-THU, 2003.

[43] A Yariv, "Coupled-Mode Theory for Guided-Wave Optics ", *IEEE Journal of Quantum Electronics*, **QE-9**, 919–933, 1973.

[44] R. V. Schmidt, "Acoustooptic Interactions Between Guided Optical Waves and Acoustic Surface Waves", *IEEE Transactions on Sonics and Ultrasonics*, **SU-23**, 22–33, 1976.

[45] G. D. Boyd and F. Heismann, "Tunable Acoustooptic Reflection Filter in $LiNbO_3$ Without a Doppler Shift", *Journal of Lightwave Technology*, **7**, 625–631, 1989.

[46] P. D. Hale and F. V. Kowalski, "Output Characterization of a Frequency Shifted Feedback Laser: Theory and Experiment", *IEEE Journal of Quantum Electronics*, **26**, 1845–1851, 1990.

[47] F. V. Kowalski, S. J. Shattil, and P. D. Halle, "Optical Pulse Generation with a Frequency Shifted Feedback Laser", *Applied Physics Letters*, **53**, 734–736, 1988.

[48] F. V. Kowalski, P. D. Halle, and S. J. Shattil, "Broadband Continuous-Wave Laser", *Optics Letters*, **13**, 622–624, 1988.

[49] I. C. M. Littler, S. Balle, and K. Bergmann, "Continuous-Wave Laser Without Frequency-Domain-Mode Structure: Investigation of Emission Properties and Buildup Dynamics", *Journal of the Optical Society of America B*, **8**, 1412–1420, 1991.

[50] I. C. M. Littler and J. H. Eschner, "The CW Modeless Laser: Model Calculation of an Active Feedback Cavity", *Optics Communications*, **87**, 44–52, 1992.

[51] I. C. M. Littler, K. Bergmann, and R. Roy, "Regenerative Amplification of a Weak CW Optical Signal in an Active Frequency Shifted Feedback Cavity", *Optics Communications*, **87**, 53–60, 1992.

[52] I. C. M. Littler, S Balle, and K. Bergmann, "The CW Modeless Laser: Spectral Control, Performance Data and Build-up Dynamics", *Optics Communications*, **88**, 514–522, 1992.

[53] I. C. M. Littler and K. Bergmann, "Generation of Multi-Frequency Laser Emission Using an Active Frequency Shifted Feedback Cavity", *Optics Communications*, **88**, 523–530, 1992.

[54] S. Balle, I. C. M. Littler, K. Bergmann, and F. V. Kowalski, "Frequency Shifted Feedback Dye Laser Operating at a Small Shift Frequency", *Optics Communications*, **102**, 166–174, 1993.

[55] I. R. perry, R. L. Wang, and J. R. M. Barr, "Frequency Shifted Feedback and Frequency Comb Generation in an Er^{3+}-doped Fibre Laser", *Optics Communications*, **109**, 187–194, 1994.

[56] J. Martin, Y. Zhao, S. Balle, K. Bergmann, and M. P. Fewell, "Visible-Wavelength Diode Laser with Weak Frequency-Shifted Optical Feedback", *Optics Communications*, **112**, 109–121, 1994.

[57] F. V. Kowalski, S. Balle, I. C. M. Littler, and K. Bergmann, "Lasers with Internal Frequency-Shifted Feedback", *Optical Engineering*, **33**, 1146–1151, 1994.

[58] S. Balle and K. Bergmann, "Self-pulsing and Instabilities in a Unidirectional Ring Dye Laser with Intracavity Frequency Shift", *Optical Communications*, **116**, 136–142, 1995.

[59] A. P. Willis, A. I. Ferguson, and D. M. Kane, "External Cavity Laser Diodes with Frequency-Shifted Feedback", *Optics Communications*, **116**, 87–93, 1995.

[60] K. Nakamura, K. Kasahara, M. Sato, and H. Ito, "Interferometric Studies on a Diode Pumped Nd:YVO_4 Laser with Frequency-Shifted Feedback", *Optics Communications*, **121**, 137–140, 1995.

[61] G. Bonnet, S. Balle, Th. Kraft, and K. Bergmann, "Dynamics and Self-Modelocking of Titanium-Sapphire Laser with Intracavity Frequency Shifted Feedback", *Optics Communications*, **123**, 790–800, 1996.

[62] K. Nakamura, F. Abe, K. Kasahara, T. Hara, M. Sato, and H. Ito, "Spectral Characteristics of an All Solid-State Frequency-Shifted Feedback Laser", *IEEE Journal of Quantum Electronics*, **33**, 103–111, 1997.

[63] K. Nakamura, F. V. Kowalski, and H. Ito, "Chirped-Frequency Generation in a Translated-Grating-Type Frequency-Shifted Feedback Laser", *Optics Letters*, **22**, 889–891, 1997.

[64] K. Kasahara, K. Nakamura, M. Sato, and H. Ito, "Spectral Dynamics of an All Solid-State Frequency-Shifted Feedback Laser", *Optical Review*, **4**, 180–184, 1997.

[65] K. Kasahara, K. Nakamura, M. Sato, and H. Ito, "Dynamic Properties of an All Solid-State Frequency-Shifted Feedback Laser", *IEEE Journal of Quantum Electronics*, **34**, 190–203, 1998.

[66] F. V. Kowalski, K. Nakamura, and H. Ito, "Frequency Shifted Feedback Lasers: Continuous or Stepwise Frequency Chirped Output", *Optics Communications*, **147**, 103–106, 1998.

[67] K. Nakamura, T. Miyahara, and H. Ito, "Observation of a Highly Phase-Correlated Chirped Frequency Comb Output from a Frequency-Shifted Feedback Laser", *Applied Physics Letters*, **72**, 2631–2633, 1998.

[68] R. Slavik and S. LaRochelle, "Frequency Shift in a Fiber Laser Resonator", *Optics Letters*, **27**, 28–30, 2002.

[69] Y. Wang, N. Saito, S. Wada, and H. Tashiro, "Narrow-band, Widely Electronically Tuned Frequency-Shifted Feedback Laser", *Optics Letters*, **27**, 515–517, 2002.

[70] M. Stellpflug, G. Bonnet, B. W. Shore, and K. Bergmann, "Dynamics of Frequency Shifted Feedback Lasers: Simulation Studies", *Optics Express*, **11**, 2060–2078, 2003.

[71] L. P. Yatsenko, B. W. Shore, and K. Bergmann, "Theory of Frequency-Shifted Feedback Laser", *Optics Communications*, **236**, 183–202, 2004.

[72] I. C. M. Littler, H. M. Keller, U. Gaubatz, and K. Bergmann, "Velocity Control and Cooling of an Atomic Beam Using a Modeless Laser", *Zeitschrift Für Physik D–Atoms, Molecules and Clusters*, **18**, 307–308, 1991.

[73] J. R. M. Barr, G. Y. Liang, and M. W. Phillips, "Accurate Optical Frequency-interval Measurement by use of nonresonant Frequency Comb Generation", *Optics Letters*, **18**, 1010, 1993.

[74] H. Sabert and E. Brinkmeyer, "Pulse Generation in Fiber Lasers with Frequency Shifted Feedback", *Journal of Lightwave Technology*, **12**, 1360–1368, 1994.

[75] K. Nakamura, T. Miyahara, M. Yoshida, T. Hara, and H. Ito, "A New Technique of Optical Ranging by a Frequency-Shifted Feedback Laser", *IEEE Photonics Technology Letters*, **10**, 1772–1774, 1998.

[76] K. Nakamura, T. Hara, M. Yoshida, T. Miyahara, and H. Ito, "Optical Frequency Domain Ranging by a Frequency-Shifted Feedback Laser", *IEEE Journal of Quantum Electronics*, **36**, 305–316, 2000.

[77] M. Yoshida, K. Nakamura, and H. Ito, "A New Method for Measurement of Group Velocity Dispersion of Optical Fibers by Using a Frequency-Shifted Feedback Laser", *IEEE Photonics Technology Letters*, **13**, 227–229, 2001.

[78] K. Iiyama, T. Maeda, and S Takamiya, "Chromatic Dispersion Measurements of Long Optical Fibers by Means of Optical Ranging System Using a Frequency-Shifted Feedback Laser", *IEEE Journal on Selected Topics in Quantum Electronics*, **7**, 484–489, 2001.

[79] M. Yoshida, T. Miyamoto, N. Zou, K. Nakamura, and H. Ito, "Novel PMD Measurement Method Based on OFDR Using a Frequency-Shifted Feedback Fiber Laser", *Optics Express*, **9**, 207–211, 2001.

[80] N. Zou, M. Yoshida, Y. Namihira, and H. Ito, "PMD Measurement Based on Delayed Self-Heterodyne OFDR and Experimental Comparison with ITU-T Round Robin Measurements", *Electronics Letters*, **38**, 115–116, 2002.

[81] F. V. Kowalski, C. Ndiaye, K. Nakamura, and H. Ito, "Noise Waveforms with Repetitive Phase and Nonrepetitive Amplitude", *Optics Letters*, **27**, 1965–1967, 2002.

[82] F. V. Kowalski, C. Ndiaye, K. Nakamura, and H. Ito, "Noise Waveforms Generated by Frequency Shifted Feedback Lasers: Application to Multiple Access Communications", *Optics Communications*, **231**, 149–164, 2004.

[83] L. P. Yatsenko, B. W. Shore, and K. Bergmann, "Ranging and Interferometry with a Frequency Shifted feedback Laser", *Optics Communications*, **242**, 581–598, 2004.

[84] Editors: A. Mooradian, T. Jaeger, and P. Stokseth, *"Tunable Lasers and Applications"*, Springer-Verlag, Springer Series in Optical Sciences, Volume 3, 1976.

[85] Editors: L. F. Mollenauer and J. C. White, *"Tunable Lasers"*, Springer-Verlag, Topics in Applied Physics, Volume 59, 1987.

[86] Editor: F. J. Duarte, *"Tunable Lasers Handbook"*, Academic Press, 1995.

[87] M. C. Amann and J. Buus, *"Tunable Laser Diodes"*, Artech House, 1998.

[88] S. Reza, H. Herrmann, V. Quiring, R. Ricken, K. Schäfer, H. Suche, and W. Sohler, "Frequency Shifted Feedback Ti:Er:$LiNbO_3$ Waveguide Laser of Wide Tunability", *Proceedings of 11th European Conference on Integrated Optics, (ECIO '03), Prague, Czech Republic*, **1**, ThA2-4, 167–170, 2003.

[89] S. Kakio, M. Kitamura, Y. Nakagawa, N. Zou, T. Hara, H. Ito, T. Iizuka, T. Kobayashi, and M. Watanabe, "Waveguide-Type Acoustooptic Frequency Shifter Driven by Surface Acoustic Wave and Its Application to Frequency-Shifted Feedback Fiber Laser", *IEEE Symposium on Ultrasonics, Honolulu, Hawaii*, **2**, 1808–1811, 2003.

[90] W. Sohler, B. K. Das, S. Reza, H. Suche, and R. Ricken, "Er-doped $LiNbO_3$ waveguide Lasers: Recent Progress", *7th International Conference on Optoelectronics, Fiber Optics,and Photonics, (PHOTONICS '04), Cochin, India*, 2004.

[91] R. Regener and W. Sohler, "Loss in Low-Finesse Ti:$LiNbO_3$ Optical Waveguide Resonators", *Applied Physics B*, **36**, 143–147, 1985.

[92] M. Minakata, S. Saito, M. Shibata, and S. Miyazawa, "Precise Determination of Refractive-Index Change in Ti-diffused $LiNbO_3$ Optical Waveguide", *Journal of Applied Physics*, **49**, 4677–4682, 1978.

[93] L. Bersiner, U. Hempelmann, and E. Strake, "Numerical Analysis of Passive Integrated-optical Polarization Splitters: Comparison of Finite-Element Method and Beam-Propagation Method Results", *Journal of the Optical Society of America B*, **8**, 422-433, 1991.

[94] D. Yap, L. M. Johnson, and G. W. Pratt, "Passive Ti:$LiNbO_3$ Channel waveguide TE-TM Mode Splitter", *Applied Physics Letters*, **44**, 583-585, 1984.

[95] Th. Gog, M. Griebenow, and G. Materlik, "X-ray Standing Wave Determination of the Lattice Location of Er Diffused into $LiNbO_3$", *Physics Letters A*, **181**, 417–420, 1993.

[96] V.T. Gabrielyan, A.A. Kaminskii, and L. Li, "Absorption and Luminescence Spectra and Energy Levels of Nd^{3+} and Er^{3+} Ions in $LiNbO_3$ Crystals", *Physica Status Solidi (A)*, **3**, K37–K42, 1970.

[97] R. Brinkmann, *"Integrierte optische Verstärker in Erbium-dotiertem $LiNbO_3$"*, Ph. D. Thesis, Department of Physics, University of Paderborn, Germany, 1994.

[98] R. Brinkmann, I. Baumann, M. Dinand, W. Sohler, and H. Suche, "Erbium-doped Single- and Double-pass Ti:$LiNbO_3$ Waveguide Amplifiers", *IEEE Journal of Quantum Electronics*, **30**, 2356–2360, 1994.

[99] M. Dinand and W. Sohler, "Theoretical Modelling of Optical Amplification in Er-Doped Ti:$LiNbO_3$ Waveguides", *IEEE Journal of Quantum Electronics*, **30**, 1267–1276, 1994.

[100] Manfred Dinand, *"Modellierung Erbiumdotierter Integriert Optischer Verstärker und Laser in $LiNbO_3$"*, Ph. D. Thesis, Department of Physics, University of Paderborn, Germany, 1995.

[101] M. K. Smit, T. Koonen, H. Herrmann, and W. Sohler, *"Wavelength Selective Devices"*, in N. Grote and H. Venghaus (eds.): Fiber Optic Communication Devices, Springer-Verlag, Berlin, 2001.

[102] H. Herrmann, *"Acoustooptical Devices"*, in K. Iga and Y. Kokubun (eds.): Encyclopedic Handbook of Integrated Optics, CRC Press, 2006.

[103] A. Rubiyanto, R. Ricken, H. Herrmann, and W. Sohler, "Integrated Acoustooptical Heterodyne Interferometer operated with a Ti:Er:$LiNbO_3$-Waveguide Laser", *Proceedings of 9th European Conference on Integrated Optics (ECIO '99), Turino, Italy, April 1999*, 275–278, 1999.

[104] B. L. Heffner, D. A. Smith, J. E. Baran, A. Yi-Yan, and K. W. Cheung, "Integrated-Optic Acoustically Tunable Infra-Red Optical Filter", *Electronics Letters*, **24**, 1562–1563, 1988.

[105] J.F. Weller, J.D. Crowley, and T.G. Giallorenzi, "Surface Acoustic Waveguides on $LiNbO_3$ Formed by Titanium in-diffusion", *Applied Physics Letters*, **31**, 146–148, 1977.

[106] S. E. Harris and R. W. Wallace, "Acoustooptic Tunable Filter", *Journal of the Optical Society of America*, **59**, 744–747, 1969.

[107] L. Kuhn, P.F. Heidrich, and E.G. Lean, "Optical Guided Wave Mode Conversion by an Acoustic Surface Wave", *Applied Physics Letters*, **19**, 428–430, 1971.

[108] K. Yamanouchi, "TE-TM Mode Conversion by Interaction Between Elastic Surface Waves and a Laser Beam on a Metal-Diffused Optical Waveguide", *Applied Physics Letters*, **28**, 75–77, 1976.

[109] Y. Ohmachi and J Noda, "$LiNbO_3$ TE-TM Mode Converter Using Collinear Acoustooptic Interaction", *IEEE Journal of Quantum Electronics*, **QE-13**, 43–46, 1977.

[110] L.N. Binh and J Livingstone, "A Wide-Band Acoustooptic TE-TM Mode Converter Using a Doubly Confined Structure", *IEEE Journal of Quantum Electronics*, **QE-16**, 964–971, 1980.

[111] D. A. Smith and J. J. Johnson, "Low Drive-Power Integrated Acoustooptic Filter on $X-$cut $Y-$Propagating $LiNbO_3$", *IEEE Photonics Technology Letters*, **3**, 923–925, 1991.

[112] L. N. Binh and J. Livingstone, "Optimisation of Collinear Acoustooptic TE_m–TM_n Mode Convertor $LiNbO_3$", *IEE Proceedings*, **127**, 323–329, 1980.

[113] L. N. Binh, "Codirectional TE–TM Mode Conversion Through Codirectional and Contradirectional Acoustooptic Interactions", *Applied Physics Letters*, **40**, 650–652, 1982.

[114] U. Rust, *"Modellierung Integriert Akustoopticher Bauelemente in Lithiumniobat"*, Ph. D. Thesis, Department of Physics, University of Paderborn, Germany, 2000.

[115] D. A. Smith and J. J. Johnson, "Sidelobe Suppression in an Acoustooptic Filter with a Raised-Cosine Interaction Length", *Applied Physics Letters*, **61**, 1025–1027, 1992.

[116] H. Herrmann and St. Schmidt, "Integrated Acoustooptical Mode-Converters with Weighted Coupling Using Surface Acoustic Wave Directional Couplers", *Electronics Letters*, **28**, 979–980, 1992.

[117] H. Herrmann, K. Schäfer, and W. Sohler, "Polarization Independent, Integrated Optical, Acoustically Tunable Wavelength Filters/Switches with Tapered Acoustical Directional Coupler", *IEEE Photonics Technology Letters*, **6**, 1335–1337, 1994.

[118] H. Hermann, U. Rust, and K. Schäfer, "Tapered Acoustical Directional Couplers for Integrated Acoustooptical Mode Converters with Weighted Coupling", *Journal of Lightwave Technology*, **13**, 364–374, 1995.

[119] E.G.H. Lean and C.G. Powell, "Optical Probing of Surface Acoustic Waves", *Proceedings of the IEEE*, **58**, 1939–1947, 1970.

[120] G. Cambon, M. Rouzeyre, and G. Simon, "Optical Probing of Surface Raleigh Waves", *Applied Physics Letters*, **18**, 295–298, 1971.

[121] H. Herrmann, Private communication.

[122] F. Tian and H. Herrmann, "Interchannel Interference in Multiwavelength Operation of Integrated Acoustooptical Filters and Switches", *Journal of Lightwave Technology*, **13**, 1146–1154, 1995.

[123] H. Herrmann, P. Muller-Reich, V. Reimann, R. Ricken, H. Seibert, and W. Sohler, "Integrated Optical, TE- and TM-pass, Acoustically Tunable, Double-Stage Wavelength Filters in $LiNbO_3$", *Electronics Letters*, **28**, 642–643, 1992.

[124] A.E. Siegman, *"Lasers"*, University Science Books, California, 1986.

[125] N. Lyi, K. Kitamura, F. Izumi, J. K. Yamamoto, T. Hayashi, H. Asano, and S. Kimura, "Comparative Study of Defect Structures in Lithium Niobate with Different Compositions", *Journal of Solid State Chemistry*, **101**, 340–352, 1992.

[126] R. M. Macfarlane, Y. Sun, F. Konz, R. L. Cone, "Inhomogeneous and Homogeneous Broadening in Pr^{3+}- and Er^{3+} -doped Lithium Niobate", *Technical Digest of Conference on Laser and Electro-Optics (CLEO 2000), Postconference Edition, Sanfrancisco, CA, USA, 7–12 May, 2000, OSA*, **TOPS Vol. 39**, 492–493, 2000.

[127] M. Dinand and Ch. Schütte, "Theoretical Modelling of Relaxation Oscillation in Er-doped Waveguide Lasers", *Journal of Lightwave Technology*, **13**, 14–23, 1995.

[128] W. Streifer and J. R. Whinnery, "Analysis of a Dye Laser Tuned by Acoustooptic Filter", *Applied Physics Letters*, **17**, 335–337, 1970.

[129] D. J. Taylor, S. E. Harris, and S. T. K. Nieh, "Electronic Tuning of a Dye Laser Using the Acoustooptic Filter", *Applied Physics Letters*, **19**, 269–271, 1971.

[130] W. Eickhoff and R. Ulrich, "Optical Frequency Domain Reflectometry in Single-Mode Fiber", *Applied Physics Letters*, **39**, 693–695, 1981.

[131] U. Glombitza and E. Brinkmeyer, "Coherent Frequency-Domain Reflectometry for Characterization of Single-Mode Integrated Optical Waveguides", *Journal of Light Wave Technology*, **11**, 1377–1384, 1993.

[132] R. Passy, N. Gisin, J. P. von der Weid, and H. H. Gilgen, "Experimental and Theoretical Investigations of Coherent OFDR with Semiconductor Laser Sources", *Journal of Light Wave Technology*, **12**, 1622–1630, 1994.

[133] J. P. von der Weid, R. Passy, G. Mussi, and N. Gisin, "On the Characterization of Optical Fiber Network Components with Optical Frequency Domain Reflectometry", *Journal of Lightwave Technology*, **15**, 1131–1141, 1997.

[134] M. Yoshida, K. Nakamura, T. Miyahara, and H. Ito, "Erbium-Doped Fiber Laser with a Frequency-Shifted Feedback; Oscillation Characteristics and Application to Reflectometry", *Technical Digest of Conference on Lasers and Electro-Optics/Europe (CLEO/Europe '98), Glasgow, UK*, Ch. paper CWE3, 157, 1998.

Acknowledgement

It was a valuable experience to carry out my research work in the group of **Applied Physics, at University of Paderborn, Germany**, headed by **Professor Wolfgang Sohler**. I had the great opportunity to come into close contact with so many pioneering people in the field of **Integrated Optics**. I would like to acknowledge their encouragement sincerely. This work was initiated in the framework of the research project: "Integrated Optics in $LiNbO_3$: New Devices, Circuits, and Applications" funded by Deutsche Forschungsgemeinschaft (DFG). I shall remain grateful for this financial support.

I would like to express my sincere thanks and gratefulness to Professor Sohler. He has offered me the opportunity to carry out research work in such a well equipped laboratory and supervised my work with many helpful suggestions, encouragement and critical comments. Furthermore I hold Prof. Sohler in high esteem and I find him to be a great teacher to learn lessons forever.

I got technological help for the fabrication of laser samples from Mr. Raimund Ricken and Mr. Viktor Quiring. Their hard work and cooperation helped this research work to be a successful one. Dr. Klaus Schäfer has introduced me into the experimental activities. Dr. Harald Herrmann and Dr. Hubertus Suche helped me with useful suggestions and guidance in various phases during this work. I would like to thank all the group members I got to know during this period for maintaining a good working atmosphere.

Personally, I wish to thank my friend and colleague Dr. Bijoy K. Das who introduced me into this group to start research work and at the end of my thesis he assisted me with useful discussions. I also like to express my gratefulness to Dr. Indira Chaudhuri, another physicist, whose presence and personal attachment helped me to remain confident and it will continue throughout my work and life. I shall always remember another pleasant personality, Mrs. Irmgard Zimmermann, from whom I have received all types of personal and official help to stay and to do my work. Finally, I am indebted to my parents, sisters and brothers for their patience and mental support which allowed me to stay and study abroad for a long period.

Selim Reza, May 2006, Paderborn